UNIVERSITÀ DI PARMA

UNIVERSITA' DEGLI STUDI DI PARMA

DOTTORATO DI RICERCA IN FISICA

CICLO XXXVI

Weightlessness droplet dynamics and emulsion ageing onboard the International Space Station

Coordinatore:

Chiar.mo Prof. Stefano Carretta

Tutor:

Chiar.mo Prof. Luigi Cristofolini

Chiar.mo Prof. Libero Liggieri

Dottorando:

Valentina Lorusso

Anni Accademici 2020/2021 – 2022/2023

Abstract

The study of colloidal dispersions represents a field of great interest in current research. Colloidal suspensions, as emulsions and foams, are multi-phase materials where one phase is finely dispersed inside another one on the microscopic scale. The investigation of emulsions, foams, and the single molecular layer level poses a captivating theoretical challenge in understanding the intricate connection between macroscopic features and microscopic parameters, in the realm of physics and chemistry of interfaces, dominated by factors like surface tension, interfacial reversible and irreversible absorption, and the dynamic equilibrium between complex formation and disintegration.

In this thesis, I will present the latest results from an experimental campaign that investigated emulsion droplet dynamics in microgravity conditions on the International Space Station (ISS). This research was conducted mainly using Diffusing Wave Spectroscopy (DWS) and made use of the Soft Matter Dynamics (SMD) facility developed by Airbus for the European Space Agency.

The microgravity environment provides an opportunity to study the intrinsic dynamics of droplets, without the complications due to gravity-related effects. As a result of this investigation, the steady-state dynamics can be identified, which often is diffusion-like, but it also enables the identification of transient dynamic events in the life of these droplets. Such accelerations in droplet dynamics are presumably related to drop-drop coalescence or aggregation with concomitant surfactant release, and subsequent onset of transient forces due to Marangoni effects. These processes obviously impact on emulsion stability. Presumably, also hydrodynamic correlations play an important role in determining the nature of the droplet dynamics. The investigation of these phenomena on ground would be much more difficult and less precise, due to the prevailing dynamics induced by gravity, such as drop creaming and sedimentation and the drop crowding effects arising as a consequence.

The results obtained in microgravity are discussed in the light of preliminary ground laboratory experiments: an extensive campaign was conducted by using the “Elegant Bread Board” (EBB), a laboratory copy of the SMD instrument on the ISS. The results of this campaign were used to define the best conditions for the experiments on orbit, like emulsion formulation and preparation protocol, and to precisely measure some critical parameters describing the light propagation inside the sample cell, whose exact determination is necessary for the interpretation of the DWS results. Further, a comparative analysis of the results on ground and in microgravity is expected to help the elucidation of the mechanisms governing emulsion stability.

Overall, the results of these investigations are expected to provide novel insights into droplet dynamics and the destabilization of emulsions. In the current panorama of industrial processes, which often rely on empirical guidelines, this new knowledge will play a pivotal role in the transition towards a more systematic and by-design approach in emulsion technology, with substantial industrial and societal advantages. All this is in line with the green economy paradigm, achieved through the reduction and optimization of additive usage.

Emulsions and foams, thanks to their widespread utility, can be very relevant for space exploration and colonization enabling technologies. For instance, solid foams can be used as lightweight building materials, and more importantly, if made by stimuli responsive or catalytic materials, they can provide very efficient functional materials, thanks to the very favourable surface to volume ratio. Very interesting in this respect is also the possibility to produce solid foams based on in situ resources, like regoliths, in the paradigm of In Situ Resource Utilization (ISRU). Also, emulsion technology is expected to play a major role as enabling technology for space exploration, for instance in the field of heat exchange (e.g. by exploiting the concept of boiling emulsions) but also for cleaning purposes and for new materials design (e.g. exploiting emulsion polymerization strategies) and in the refinement of waste recycling processes.

Contents

1. Single liquid interfaces

Liquid interfaces refer to the boundary or interface between two immiscible liquids or between a liquid and another phase (such as a gas or solid). They play a fundamental role in various natural and technological processes, influencing the behaviour and properties of the liquids involved. By definition, a liquid interface refers to the region where two distinct liquids come into contact, creating a distinct boundary between them. It is at this interface that the two liquids interact, exhibiting unique properties and behaviours that distinguish them from the bulk phases. It is characterized by interfacial properties such as interfacial tension, interfacial energy, and interfacial thickness [1–4].

- **Surface tension** $\gamma = F/L$, also known as **interfacial tension** (in the case of emulsions, at the boundary of two immiscible liquids), is the force (F) per unit length (L) acting tangentially along the liquid interface. It arises due to the imbalance of intermolecular forces at the interface, causing liquids to minimize their interfacial area and adopt a shape with minimal surface area. As a result, there is a region near the interface where the properties, such as density, composition, and molecular arrangement, gradually transition from one phase to the other. Interfacial tension influences the behaviour and stability of liquid interfaces, including wetting, emulsification, and the formation of droplets or bubbles, interfacial rheology, and interfacial dynamics [5].

- Surface tension can also be expressed through a surface energy $\gamma = E/A$. **Interfacial energy** is the amount of energy required to create a unit area (A) of an interface between two phases. It is a measure of the energy associated with the boundary or interface between two immiscible liquids or between a liquid and another. When two phases come into contact, the molecules at the interface experience different intermolecular interactions compared to those within the bulk phases. This leads to a change in energy, and the interfacial energy quantifies this energy difference per unit area. Also, interfacial energy plays a significant role in determining the behaviour and stability of liquid interfaces [6].

- **Interfacial thickness** refers to the distance or region over which the properties of a liquid interface extend into each adjacent phase. It represents the spatial extent of the interfacial region and is typically characterized by a transition in the properties between the two bulk phases. The interfacial thickness can vary depending on the specific system and the forces involved. It is influenced by factors such as intermolecular forces, temperature, pressure, and the presence of surfactants or additives that can alter the interfacial properties. Interfacial thickness is a measurable dimension on the macroscopic level, while at the microscopic level, it signifies the gradual transition of material properties across an interface. This transition impacts how molecules or particles interact and, consequently, influences the bulk properties and overall behaviour of the system. Then, changes on the microscopic scale can yield significant effects at the macroscopic level.

Understanding and manipulating liquid interfaces have important implications in various technological fields. It is crucial in industries such as pharmaceuticals, cosmetics, food processing, and materials science, where emulsions, coatings, and surface treatments are common.

When discussing interfaces, it is essential to consider the concept of Laplace pressure. It plays a fundamental role in understanding phenomena such as capillary action, bubble formation, stability of emulsions and foams, fluid flow in small channels, and many more. Laplace pressure, also known as capillary pressure or interfacial pressure, refers to the pressure difference across the curved interface between two immiscible fluids.

Laplace pressure refers to the disparity in pressure between the interior and exterior of a curved surface serving as the interface between two fluid regions.

According to Young-Laplace equation:

$$\Delta \mathrm{P} = \mathrm{P}_{\mathrm{inside}} - P_{outside} = \gamma \left(\frac{1}{R_1} - \frac{1}{R_2} \right) \tag{1.1}$$

In the case of bubbles or droplets, where $R_1 = R_2$, the pressure difference (ΔP) across a curved interface is directly proportional to the surface tension (γ) and inversely proportional to the radius of curvature (R) of the interface $\Delta P = 2\gamma/R$. This indicates that as the radius of curvature decreases, the Laplace pressure increases. In other words, the pressure within a liquid droplet or a bubble is higher on the inside than on the outside due to the curvature of the interface.

1.1 Surfactants

Surfactants, short for surface-active agents, are chemical compounds that possess unique properties due to their molecular structure. They are commonly used in various industries and products, including detergents, personal care items, pharmaceuticals, and food processing. Surfactants have a dual nature, with one end of the molecule being hydrophilic (water-loving) and the other end being hydrophobic (water-repelling) or lipophilic (fat-loving). This characteristic allows surfactants to interact with both water and oil or fat, making them effective in reducing surface tension and facilitating the mixing of substances that would otherwise be immiscible [7–13].

The primary function of surfactants is to lower the interfacial tension (γ) between different phases, such as between liquid and air or between oil and water. They achieve this by spontaneous adsorbing at interfaces (adsorption Γ), which helps to stabilize emulsions, disperse substances, enhance wetting and diffusion, and increase the solubility of hydrophobic compounds in water. Surfactants can be classified into different types based on their charge properties, including anionic (negatively charged), cationic (positively charged), non-ionic (no charge), and amphoteric/zwitterionic (both positive and negative charges). Each type has specific applications and characteristics, such as cleaning, foaming, disinfection, or conditioning properties.

The **Gibbs adsorption isotherm** is a fundamental equation that connects alterations in the concentration of a component at a surface to variations in surface tension, consequently influencing surface energy. When dealing with two coexisting phases (α and β), the surface is located at the boundary between these two phases. Gibbs [14] proposed an idealized model with an infinitesimally thin surface layer, wherein the chemical composition of the bulk phases α and β remains constant except at the dividing surface.

Surface excess quantities are defined and attributed to a geometrical “dividing interface” of area A and the Interfacial tension is defined as an energy excess

$$\gamma = \frac{U + P_\alpha V_\alpha + P_\beta V_\beta}{A} \tag{1.2}$$

with U internal total energy, and P and V pressure and volume of the phases α and β.

Indeed, in presence of surfactant, the quantitative measure of adsorption Γ is defined as a surface excess concentration $\Gamma = \frac{n_i^\sigma}{A}$. The molar surface excess represents the difference between the total moles n of the i-th component in a system and the moles of the i-th component in a particular phase (either α or β) and is represented by $n_i^\sigma = n_i - c_{i,\alpha} V_\alpha - c_{i,\beta} V_\beta$.

The relation between surface tension and the surface excess concentration for a closed system at equilibrium is given by the Gibbs-Dunhem equation.

$$\mathrm{d}\gamma = -\mathrm{s}^{\sigma} dT - \sum_i \Gamma_i d\mu_i \tag{1.3}$$

with temperature T, entropy s, surface excess concentration Γ, and chemical potential μ.

A non-linear partition equilibrium exists between the surfactant in the bulk and at the interface. The system is described by the variables γ, c,Γ. In fact, the three relations hold:

- $\gamma = \gamma(c)$ $\boldsymbol{\gamma - c}$ **isotherm**, the surface tension depends on the bulk concentration.
- $\gamma = \gamma(\Gamma)$ **surface equation state**, the relation between γ and Γ is a material property.
- $\Gamma = -\frac{1}{RT}\left(\frac{\partial \gamma}{\partial(\ln(c)}\right)$ **Gibbs adsorption equation**, thermodynamics provide the adsorption, at a constant temperature. It assumes that the bulk phase is an ideal solution. Which is true only for dilute systems (below the CMC).

For rational use of surfactants, it is of particular importance to quantitatively determine the ratio between the polar (hydrophilic) and apolar (lipophilic) portions. This ratio is called HLB (Hydrophylic-Lipophylic-Balance), which is a semi-empirical parameter calculated based on the number and type of hydrophilic and lipophilic groups in the surfactant molecule [15]. To predict the action produced by a surfactant on the dispersion of two immiscible liquids, the Bancroft rule is used: the continuous phase will be the one in which the surfactant is most soluble. For example, since the water solubility of a surfactant increases with the HLB value, it is logical that surfactants with high HLB predominantly give oil-in-water (O/W) emulsions. The solubility of the surfactant is then based on the distinct characteristics of hydrophobic and hydrophilic chains, and consequently on the partition coefficient (k_p), which measures the breakdown between water and oil. A lower value of k_p indicates that less material is required, allowing for better control of the concentration in water. When surfactants are dissolved in the phase, their addition increases adsorption at the oil-water interface. Each surfactant has a characteristic concentration known as Critical Micelle Concentration (CMC) which refers to the minimum concentration of surfactant molecules in a solution at which micelles start to form spontaneously. Micelles are supramolecular aggregates of surfactant molecules that self-assemble to reduce the system's free energy. When the concentration of surfactant in a solution is below the CMC, the individual surfactant molecules exist as monomers dispersed in the solvent. However, as the surfactant concentration exceeds the CMC, the hydrophilic heads of the surfactant molecules align towards the solvent, while the hydrophobic tails come together in the core of the micelle, forming a stable structure. The formation of micelles is driven by the tendency to minimize the system's free energy by reducing the exposure of hydrophobic groups to the solvent. The CMC is a critical point at which the aggregation of surfactant molecules becomes favourable, and micelles begin to form spontaneously. Beyond CMC, the Surface Tension stabilizes at a constant level. This is due to the continuous formation of additional micelles with the introduction of more surfactant. Meanwhile, the concentration of the monomer, the only species capable of adsorbing at the interface, remains equal to the CMC. The CMC is an important parameter in understanding the behaviour and properties of surfactant solutions. It affects various phenomena, such as surface tension, solubilization, emulsion stability, and foaming characteristics. Additionally, the CMC can vary depending on factors such as temperature, pH, and the presence of other substances in the solution.

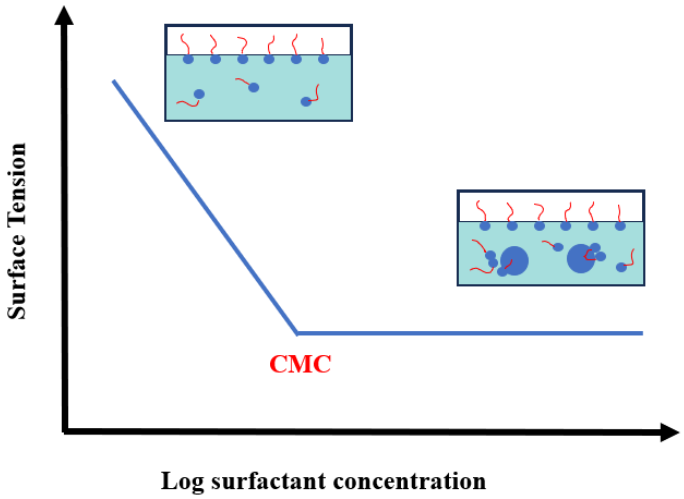

Figure 1.1 Relationship between surface tension and surfactant concentration. When the surfactant concentration is low, the surfactant is dissolved as individual monomers, which can attach to the interface and reduce the surface tension. As the concentration reaches the critical micelle concentration (CMC), the amount of monomers remains constant, and so does the surface tension. Above the CMC, the micelles spontaneously self-assemble.

1.2 DLVO Theory

DLVO (Derjaguin, Landau, Verwey, Overbeek) theory provides a valuable understanding of colloidal interactions and is widely used in various fields to explain and predict the behaviour of colloidal systems. This theoretical framework is used to describe the stability and interactions between colloidal particles in a liquid medium. It provides insights into the forces that govern colloidal systems and their aggregation behaviour. The DLVO theory considers two primary forces that act on colloidal particles: Van der Waals forces and Electrostatic forces [6].

Van der Waals forces are attractive forces resulting from fluctuations in electron distribution within particles. These potentials ϕ_{VdW} are influenced by the distance between particles and become stronger as the particles get closer. For this reason, they contribute to the attraction between colloidal particles. Instead, electrostatic forces arise from the interaction between charged particles. Colloidal particles can acquire a net charge due to their surface properties or the presence of ions in the surrounding medium. **Electrostatic forces** can be either repulsive (like-charged particles) or attractive (oppositely charged particles). The electrostatic component of the DLVO interaction is calculated under the condition of low surface potentials. This condition arises when the potential energy of a single elementary charge on the surface is significantly smaller than the thermal energy scale k_BT. The usual electrostatic potential for a point-charge in vacuum $\psi(R) \propto 1/R$ in a polarizable medium becomes decaying exponential for reasonable values of surface potential $\psi(x) = \psi_0 \exp(-\kappa x)$, where x is the distance from surface and $\kappa^{-1} \propto |z|^{-1}$ (with |z| valence of electrolyte) is called Debye screening length, and it is a measure of the thickness of the ionic layer effectively screening the Coulomb interaction in the long-range. Approaching the surface, a more realistic picture assumes an inner layer (Stern layer) and an outer portion. The inner layer is modelled as a monolayer of counterions, whose density is given by the Langmuir adsorption isotherm $\Gamma = \frac{\Gamma_\infty C}{a+C}$, where Γ_∞ is the total number of (moles of) "sites"/area for adsorption on the adsorbent surface (saturation of adsorption) and C is the bulk concentration.

The Derjaugin approximation provides valuable insight into the interaction between curved surfaces. It establishes a proportional relationship between the total force of interaction for a pair of spherical surfaces and the repulsive energy of interaction for a pair of flat surfaces. Therefore, the electrostatic potential energy of repulsion between two spheres, both with a radius of a and separated by r, is denoted as

$$\phi_{\mathrm{R}} \propto \frac{ak_BT}{\kappa^2} \exp(-\kappa r) \tag{1.4}$$

DLVO theory combines the effects of Van der Waals and electrostatic forces to predict the stability and behaviour of colloidal systems ("DLVO" curves). It considers the total potential energy between particles as the sum of these potentials $\phi_{net} = \phi_{VdW} + \phi_R$. At very close distances, the combination of these forces results in a deep attractive well, which is referred to as the primary minimum. At larger distances, the energy profile goes through a maximum, or energy barrier, and subsequently passes through a shallow minimum, which is referred to as the secondary minimum. In a colloidal system, the state of thermodynamic equilibrium is often attained when the particles reside in the deep primary minimum. In this region, attractive forces dominate over repulsive forces at shorter molecular distances. As a result, the particles undergo aggregation, and this process is irreversible. However, if the energy barrier's height is too substantial to surmount, the colloidal particles may remain in the secondary minimum. In this scenario, weak attractions form between the particles, and their aggregation becomes reversible.

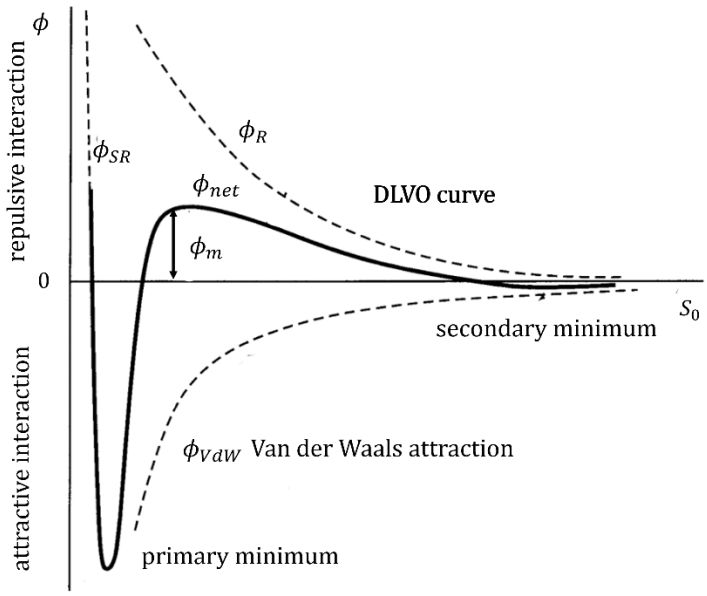

Figure 1.2 The sum of the van der Waals attraction ϕ_{VdW} and electrostatic repulsion ϕ_R results in "DLVO curve". It displays a primary minimum followed by an intermediate maximum in potential ϕ_m, that represents the potential energy barrier and a secondary minimum.

Thus, the stability of colloidal dispersions is determined by the balance between attractive Van der Waals forces and repulsive electrostatic forces. If the repulsive forces dominate, colloidal particles remain dispersed, leading to a stable suspension. However, if the attractive forces become stronger, particles may come close enough to form aggregates or flocculates, resulting in the destabilization of the system.

When applying the DLVO theory to emulsions, certain considerations come into play. For instance, in emulsions, the coalescence process involves the disruption of the adsorbed film around the droplets. When calculating the potential energy barrier that hinders the collision of oil droplets, one must consider such factors

as distortion or flattening of oil droplets upon close approach. If the velocity of the approach is sufficiently small, a flat film of constant thickness is formed. At higher velocities, the film surfaces deform, resulting in a "dimple" shape, with the centre thicker than the boundary. The equilibrium thickness of this film arises from the balance between capillary pressure at the film borders and the force between the film surfaces per unit area, known as the "disjoining pressure" [16].

The DLVO theory, originally developed for understanding colloidal stability, has been expanded to incorporate the influence of shear flow in fluid dynamic systems [17]. This theory accounts for a lag-time in the aggregation of particles induced by shear. The lag-time decreases exponentially as the shear rate increases. Furthermore, the theory elucidates the subsequent regime of aggregation kinetics that occurs after the lag-time, as well as the characteristic bimodal distribution of cluster sizes typically observed in systems undergoing shear-induced aggregation and self-assembly [17].

1.3 Neutron reflectometry on NP complexes adsorbed at interfaces

In the first part of my PhD, the interfacial properties due to the adsorption of surfactants on nanoparticles were studied. This study is motivated by several factors:

Firstly, the utilization of surfactant adsorption onto the surface of nanoparticles (NP) presents a cost-effective method to regulate the hydrophilic-lipophilic balance of NPs within dispersions. Secondly, when cetyltrimethylammonium bromide (CTAB) is introduced to hydrophilic silica nanoparticles (SiO_2 NP), it could lead to the formation of distinct complexes at the interface of the dispersion. This process would effectively stabilize Pickering emulsions (see chapter 2.2). Furthermore, investigations involving tensiometric and interfacial rheology have demonstrated that the properties of these layers change as the quantity of CTAB added to the dispersion increases. In other words, the degree of hydrophobicity of the complexes influences the characteristics of these layers. Nevertheless, there is still a degree of speculation regarding the precise structure of these mixed particle-surfactant layers at the liquid-liquid interface.

Adsorption of surfactants on hydrophilic silica nanoparticles leads to the formation of amphiphilic complexes, which can migrate to liquid interfaces and thus form interfacial layers [18–20]. These layers are characterized by properties, which depend on their nanoscale structure. To investigate these interfacial properties measurements of Neutron Reflectivity on interfacial liquid-liquid layers between SiO_2NP dispersions in water, CTAB (cationic surfactant), and dodecane are conducted. This study aims mostly to understand the difference in the organization of the surfactant within the interfacial layer and its distribution between the interfaces.

Neutron reflectometry is specifically employed in this context to investigate the layers of nanoparticles and surfactants at the liquid-liquid interface. The time-of-flight instrument employed for this purpose is FIGARO (Fluid Interfaces Grazing Angles Reflectometer - https://www.ill.eu/users/instruments/instruments-list/figaro/description/instrument-layout) [21], which operates at the ILL (Institute Laue-Langevin) facility in Grenoble, France.

This investigation exploits a key characteristic of neutrons: their significant contrast in nuclear scattering length between hydrogen and deuterium. Thus, selective deuteration enables the analysis of complex structures and the identification of distinct components within the system. By employing multiple isotopic contrasts, the technique allows for the gradual differentiation of scattering contributions from various components. This deuteration process significantly enhances the resolving power of neutron reflectometry, enabling deeper insights into complex structures. Then, neutron reflectometry is a technique utilized to precisely analyse the nuclear and magnetization distribution within a thin film at the nanoscale. By employing a well-collimated

monochromatic neutron beam, the sample's surface is impinged at a defined and small angle. This incident beam undergoes specular reflection, causing a partial refraction of the exit angle within the material. In scenarios where multiple layers exist on the substrate, both reflection and refraction occur at the surface and interfaces. Consequently, the rays reflected by different interfaces can interfere with each other, particularly when the layer structures possess dimensions comparable to the wavelength of neutrons [22]. In these experiments, the measured quantity is the reflectivity as a function of the scattering wave vector, denoted as Q, which is oriented perpendicular to the surface of the sample.

Neutron reflectivity primarily provides a description of the scattering length density (SLD) profile at the interface and within the depth of the sample. To initiate the experiment, certain initial information is required, such as the SLD values for the different components of the sample and the mean and distribution of the size of suspended particles.

The relationship between the scattering moment and the scattering length density is established by incorporating the critical angle of total reflection. This critical angle serves as a crucial link connecting these parameters:

$$Q_c = 4\pi/\lambda sin(\theta_c) \sim 4\pi/\lambda \cdot \theta c \sim 4\pi\sqrt{(\rho/\pi)} \tag{1.5}$$

This enables the calculation of the Fresnel reflectivity coefficients, denoted as the ratio of the number of neutron reflections to the number of incident neutrons, in terms of the scattering vector Q. Below the critical angle, the reflectivity decreases as the fourth power of the scattering vector. In the experimental context, the reflectivity obtained is combined with the resolution function in Q, incorporating the width defined by δq [23]. This width encompasses the angular divergence and the propagation of the wavelength. The resulting reflectivity, convoluted with the resolution function, provides a more accurate representation of the experimental measurements.

The interference phenomenon in Q space relates to the length scales of real space reciprocally. These interference phenomena in reflectivity curves lead to reflectivity periodic decreases, characterized by oscillations known as Kiessig fringes. The effects of the interfacial roughness are observed through a reduction in reflectivity at higher transferred wave vectors, and the decay is modulated by the Debye-Waller factor:

$$R_{rough} = R_{flat} \cdot \exp(-4\sigma^2 k^2) \tag{1.6}$$

which quantifies the mean quadratic shift (σ^2) of the interface diffusion from the position of a flat interface.

In view of the Neutron Reflectometry (NR) experiment, the samples were prepared with a suspension of silica nanoparticles (Levasil 200A/30, Nouryon, highly hydrophilic and solely stabilised by surface charge) in 1 wt% water, CTAB (https://www.sigmaaldrich.com/IT/it/product/sigma/h6269) surfactant and dodecane oil (Dodecane-d26,98 atom%D https://www.sigmaaldrich.com/IT/it/product/aldrich/489131). In this study, the same approach mentioned above is adopted, utilizing four distinct isotopic contrasts, each involving heavy water as the aqueous phase. Due to the large incoherent scattering cross section of hydrogen, it is essential to avoid propagation of the neutron beam for long paths in normal water. Therefore, deuterated water (D_2O) is chosen as the aqueous phase. The following isotopic contrasts have been investigated:

a) H-CTAB / oil matched NP. Silicon matched oil and hydrogenated surfactant (mainly SiNP and surfactant contribute to the NR signal)
b) H-CTAB / H-oil (dodecane). Hydrogenated oil and hydrogenated surfactant (all components contribute to the NR signal)
c) D-CTAB / oil matched NP. Silicon matched oil and deuterated surfactant (most of the NR signal derived from SiNP only).

d) D-CTAB / H-oil. Hydrogen oil and deuterated surfactant (mostly liquid interface and SiNP contribute to NR signal)

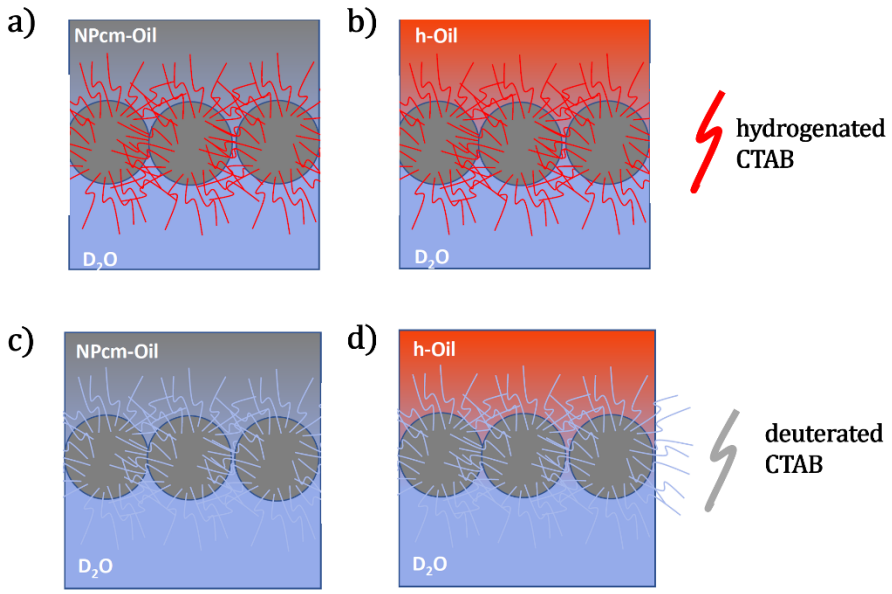

Figure 1.3 NR contrast scheme. Partial hydrophobicity is induced by the adsorption of CTAB to the surface of NP, thus NP-CTAB complex adsorbs to the liquid-liquid interface. Respectively in the panel: a) hydrogenated CTAB and silica - matched oil b) hydrogenated CTAB and hydrogenated dodecane c) deuterated CTAB and silica matched oil d) deuterated CTAB and hydrogenated dodecane.

A first estimate of particle size distribution can be obtained by DLS. To interpret DLS results, the optical refractive index of the particles is needed. This was determined by index matching: a liquid mixture of water and thiodiglycol in varying proportions is chosen, to cover the range of refractive index from 1.33 to 1.47. The results in figure 1.4 show n=1.47, which is substantially lower than pure silica. This is a well-known effect in this type of NP, typically due to porosity in the structure. By comparing with the existing literature [24] the gravimetric density of the nanoparticles can be determined (2.1 g/cm^3) which implies that 80% of the NP is composed of SiO_2, the rest being filled by water.

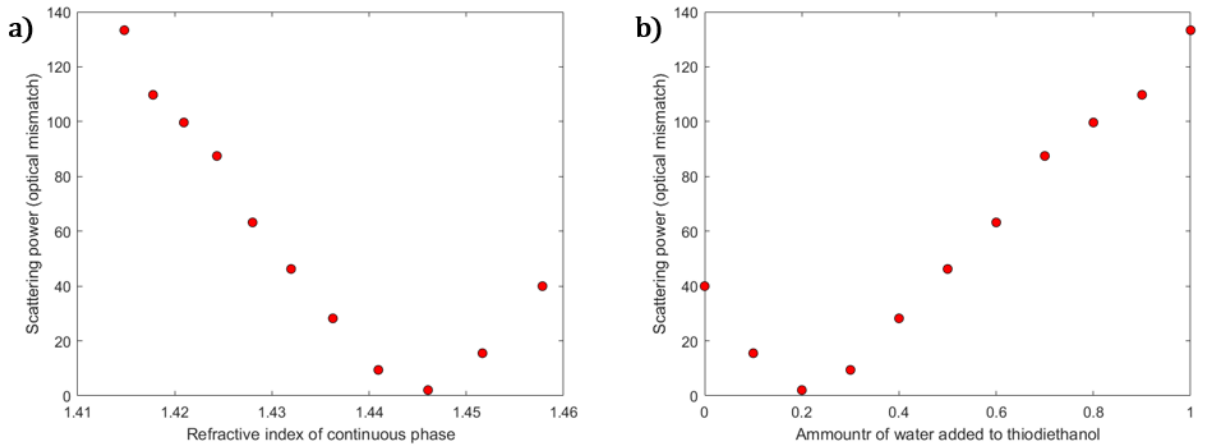

Figure 1.4 One method of measuring the refractive index of particles is to suspend them in a liquid with a variable refractive index and look for the minimum of the diffuse intensity corresponding to index matching. a) Scattering intensity (count rate per second) according to the refractive index of the water-thiodiglycol

suspension with silica nanoparticles. b) scattering intensity as the percentage of water added to thioglycol varies to find index matching.

To gain better insight into NP size distribution, preliminary studies are also made, via SANS (Small Angle Neutron Scattering - D11, ILL facility) and SEM (Scanning Electron Microscope-FEG Zeiss SUPRA-40, University of Parma).

Small-angle scattering (SAS) is a diffusion-based technique that involves the slight deflection of collimated radiation from its straight path after interacting with structures significantly larger than the wavelength of the radiation. This technique provides valuable information about the size, shape, and orientation of structures within a sample. In the case of small-angle neutron scattering (SANS), the measured quantity is the scattering intensity, represented as I(Q), which is a function of the transferred momentum. The scattering intensity is expressed as

$$\mathrm{I(Q)} = \mathrm{S(Q)P(Q)} \cdot \mathrm{V}\phi\Delta\rho \tag{1.7}$$

where S(Q) corresponds to the structure factor, specifically in our case, considering hard spheres with varying interaction potentials. P(Q) represents the form factor, which is assumed to be spheres with a lognormal size distribution (obtained from the Fourier transform of the particle size distribution in real space). $\Delta\rho$ is the contrast variation between silica and heavy water in terms of scattering length density ρ (SLD). This contrast, $\Delta\rho$, is given by $\Delta\rho = \rho_{solvent} - \rho_{particles} = \phi\rho_{np} + (1-\phi)\rho_{D_2O}$, where ρ_{np} represents the SLD of the nanoparticle, and ϕ denotes the volume fraction of nanoparticles. By fitting analyses, it is observed that the average nanoparticle radii is approximately 65 Å, with $\sigma = 0.36$. A weight fraction of 1% is employed, corresponding to a volume fraction of 0.48%. Furthermore, a scattering length density of $\rho = 4.6 \cdot 10^{-6}\text{Å}^{-2}$ is determined. The curve for the complex silica nanoparticles and CTAB exhibits a similar pattern, slightly steeper in the Guinier limit at small, transferred momentum Q. This scattering behaviour can be described by the equation $I(Q) = I_0 \exp\left(-R_g^2 \cdot \frac{Q^2}{2}\right)$ where R_g represents the radius of gyration.

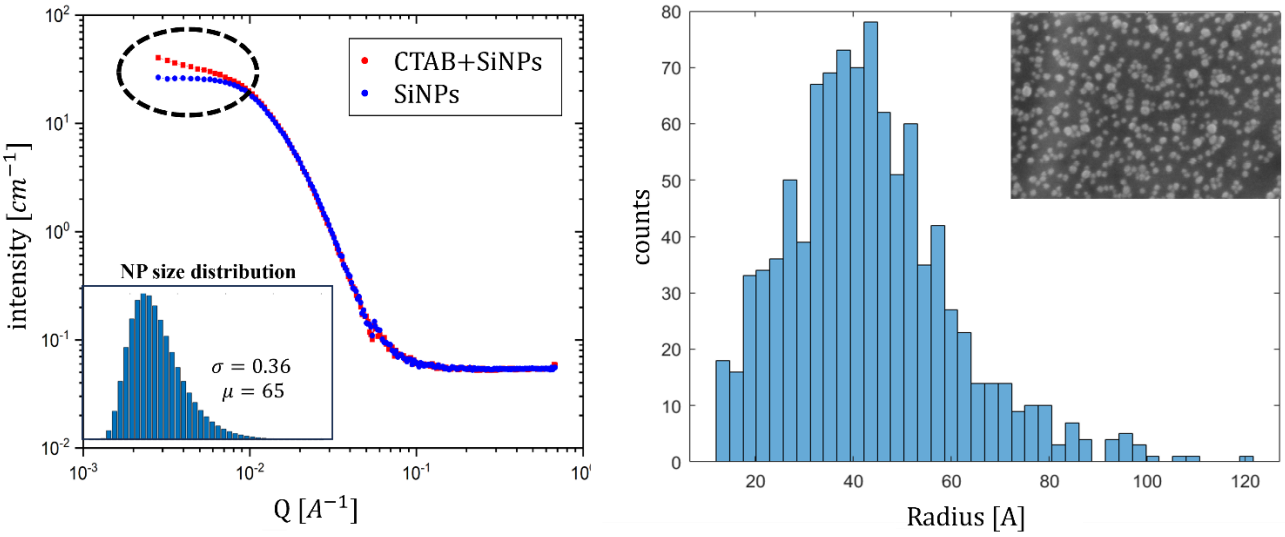

Figure 1.5 In panel a) is represented the SANS curve of only suspended nanoparticles (blue line) and complex nanoparticles plus CTAB 200 μM dispersion (red line). A fairly large radii distribution of nanoparticles with an average radius of about 66 Å is obtained. There is also evidence of the formation of low Q aggregates for the sample with CTAB plus silica nanoparticles (black circle). In panel b) the size distribution of silica

nanoparticles obtained from SEM analysis. Also, in this case, there is evidence of polydispersity and a peak around 50 Å.

The acquired sample images obtained through scanning electron microscopy (SEM) were subjected to analysis. The examination revealed a dispersed distribution of nanoparticle (NP) radii, with a predominant peak around 50 Å. It is important to note that this distribution does not entirely align with the results obtained from small-angle neutron scattering (SANS) data. Factors such as size distribution, agglomeration distribution, and the presence of concatenated particles are not considered during the SEM analysis. However, it does emphasize the polydispersity of the sample, indicating variations in particle sizes.

To initiate the measurement, the transmitted beam is initially assessed, and the experimental setup is aligned. Reflectivity curves are then recorded for various conditions, including reflection from air, the solution (consisting of 1% silica nanoparticles and CTAB solution with $2 \cdot 10^{-4} M$ in D_2O), and the liquid-liquid interface, at two distinct angles, denoted as θ_1 and θ_2.

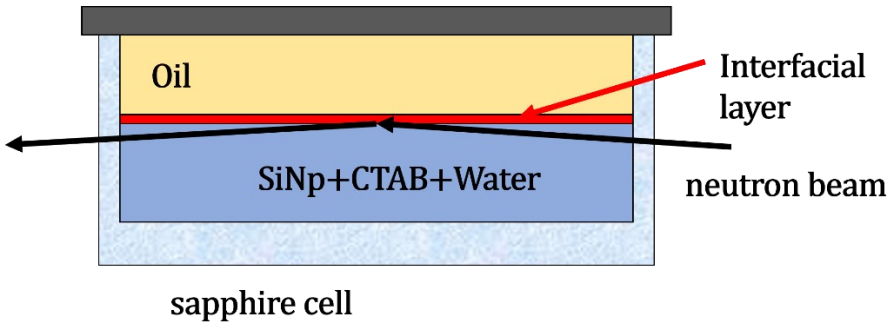

Figure 1.6 Scheme of the sapphire cell used for neutron reflectometry experiments. The collimated neutron beam impinges, at a well-defined and small angle, the surface of the sample at the water/oil interface. This is partially reflected and refracted from the interfacial layer and is collected by the detector.

During the experiment, data collection is conducted at two distinct detector angles, corresponding to large and small values of Q. This approach enables the acquisition of a reflectivity curve that spans the entire Q range, providing comprehensive information about the sample's scattering behaviour. The critical angle SLD estimates, reveal a surface scattering length density (SLD) of $\rho \sim 6.12 \cdot 10^{-6}\ \dot{A^{-2}}$ for the aqueous phase and an SLD of $\rho \sim 3.5 \cdot 10^{-6}\ \dot{A^{-2}}$ for the oil phase, as expected.

In this thesis, I primarily focus on presenting preliminary studies and the raw data obtained during the experiment conducted at ILL. Unfortunately, the continuation of this study became unfeasible due to the transition to a new project, which I will unravel in the following chapters, as the central focus of this thesis.

However, based on the assumed microscopic model of the interfacial layer, the following considerations are made:

- The liquid-liquid interface is assumed to be rough, with appropriate roughness characteristics.
- NP-CTAB complexes are attached to the oil/water interface, exhibiting an average contact angle that is a fitted parameter.
- The size distribution of NPs is fixed to the SANS results (lognormal distribution with an average radius of 65 Å and σ=0.36)
- The CTAB layer at the interface is estimated to have a thickness of 21 Å, corresponding to the extended molecule.

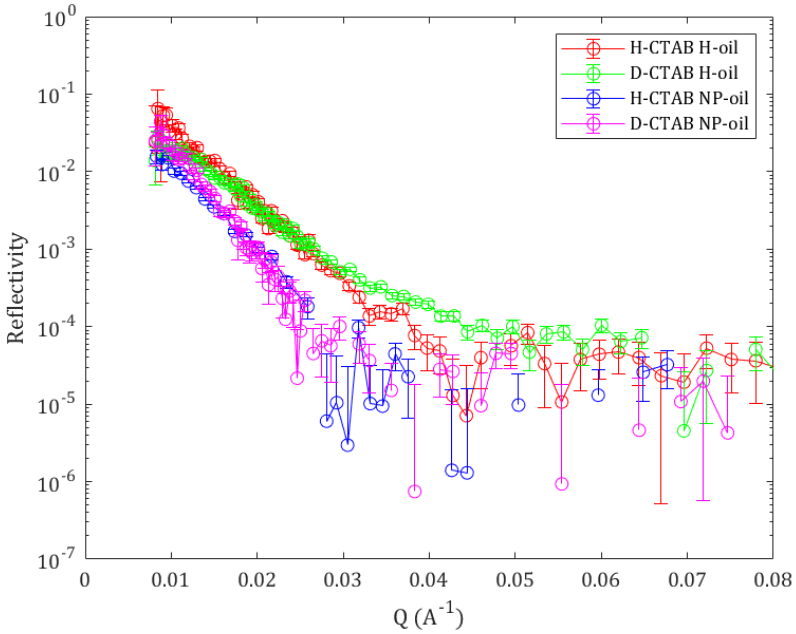

Figure 1.7 Reflectivity curves from raw data acquired in the neutron reflectometry experiment on FIGARO. Each curve represents the reflectivity for the four isotopic contrasts investigated.

From these studies emerges the presence of a rough liquid-liquid interfacial layer, which is attributed to the presence of nanoparticles attaching to the interface. This finding highlights the complexity of the interfacial layer and the role of nanoparticles in its structure. Therefore, the information derived from the preliminary studies serves as a solid foundation for the development of an advanced model that will contribute to unravelling the intricacies of mixed particle-surfactant layers. To gain a more comprehensive understanding, further investigations using neutron reflectometry are necessary. These investigations would help refine existing models and provide more insights into the structural details, including the characterization of the CTAB shell in the adsorbed complexes.

2. Multiple liquid interfaces: emulsions

Emulsions, which are liquid-in-liquid dispersions, hold significant technological importance [25]. Ordinary emulsions consist of droplets ranging from nanometric to micrometric sizes dispersed within a liquid matrix. However, these emulsions are thermodynamically unstable, leading to a tendency for their liquid phases to separate. The kinetic stability (chapter 2.1) of emulsions relies on the presence of emulsifiers, which are mixtures of surface-active substances (chapter 1.1) such as short-chain surfactants, polymers, proteins, and even nanoparticles. These emulsifiers adsorb at the liquid-liquid interface, reducing the energy required for the creation of new interfacial area and appropriately modifying the chemical, physical, and mechanical properties of the interface [7–9]. This modification counters the destabilization mechanisms (chapter 2.3). Conversely, other additives known as de-emulsifiers can be employed to counteract the stabilizing effects of already-present surface-active substances, particularly in natural emulsions, to destabilize the emulsion and cause phase separation.

In the past three decades, there has been notable advancement in comprehending the kinetic destabilization of emulsions and other multiphase systems (chapter 2.2), as well as the influence of surfactants on stabilization. Despite these progresses, several aspects of this field remain unclear, necessitating further investigation. As a result, the development of emulsifiers or de-emulsifiers still heavily relies on empirical methods, highlighting the need for additional research to achieve a comprehensive understanding of these processes.

This research is associated with the EDDI project (Emulsion Dynamics and Droplet Interface, chapter 2.4) conducted under a contract with the European Space Agency (ESA). The primary objective of this project is to investigate the influence of surfactants on emulsion formation and stability, with the ultimate goal of minimizing and optimizing the amount of emulsifiers required. To achieve this, experiments are conducted in a microgravity environment onboard the Columbus module of the International Space Station (ISS), specifically within the Fluid Science Laboratory. This facility houses a dedicated Experimental Container known as "Soft Matter Dynamics" (SMD) for conducting these experiments.

2.1 Stability, morphology, and dynamics

A wide range of natural and synthetic products fit into the category of emulsions, including food, cosmetics, pharmaceuticals, and household items, among others. Emulsions can be defined as metastable dispersions of one liquid within another, with droplets ranging in size from nanometers to micrometers and beyond. In this context, the examination will centre on "ordinary" emulsions (or mini emulsions) characterized by thermodynamic instability. These emulsions are typically classified based on the nature of their continuous phase: Oil-in-water emulsions, where oil droplets are dispersed within a continuous aqueous phase and water-in-oil emulsions, if water droplets are dispersed within a continuous oil phase.

The formation of emulsions requires certain conditions:

- Energy must be applied to a mixture of immiscible or mutually insoluble liquids. This energy input leads to a deformation and subsequent fragmentation of drops into smaller droplets. This instability arises from the product of the Interfacial energy per area and the new area produced by breaking large volume drop into small volume drops. This results in an increase in surface area per unit volume as the size decreases.
- Surface-active agents, such as surfactants, polymers, proteins, particles, or their combinations, play a key role in facilitating emulsification. These agents adsorb at the liquid-liquid interface, reducing the

energy required to create a new interfacial area. They also modify the chemical, physical, and mechanical properties of the interface, thereby countering destabilization mechanisms.

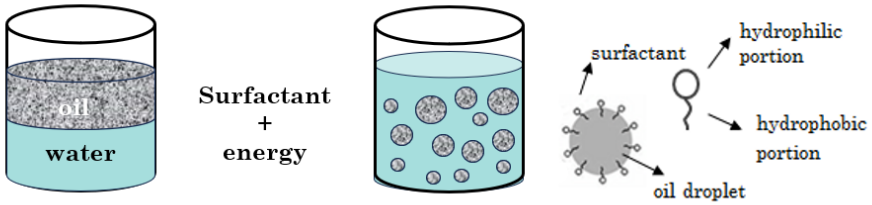

Figure 2.1 Example of an oil-in-water emulsion obtained by adding a surfactant, which adsorbs at the droplet surface.

Another type of water-oil emulsions are the so-called double emulsions. Double emulsions can be defined as emulsions composed of smaller emulsion droplets, simultaneously featuring both oil-in-water (O/W) and water-in-oil (W/O) emulsion phases. Two primary types of double emulsions exist: water-in-oil-in-water (W/O/W) and oil-in-water-in-water (O/W/O), with the former being more commonly prepared. The appeal of double emulsions lies in their ability to encapsulate and safeguard active ingredients within the internal emulsion droplets [26,27]. To fully harness the potential applications of double emulsions, it is vital to not only comprehend how to formulate stable structured emulsions but also to strategically destabilize the structure to facilitate the controlled release of active ingredients. The mechanisms underlying the destabilization of double emulsions share similarities with those for single emulsions but encompass a range of different combinations. However, due to the presence of two distinct interfaces, achieving stability in double emulsions necessitates a delicate balance of lipophilic and hydrophilic emulsifying agents [28].

The process of emulsification and the stability of emulsions are influenced by several factors, including the addition and type of emulsifiers, density and viscosity of the continuous phase, droplet size distribution, oil/water ratio, temperature, intensity, and duration of mechanical stirring. Analysing the relationship between destabilization processes and the physical property of the interface is crucial for achieving stable emulsions. Due to the complexity of these systems, a comprehensive characterization often requires the use of different experimental techniques.

The efficiency of an emulsifier depends on how the interfacial film formed between the two liquids minimizes their contact, coalescence, and aggregation. Moreover, the concentration of the surfactant plays a role in emulsion stability. There exists a concentration window where the emulsion volume decreases due to the agglomeration of oil droplets at low concentrations or coalescence phenomena at high concentrations. The optimal packing and long-term stability of the emulsion can be achieved at a specific emulsion fraction, which depends on the oil-water ratio. Studies have shown that increasing the intensity of emulsification and the duration of the process leads to a decrease in the average droplet size. However, there is an optimal emulsification time for each emulsion beyond which further improvement is minimal, as emulsifiers may start to leave the oil-water interface [29]. Temperature also plays a role in emulsification, as both interfacial tension and viscosity decrease at higher temperatures, so emulsifying temperature influences the adsorption of emulsifiers at the interface.

2.2 Other multiphase systems: Pickering emulsions, Bubbly emulsions, and Solid foams

A multiphase system refers to a physical system that consists of two or more distinct phases or states of matter coexisting within it. Each phase represents a region or portion of the system with uniform physical and chemical properties. The phases can be in different states of matter, such as solid, liquid, or gas, or they can be combinations thereof. In a multiphase system, the phases are separated by interfaces, which can be well-defined boundaries or transitional regions where the properties change gradually. A common example of a multiphase system is a mixture of oil and water (traditional emulsions). Other examples include a suspension of solid particles in a liquid (as Pickering emulsion), where the solid particles represent a separate solid phase dispersed within the liquid phase, or a gas-liquid system, such as bubbles in a liquid or droplets in a gas (bubbly emulsions and foams).

Multiphase systems are prevalent in many fields, including physics, chemistry, materials science, engineering, and biology. Understanding and characterizing multiphase systems is important for studying various phenomena, such as phase transitions, interfacial behaviour, mass transfer, heat transfer, and chemical reactions. The behaviour and properties of a multiphase system are influenced by factors like phase composition, phase distribution, phase interactions, interfacial tension, and the dynamics of phase change processes. Analysing and manipulating multiphase systems often involves studying the interactions between the phases, the stability of the system, and the transport of mass, energy, or momentum across the phase boundaries. Overall, multiphase systems are complex and diverse, and their study is crucial for understanding many natural and engineered processes and systems that involve the coexistence of distinct phases.

Below is a concise introduction about two fascinating areas of research that have captured the interest of my research group: Pickering emulsions and solid foams. These subjects hold particular significance in my PhD studies, where I delved into analysing interfacial studies involving nanoparticles and surfactants (chapter 1.3), seeking to unravel the intricacies of Pickering emulsions. Additionally, my research group has been actively involved in studying solid foams as part of the comprehensive SPUMA project (see chapter 8), focusing on Solid Foam Photocatalytic Multiscale Filters.

In a Pickering emulsion [18,20,30–32], solid particles, such as colloidal particles or nanoparticles, are used together with surfactants to stabilize the emulsion. These solid particles adsorb at the oil-water interface, creating a physical barrier that prevents the coalescence of the droplets The primary factor driving particle segregation at the fluid interface is partial wetting. This phenomenon can be effectively harnessed by modifying the wetting characteristics through physical alterations to the particle's surface or by introducing surfactants for adsorption on the particle's surface. A compelling model suggests that particles with partial hydrophilicity and contact angles exceeding 90 degrees enjoy a favourable energy advantage, encouraging them to remain stably positioned on the liquid-liquid interface. This dynamic equilibrium between contact angles and energy gains can lead to a state where particles become irreversibly anchored to the liquid-liquid interface.

The particles form a shielding layer around the droplets, providing stability to the emulsion. The stabilization mechanism in Pickering emulsions is based on the balance between the interfacial tension concerning the two immiscible liquids and the mechanical resistance provided by the solid particles. The particles adsorb at the oil-water interface due to their amphiphilic nature or surface properties, creating a stable network that hinders droplet coalescence. Pickering emulsions have attracted significant attention due to their potential advantages over traditional emulsions. They offer improved stability, as the solid particles provide a more robust and rigid interface. Additionally, Pickering emulsions can offer enhanced control over droplet size, rheological properties, and functionality compared to conventional emulsions.

A solid foam, also known as a porous solid, is a material that consists of a solid matrix with a significant volume fraction of pores distributed throughout its structure. These pores can be interconnected or closed, and they give the material its foam-like appearance. Solid foams are typically created by introducing gas bubbles into the liquid or molten state of the material, followed by solidification, or curing. The gas bubbles become trapped within the material, forming the voids. Various techniques can be used to produce solid foams, including foam casting, foam blowing, and foaming agents. The properties of solid foams depend on factors such as the material composition, pore size, pore distribution, and the connectivity of the pores.

Solid foams have several desirable characteristics that make them useful in a wide range of applications. These characteristics include low density, high strength-to-weight ratio, thermal isolation, acoustic absorption, shock absorption, and buoyancy. Solid foams find applications in industries such as construction, automotive, aerospace, packaging, insulation, furniture, and sports equipment. The specific properties and applications of a solid foam can vary depending on the material used and the manufacturing process employed. Different materials and techniques can result in foams with varying densities, pore sizes, mechanical properties, and functionalities, allowing for the design of the foam properties to meet specific requirements.

It is necessary to mention the significance of bubbly emulsions, as extensive research has been devoted to understanding and addressing the issue of air bubbles within emulsions. Notably, the PASTA experiment and the EDDI project (Emulsion Dynamics and Droplet Interfaces), as highlighted in chapter 5-6, have delved into investigating bubbly emulsions on ground and on board the International Space Station (ISS). These activities have shed light on the dynamics of emulsion systems and the behaviour of droplet interfaces, further contributing to our understanding of bubbly emulsions.

A bubbly emulsion, is a type of emulsion that contains gas bubbles dispersed within a continuous liquid phase. It combines the characteristics of both emulsions and foams, where the dispersed phase consists of gas bubbles rather than droplets of another liquid. These characteristics of bubbly emulsions make them both challenging and intriguing systems to study. The presence of air bubbles introduces complexities that require special attention in their treatment and analysis. However, it is precisely these complexities that make bubbly emulsions highly fascinating and worthy of investigation. Their intricate behaviour and properties offer rich opportunities for scientific exploration and potential applications.

In a bubbly emulsion, the gas bubbles are typically formed and stabilized by surfactant molecules or other emulsifying agents present in the system. These surfactants reduce the interfacial tension between the gas and liquid phases, allowing the bubbles to form and be dispersed throughout the liquid. The presence of gas bubbles in the emulsion imparts unique properties and behaviour to the system. Bubbly emulsions often exhibit increased apparent viscosity compared to their non-foamed counterparts, as the gas bubbles contribute to the overall system volume and alter its rheological properties. Their stability, as with traditional emulsions, can be influenced by factors such as surfactant concentration, pH, temperature, and the presence of other additives. Bubbly emulsions find applications in various industries and fields. For example, in the food industry, they are used to create foams in products like whipped creams, mousses, and foam toppings. In cosmetic formulations, bubbly emulsions can provide enhanced texture and sensory attributes to creams, lotions, and shaving foams. They are also utilized in pharmaceuticals, where they can serve as carriers for drug delivery systems or as foaming agents in oral solutions or topical products.

Previous investigations have primarily focused on the general aspects of bubbly emulsion systems, without delving into the intricate interactions between bubbles and droplets [33,34]. One notable phenomenon observed in these systems is the formation of drop-bubble aggregates, which, under normal gravitational conditions, are subject to creaming. The stability of these aggregates relies on the balance between wetting forces and drag forces induced by the shearing motion of the continuous phase.

In microgravity environments, the shearing motion diminishes, and capillary forces become the dominant driving force in bringing bubbles and drops together. Although considerable progress has been made in simulating two-phase systems using reliable algorithms that account for capillarity [35,36], the simulation of three-phase systems involving capillary phenomena remains a challenge. The computational complexity, coupled with the substantial density disparity between gases and liquids, often leads to artificial effects that hinder accurate simulations. Microgravity studies offer a valuable platform for developing and testing numerical algorithms that effectively incorporate capillary effects into the dynamics of three-phase systems. For instance, simulations of bubbly emulsion evolution under "weightlessness" conditions predict that local coalescence events trigger abrupt flows in the continuous phase, resulting in coalescence cascades and heightened system instability. Advanced techniques leveraging the interpretation of multiply diffused light, particularly through multi-speckle detection utilizing the CMOS line camera (LC) available on the Soft Matter Dynamics (SMD), prove instrumental in effectively detecting and investigating these intermittent dynamics associated with coalescence.

2.3 Mechanisms of destabilization

Stable emulsions exhibit consistent behaviour over time, maintaining a uniform distribution of droplets in the continuous medium and a constant drop size distribution (DSD). In emulsions where the droplets are in the micrometric range and the constituting liquids have different densities, phase separation can occur due to gravity sedimentation or creaming. In contrast, emulsions with a submicrometric DSD often display long-term stability, as they reach a diffusion-sedimentation equilibrium. As depicted in figure 2.2, various mechanisms can contribute to an increase in droplet sizes, leading to gravity sedimentation or creaming and destabilizing the emulsions.

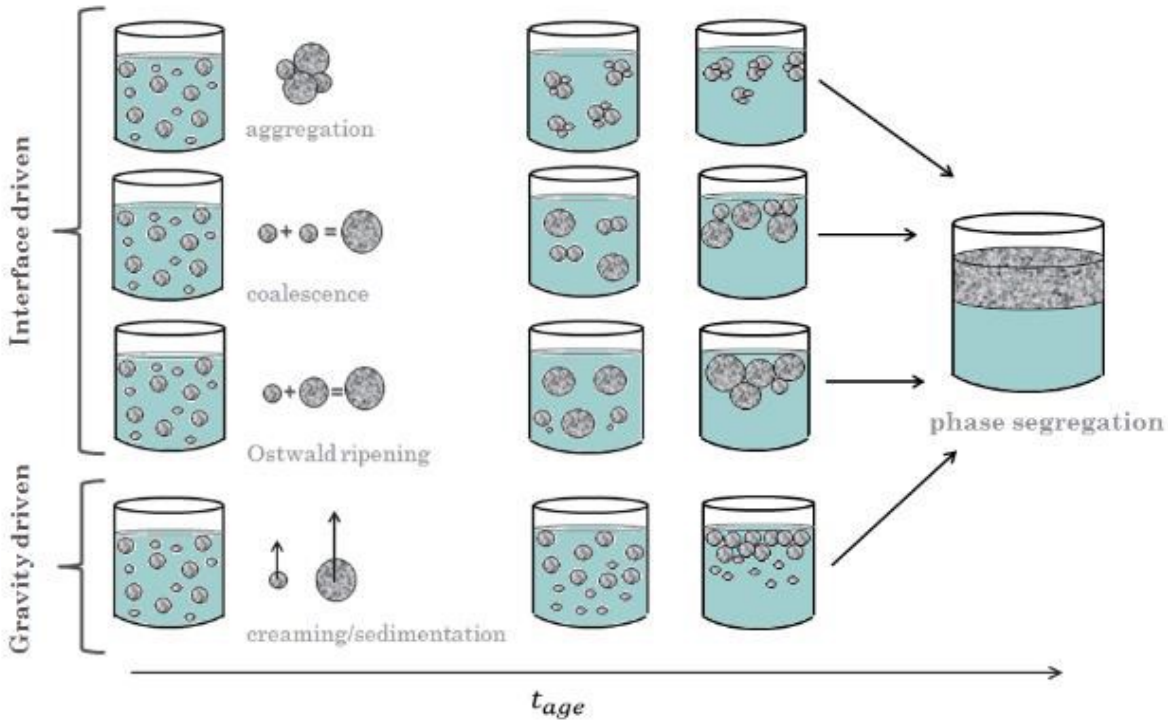

Figure 2.2 Illustration showcasing the mechanisms involved in emulsion destabilization.

The destabilization of an emulsion involves two distinct factors: interface-driven phenomena, such as aggregation, coalescence, or Ostwald ripening, and gravity-driven phenomena (creaming/sedimentation). In both cases, during the initial stages of the emulsion's aging, the behaviour resembles that of a Brownian motion regime. However, as the emulsion ages, the dominance shifts to a gravitational regime. This transition triggers the segregation of the droplets, resulting in phase separation during the later stages of the process.

1. Droplets have the potential to **aggregate**, forming either reversible or irreversible arrangements, with a stable film of the continuous phase separating them. As the aggregates grow in size, gravity causes them to segregate and eventually undergo phase separation. The phenomenon of aggregation arises due to molecular interactions between two or more droplets, which are influenced by various factors such as the properties of the liquids, the presence of surface-active molecules, and the condition of the interface [37].

2. Larger droplets, with a higher susceptibility to gravity segregation, can form when smaller droplets interact and undergo spontaneous **coalescence**. The coalescence phenomena are closely connected to the stability of the liquid film between the droplets. Thinning of this film can lead to direct rupture and droplet merging or the formation of a stable film, as seen in stable drop aggregates [38]. Consequently, preventing or promoting emulsion destabilization lies in the inhibition of film thinning, which poses a challenging problem involving the thermodynamic properties [39] and fluid dynamics of the film. The chemical-physical characteristics of the surfactant layer at the water-oil interfaces, such as dynamic interfacial tension and dilational viscoelasticity, play a significant role in this process [13,40–43]. The latter specifically quantifies the interfacial tension's response to changes in interfacial area [7], thus influencing the mechanical stability of the film when subjected to external disturbances. A high degree of elasticity, for instance, impedes thinning and enhances the stability of the liquid films. Coalescence and aggregation are fundamental mechanisms that retain their characteristics even in concentrated emulsions. Considering the role of surface-active substances in the stabilization/destabilization problem, investigating the impact of adsorption layers on the physical and chemical properties at the liquid-liquid interfaces becomes imperative in modeling aggregation and coalescence mechanisms in emulsions [1,3,44]

3. Under the influence of **Ostwald ripening** [45] , larger droplets grow at the expense of smaller ones. OR is a dynamic process driven by the difference in Laplace pressure within the droplets, leading to increased solubility of molecules in the smaller droplets [46]. The growth of droplet size, depending on the droplet packing, follows time dependencies between $t^{\frac{1}{2}}$ (concentrated emulsions) and $t^{\frac{1}{3}}$ (diluted emulsions) [47]. These time dependencies reflect extreme scenarios where diffusive exchange of molecules between droplets occurs either through the films between droplets or through the bulk of the matrix [47]. However, the situation becomes more complex in flocculated emulsions due to the presence of both types of transport. The interfacial tension, being proportional to the Laplace pressure in the droplets, plays a central role in driving the process. The presence of surfactants slows down or, in some cases, stops the Ostwald ripening process. Experimental studies conducted on droplets in the presence of surface-active molecules [2,39,43] support the theoretical prediction that Ostwald ripening ceases when the Gibbs elasticity, exceeds half of the surface/interfacial tension. However, these studies are still limited, and the substantial differences in Ostwald ripening rates observed with varying surfactant types and concentrations [48,49] have not been satisfactorily explained. In emulsions, where the mutual solubility between water and oil and the associated interfacial tensions are generally low, Ostwald ripening is typically slow and the criterion based on Gibbs' elasticity is rarely, if ever, met in practice [50].

However, gravity imposes limitations on emulsion formation and subsequent destabilization, such as the drainage of liquids. Moreover, creaming and/or sedimentation hinder the understanding of the individual processes involved in destabilization mechanisms, making the comprehension of emulsion hydrodynamics a challenging task.

2.4 Project EDDI 'Emulsions Dynamics and Droplet Interfaces'

The dynamic behaviour and evolution of emulsions result from the concurrence of different processes at different scales, from microscopic to macroscopic. All these mechanisms driving emulsion stability need to be investigated above the elementary process and in relation to the role played by the physiochemical properties of the droplet interfaces, which are induced and tuned by the presence of surfactants. The scientific state of the art provides only general principles, and many questions are yet open. Understanding of specific systems has been established, but generic mechanisms have not yet emerged. For many emulsions studied on Earth, gravitational separation is typically the dominant mechanism of destabilization and can obscure the other aging processes. Among them, in particular, are the coalescence mechanisms in low-surfactant-content emulsions, the droplet dynamics in the Ballistic and Brownian regimes, or coalescence event frequency. Microgravity offers a unique opportunity to investigate emulsion destabilization without ground-condition segregation. Microgravity experiments can provide evidence of the relations between the properties and the interfacial layers of droplets and their coalescence, allowing testing and developing models for emulsion stability and destabilization scenarios. The PASTA experiment, on board the International Space Station, is included in the project "Emulsion Dynamics and Droplet Interfaces-EDDI". It aims to push forward the comprehension of the features of these processes, decoupled from droplet creaming and properly modelled to establish their effects and links between them. To support the development of new concepts and sustainable and green methodologies in emulsion technology The PASTA experiment aims to address and evaluate the following key objectives (chapter 6-7):

1. Investigating and defining the conditions for coalescence (drop-drop) and aggregation/incorporation (drop-drop, drop-bubbles) between single droplets. This includes examining the characteristic time for droplet coalescence, considering the formulation of the emulsifiers, and studying specific dynamic regimes during emulsion destabilization. The experiment aims to measure the corresponding rates.

2. Studying the destabilization of emulsions and identifying the most involved processes, quantifying their frequency, and observing the evolution of droplet size. This research will help characterize the dynamic features of the emulsion and their effects on emulsion stability and destabilization.

3. Correlating the results of the investigations mentioned above with the development of models that account for the dynamic and structural aspects of adsorption layers. These models will consider potential surfactant exchange between liquid phases, which also needs to be investigated and incorporated.

To accomplish these objectives, the following steps will be taken:

1. Conceiving and designing the necessary DWS (Diffusing Wave Spectroscopy) experiments for investigating the above-mentioned points and for different types of emulsions (chapter 3).

2. Preparing the specifications for the first batch of experiments on emulsions that require minimal adaptations of the facility hardware (chapter 4).

3. Conducting ground-based studies on the samples that will be used in the experiment to establish a baseline and to evaluate the effects of the unique conditions experienced during the space mission (chapter 5).

4. Conducting a control experiment by using a standard. This control experiment serves as a reference point and allows for the assessment of any variations or deviations from the expected results (chapter 5).

By undertaking these steps, the PASTA experiment aims to enhance our understanding of emulsion behaviour, including droplet coalescence, aggregation, and destabilization processes. The results will contribute to the development of models that consider the dynamic and structural aspects of emulsion systems, including surfactant exchange, and improve our ability to control and manipulate emulsions for various applications (chapter 7).

2.5 Sample definition

The emulsions subject to investigation are a dispersion of Medium Chain Triglycerides (MCT oil, Migloyl 812N, IOI OLEO, Hamburg) in water (by varying oil/water fraction), with the non-ionic surfactant C12EO21 (Nikkol, Japan) stabilizing water/oil interface (at different molar concentrations).

A non-ionic surfactant is a type of surfactant that does not carry an electrical charge when dissolved in water or other solvents. In C12EO21 the hydrophilic portion contains polar functional ether (-EO-) groups. While the hydrophobic part consists of carbon chains. Due to their lack of ionic charges, these surfactants have several unique properties and applications:

- Lower toxicity: Non-ionic surfactants are generally considered less toxic compared to anionic or cationic surfactants, making them suitable for applications where milder formulations are desired.
- Good compatibility: Non-ionic surfactants are compatible with a wide range of other substances, including anionic, cationic, and other non-ionic surfactants. This compatibility makes them versatile in formulating various products.
- Stability: Non-ionic surfactants are stable over a broad range of pH levels, electrolyte concentrations, and temperatures, which makes them useful in different environments.
- Low foaming: Non-ionic surfactants typically exhibit low foaming properties, which can be advantageous in applications where excessive foam generation is undesirable.

MCT oil stands for medium-chain triglyceride oil. It is a type of dietary fat composed of medium-chain fatty acids (MCFAs). MCT oil is primarily derived from coconut oil or palm oil, although it can also be produced through industrial processes. The main components of MCT oil are three MCFAs: caprylic acid, capric acid, and sometimes a small amount of lauric acid. Furthermore, MCT oil exhibits exceptional compositional stability, devoid of any significant presence of surface-active compounds. MCT oil has gained popularity in recent years due to several potential health benefits.

C12EO21 is a water-soluble surfactant, and insoluble in oil, and has a critical micellar concentration of $\mathrm{CMC} \sim 2.4 \cdot 10^{-4}\, M$. The samples under investigation comprehend MCT-in-water emulsions, wherein stability is achieved through the employment of C12EO21 as a surfactant. Various combinations of water and oil fractions, along with different molar concentrations of surfactants below the CMC are employed. In preliminary ground studies, stable emulsions were observed within the molar concentration range of $10^{-4}M - 10^{-5}M$. The oil-

to-water fractions employed spanned from 20:80 oil-to-water to 30:70 oil-to-water and 50:50 oil-to-water (Table 1).

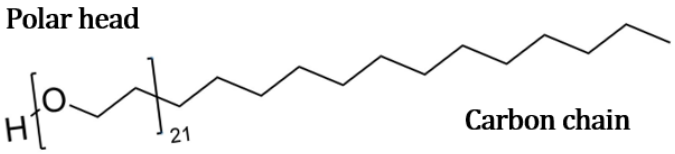

Figure 2.3 Model of the non-ionic surfactant C12EO21 polyoxymethylene alcohols. The hydrophilic head is represented by the ether group while the hydrophobic tail by a carbon chain.

In the context of preparing samples for the on-board experiment, another notable surfactant utilized is C10EO5, which belongs to the family of polyoxyethilenated alcohol surfactants. Like C12EO21, it possesses a surface-active structure. However, C10EO5 distinguishes itself by being soluble in both water and oil. Unfortunately, this thesis does not present any results about samples stabilized with C10EO5. The analysis of C10EO5-stabilized samples will be conducted in forthcoming studies.

Subsequent Table 1 contains detailed information regarding the standard sample and the precise arrangement of samples within the facility on board the ISS.

SCU	SAMPLE	SURFACTANT	CONCENTRATION [M]	V_{oil}/V_{water}
EM 09-	1	C12EO21	10^{-5} M	20:80
	2	C12EO21	$4 \cdot 10^{-5}$ M	20:80
	3	C12EO21	10^{-4} M	20:80
	4	C12EO21	$2 \cdot 10^{-4}$ M	20:80
EM 10-	1	C12EO21	10^{-5} M	30:70
	2	C12EO21	$4 \cdot 10^{-5}$ M	30:70
	3	C12EO21	10^{-4} M	30:70
	4	C12EO21	$2 \cdot 10^{-4}$ M	30:70
EM 11-	1	C12EO21	10^{-5} M	50:50
	2	C12EO21	$4 \cdot 10^{-5}$ M	50:50
	3	C12EO21	10^{-4} M	50:50
	4	C12EO21	$2 \cdot 10^{-4}$ M	50:50
EM 12-	1	C10EO5	$7 \cdot 10^{-4}$ M	50:50
	2	C10EO5	$9.9 \cdot 10^{-4}$ M	20:80
	3	Polystyrene latex particle dispersions in 45%-55% mixture of $D_2O - H_2O$		
	4	C10EO5	$4.4 \cdot 10^{-3}$ M	80:20

Table 1 The experimental test samples conducted on board the International Space Station (ISS) are documented in the table provided. The first column represents the SCU number (Sample Cell Unit), which corresponds to a specific set of samples, categorized based on the oil-to-water fraction. Within each SCU, four SCs (Sample Cells) are present, containing four distinct samples for each oil-to-water fraction (four for 20:80, four for 30:70, and four for 50:50). Each sample within these SCs is stabilized using varying concentrations of surfactant to maintain the emulsion's stability. The concentrations employed include, $4 \cdot 10^{-5}M$, $1 \cdot 10^{-4}M$, *and* $2 \cdot 10^{-4}M$. *The last SCU, on the other hand, has three SC containing the samples stabilized with C10EO5 and one SC containing the standard sample Polystyrene latex particle dispersions in 45%-55% mixture of* $D_2O - H_2O$.

3. Diffusing wave spectroscopy

3.1 Theoretical Background

Diffusing Wave Spectroscopy (DWS) is a powerful tool to investigating the dynamics, structure, and rheological properties of turbid samples, such as colloidal suspensions, foams, emulsions [51–53].
It does so by analysing the temporal fluctuations of "speckles" of coherent light scattered by the sample, with sub-microsecond resolution, employing autocorrelation functions. As such, the main advantage of DWS is its non-invasive character, which makes it ideally suited to investigate the ageing processes of emulsions and foams with high statistics (i.e. improved accuracy, high resolution of dynamic and statistical distribution information). The technique is also sensitive to small displacements from scattering centres and fast time scales, overcoming the limitations of the usual microscopic techniques. These advantages are weighted by the complexity of the analysis required to extract the relevant physical parameters from the measured intensity autocorrelation functions. For this reason, DWS was chosen as one of the diagnostic tools for investigations of granular materials, foams, and emulsions in microgravity in the "Soft Matter Dynamics" (SMD) instrument aboard the International Space Station [54].
The theoretical framework for DWS analysis has been detailed by D.J. Pine and D.A. Weitz [51,52]. Each detected photon has experienced several scattering events proportional to the length s of the light path it followed. The intensity of the speckle pattern, which results from the interference of all detected photons, fluctuates in time; its autocorrelation function is the sum of the overall decorrelation caused by the relative motion of the scattering centres that each photon met along its path, i.e., the internal dynamics of the sample, weighted by the distribution $P(s,l_*)$ of photon path lengths s, measured in units of the photon transport mean free path l_*. By analysing the correlation functions measured simultaneously in at least two different scattering geometries, it is possible to characterize the internal dynamics of the sample, and to measure l^*, which is related to structural information such as the size and interparticle distance of scattering centres.

3.2 Homodyne and Heterodyne methods

In optical mixing techniques, the scattered light impinges directly on the detector. In the homodyne method, only scattered light is used, while in the heterodyne method a local oscillator (usually a small portion of unscattered laser beam) is mixed with scattered light on detector surface [55] .The dynamics of the samples are probed by calculating the temporal autocorrelation function of the light intensity detected following the multiple scattering in the sample. This is directly related to the correlation of the electric field:

$$\langle I(t_0)I(t_0+t)\rangle \propto \langle |E_s(t_0)|^2 |E_s(t_0+t)|^2\rangle \tag{3.1}$$

The correlation function has a direct relationship with the Intermediate Scattering Function $f(\boldsymbol{q},t)$, which represents the spatial Fourier Transform of the van Hove Function $G(\boldsymbol{r},t)$, The van Hove Function encapsulates the entirety of the sample's structure and dynamics. In cases where the Gaussian approximation holds true, meaning that numerous independently fluctuating volumes are probed, the two correlation functions are connected through the Siegert relation.

$$g_2(t) = \frac{\langle I(t_0)I(t_0+t)\rangle}{\langle I\rangle^2} = 1 + \beta[g^1(t)]^2 \tag{3.2}$$

A baseline and contrast β are introduced from Siegert relation, representing the plateau and amplitude of the correlation function's decay.

Precise determination of these parameters is crucial, particularly for the baseline, which necessitates a significantly longer measurement time, spanning at least two decades longer than any characteristic time scale of the sample. This extended measurement time is essential to ensuring the complete decorrelation of the function.

The g_2 function in the heterodyne method is proportional both to the scattered electric field E_s and local oscillator electric field E_{LO}. With the assumptions that the fluctuations of the local oscillator field are negligible $|E_{LO}(t)| \gg |E_s(t)|$ and the two fields are statistically independent $\langle I_{LO} I_s \rangle = \langle I_{LO} \rangle \langle I_s \rangle$, heterodyne correlation function is written as a sum of the intensity of the local oscillator signal and a term that is the real part of complex single exponential and contains relaxation times.

$$\langle I(t_0) I(t_0 + t) \rangle \propto \langle |I_{LO}^2 + 2 I_{LO} Re I_1(t)| \rangle \tag{3.3}$$

With intensity of the local oscillator signal $I_{LO} = \langle |E_{LO}|^2 \rangle$ and $I_1(t) = \langle \boldsymbol{E}_s^*(t_0) \boldsymbol{E}_s(t_0 + t) \rangle$.

It is quite common to find systems where an organized flow of matter coexists with the Brownian motion of individual particles. Examples of such systems include aerosols, particle suspensions, and emulsions that experience externally induced flow, convective flow, or gravity-driven sedimentation or creaming. Light scattering spectroscopies have long been used to characterize these systems since their inception. The motion characterized by a constant velocity is frequently referred to as "ballistic". Dynamic Light Scattering (DLS) represents the simplest scenario where light undergoes a single scattering event before detection. In this case, it is possible to directly measure the flow velocity when experiments are conducted in heterodyne mode, provided that the velocity $\boldsymbol{v}$ possesses a non-zero component along the exchanged momentum $\boldsymbol{q}$. The decay of the correlation function is modulated by an oscillating term, which is generated by the Doppler shift. Specifically, in the presence of both ballistic and Brownian motion, the correlation function can be expressed as $g_1\,(q,t) \propto \exp\,(-q^2\,Dt)\cos\,(q \cdot vt)$, where D represents the diffusion coefficient.

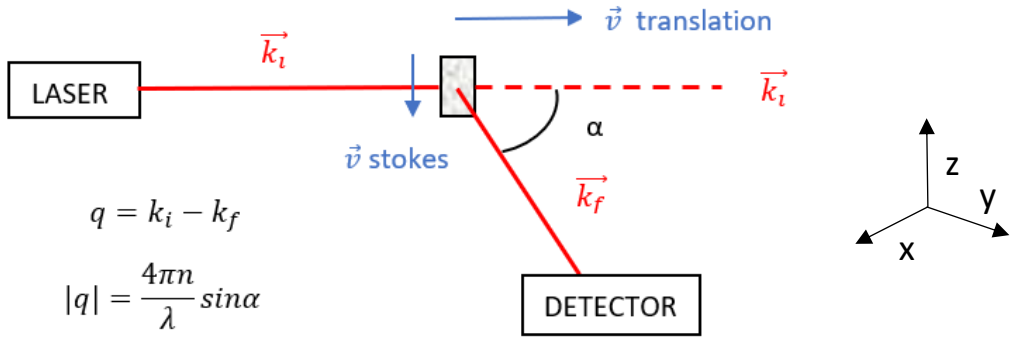

Figure 3.1 A schematic representation of light scattering experiment in Homodyne configuration, where xy indicates the scattering plane.

In simple homodyne setup, the light from a polarized He-Ne laser (λ=632.8 nm, illumination power 50 mW, LGK 7665, LASOS Lasertechnik GmbH) is expanded by two lenses in a beam-expander configuration, to obtain uniform illumination on the cuvette side. The sample is placed in a wide quartz cuvette 0.48×1.8×3.6 cm. The light front impinges perpendicularly on the side of the cuvette. Cuvettes were placed in 3D-printed custom-made sample holder. The sample holder presents supports to accommodate a fiber-optic collimator for backscattering (BS) and forward (FW) acquisition. In BS geometry, the light is collected from the centre of the cuvette side, uniformly illuminated by the expanded laser beam. In front of the collection optics, a linear analyser extinguishes light polarized parallel to the incident beam polarization, likely reflected from the cuvette side. The scattered light collected either in BS or FW geometry is sent by fiber optics via 1x2, 50:50 wideband

fiber coupler (Thorlabs) to two single photon counting modules (Hamamatsu C13001-01) in cross-correlation configuration. The signals from the two detectors are then fed to a FPGA correlator based on a Xilinx SP605 board, which computes the autocorrelation function.

For the heterodyne configuration setup, two main factors must be taken into account: the space-time coherence and the coherence area. The contrast of the correlation function usually depends on the signal-to-noise ratio and coherence area. It decreases if the speckle size is smaller than the detector due to averaging effects. In the heterodyne method, it actually depends on the root of the mixing efficiency, that is, the degree to which the scattered field and local oscillator have a phase correspondence over an area equal to the coherence area. The efficiency is maximum if local oscillator and scattered field have wave fronts that match in phase. This efficiency becomes small if the wavefronts are tilted or distorted with respect to each other. Temporal and spatial coherence is also important, so the optical path of the "two laser beams" must be the same. The light mixing takes place in fiber. In addition, an optical filter can be used to attenuate the intensity of unscattered light and prevent damage to the detector. The polarizer, on the other hand, is necessary to attenuate the intensity of the scattering light so that the intensity of the local oscillator is much greater than the light scattered by the sample.

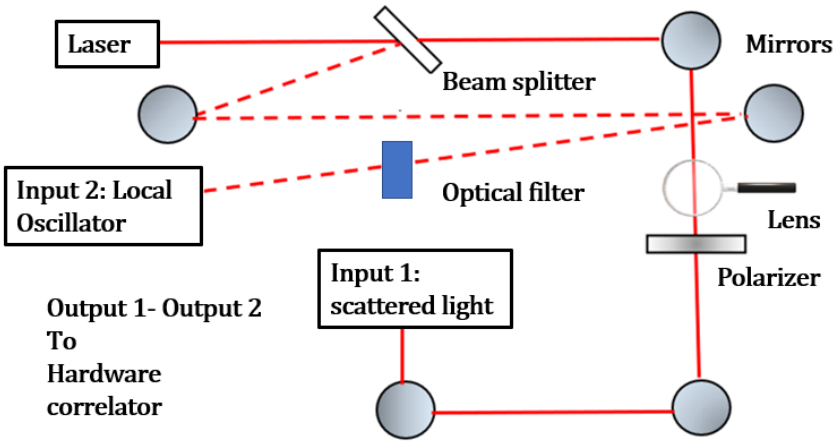

Figure 3.2 Setup for heterodyne configuration: laser radiation hits the beam splitter, thus generating a "second beam" that will be used as a second input (local oscillator). The initial beam continues along the optical path to the sample, passes through the sample and produces diffuse radiation that will be used as the first input (scattered light). The two outputs are collected in fiber. The correlator finally generates the autocorrelation functions of the mixed intensity.

A heterodyne setup was implemented to explore the DWS technique in all its aspects. This setup was then used in the homodyne configuration for the calibration procedures of the microgravity experiment and to validate control measurements in on-ground experiments.

The first colloidal suspension studied is composed of 900 nm polystyrene particles, whose Stokes speed $v_s = \frac{2}{9}\frac{\Delta\rho}{\eta} gr^2$ corresponds to a few nanometers per second. The larger particles diffuse more slowly but have a sedimentation rate that depends on both particle radius and density. The chosen particles do not settle to avoid transit-time effects. In figure 3.3 measures of dynamic light scattering for the correlation function in different configurations are reported. The correlation function in homodyne and heterodyne and the heterodyne configuration with the sample placed in horizontal translation are added. The movement of the sample holder is done by a stepper motor set at various speeds. It is noted that in the heterodyne configuration with the translating sample, there are cosine oscillations in the decay of the correlation function and a shift on the right temporal axis with respect to the homodyne correlation function (figure 3.3). In heterodyne regime the function

$g^2(t) = 1 + \beta g^1(t)$ is directly linked to the correlation of the electric field and only the real part as the product between the transferred moment $\boldsymbol{q}$ and the velocity $\boldsymbol{v}$, vectors of the same scattering plane.

$$g^1(t) = \exp\left(-\frac{t}{\tau_q}\right)\cos\left(\boldsymbol{q}\cdot\boldsymbol{v}t\right) \tag{3.4}$$

All tests are performed also with DWS. In this case, the dispersion of the scattering vectors, due to multiple scattering, does not allow to observe oscillations in the decay of the correlation function. The dynamics underlying the decay are therefore purely diffusive, even in the presence of a uniform motion induced from the outside. The suggestion that a different optical configuration, exploiting the strong limit of heterodyne, could have directly measured the drop velocities to obtain information on the distribution of the size of the drop fails. Even when testing with very large particles, the result only remains the validity of the Siegert relation in the heterodyne configuration.

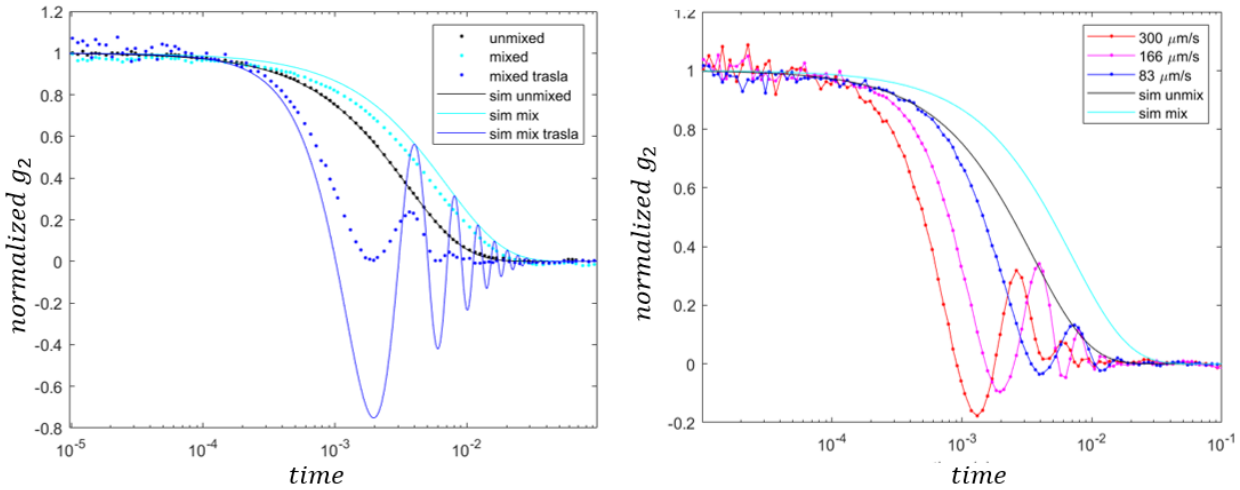

Figure 3.3 The first panel on left, show DLS correlation function in homodyne (unmixed), heterodyne (mixed) and heterodyne configuration with translating sample (mixed trasla) overlap with their simulated curves. On second panel the heterodyne configuration with translation is evaluated for three different translation speed at $300\ \mu m/s, 166\ \mu m/s$ *and* $83\ \mu m/s$.

3.3 Models for dynamics

Diffusing Wave Spectroscopy (DWS) [51,52] is a commonly employed method for studying the structure and dynamics of multiply scattering samples, including emulsions. In DWS, a laser beam emits coherent light that undergoes multiple scattering within the sample before being detected upon exit. The intricate dynamics of isolated drops arise from their translation, degrees of freedom, and thermally excited internal dynamics. To investigate these phenomena, the temporal fluctuations of the luminous intensity resulting from multiple scattering within the sample is analysed. Autocorrelation functions are subsequently computed for the intensity of the scattered light, denoted as $I(t)$. This procedure is typically performed in the homodyne regime $g_2(t) = \frac{\langle I(t_0)I(t_o+t)\rangle}{\langle I^2\rangle}$ where the detected intensity is averaged over initial time t_0 (or over space in case of measurement based on multi-pixel detector, as CCD or CMOS).

To establish a connection between the structure and dynamics of the sample and the temporal fluctuations observed in the patterns, we rely on two fundamental approximations forming the basis of the technical theory.

The analysis assumes that light propagation in the sample occurs through multiple scattering events, where photon's path follows a random walk, experiencing scattering at each step. The significant number of scattering events (high step number of walker) results in the dispersion of light in random directions. The density of diffusing photons (U) is mathematically described by the equation $\frac{\partial U}{\partial t} = D\nabla^2 U$, where $D = cl/3$ represents the reflection coefficient of light, with c being the speed of light and l being the mean free path length between scattering events. Individual scattering events are then approximated by an average scattering event defined by the mean free path of transport l^*.
The measured intensity correlation function $g_2(t)$ is related to the field correlation function $g_1(t)$ by the Siegert relation (eq. 3.2). It is straightforward to conceptualize the electric field at the measurement location as the vector sum of fields originating from all possible optical paths. In this scenario, the relevant parameters are the path length, denoted as s, and the associated statistical weight $P(s)$. For each specific path length, a partial correlation function $g_s^1(t)$ can be defined. Consequently, the correlation function for the electric field $g_1(t)$ can be expressed as the sum of all partial contributions $g_s^1(t)$, each weighted by the corresponding $P(s)$:

$$g_1(t) = \int_{-\infty}^{\infty} P_{l^*}(s) g_s^1(t) ds \tag{3.5}$$

In the case of Brownian motion, $g_1(t)$ has an exponential shape governed by the mean square displacement $\langle \Delta r^2(t) \rangle$ of the scattering centre over time and by the ratio s/l^*, where l^* is the transport mean free path and s is a path length linked to the average number of scattering events.
This parameter l^* is therefore representative of the extent at which the propagation direction becomes randomized and is related to the distance between the scattering centres and the scattering angle $l^* = \frac{l}{\langle 1 - cos\theta \rangle}$

$$g_1(t) = \exp\left(-\frac{1s}{3l^*} k_0^2 \langle \Delta r^2(t) \rangle\right) \tag{3.6}$$

With relevant implicit parameter Brownian relaxation time $\tau_B = D^{-1}k_0^{-2}$ related to the diffusion coefficient D and to $k_0 = 2\pi n/\lambda$, the light wavevector in the medium of refractive index n and with a wavelength λ.

DWS finds an interesting application in rheology by expanding the temporal domain to high frequencies that are typically inaccessible to conventional rheology techniques. By utilizing generalized Stokes-Einstein relations, the mean square displacements $\langle \Delta r^2(t) \rangle$ of the scattering centres can be related, allowing for the determination of creep compliance $J(t)$ and the mechanical viscoelastic moduli [51].

In the absence of externally applied mechanical stress, $J(t)$ is directly proportional to the mean square displacement $J(t) = \pi a / k_B T \langle \Delta r^2(t) \rangle$. The complex mechanical shear modulus $\tilde{G}(\omega)$ is then obtained from the compliance, either through Laplace transforms [56] or by operating in the Fourier domain [57].

$$\tilde{G}(\omega) = G'(\omega) + iG''(\omega) = \frac{1}{i\omega J(\omega)} \tag{3.7}$$

Where $J(\omega)$ is the Fourier transform of $J(t)$, function of the angular frequency, and $G'(\omega)$ and $G''(\omega)$ are respectively the elastic modulus and the loss modulus.
Nevertheless, Kim et al. [58] recently emphasized the importance of considering the impacts of crowding and internal flow within the sample when dealing with concentrated emulsions. In the case of Diffusing Wave Spectroscopy (DWS), where light undergoes multiple scattering events before detection, Wu, Pine, and Weitz

[59] demonstrate that DWS can detect velocity variations within the sample, leading to changes in the relative phase differences in the multiply scattered light. Specifically, they establish that when ballistic motions coexists with Brownian motion, all DWS correlation functions retain the same analytical form as in the classical scenario of pure Brownian motion. However, there is a modification in the time-dependent term, where the linear term is replaced by the sum of a linear term and a quadratic term.
The analysis of emulsion structure and dynamics right after emulsification follows the procedure detailed in ref. [60]. There, the exponential decay of g_1 is modified to consider creaming, by adding, in equation (3.6) an additional relaxation time τ_S. That accounts for the relative motion of oil drops of different size during gravity-induced creaming:

$$\frac{t}{\tau_B} \rightarrow \frac{t}{\tau_B} + \left(\frac{t}{\tau_S}\right)^2 \tag{3.8}$$

Where τ_B is the usual Brownian relaxation time and τ_S is the shear decay time related to the shear rate Γ.
The obtained values for τ_B and τ_S, extracted from the model used to fit DWS correlation functions, encode two types of motion in the sample: Brownian dynamics and heterogeneous ballistic motions. Brownian dynamics, driven by thermal fluctuations, are well understood, with some corrections for dense emulsions to account for drop packing effects [61]. On the other hand, the interpretation derived from the literature [59], which describes the motion of tracers in a viscous flow with defined shear rates, cannot be directly applied here for ballistic heterogeneous dynamics, even though space variation was considered.
In our case, the scattering centres are the drops of an emulsion undergoing creaming or sedimentation, introducing different velocities for individual drops within a static fluid matrix. Following the reasoning in [59] for inhomogeneous velocity gradients, we need to average Γ^2 over the entire probed volume, replacing Γ with $\bar{\Gamma} = \sqrt{\langle\Gamma^2\rangle}$. It is important to note that the mean free path sets the length scale over which $\bar{\Gamma}$ is measured. The dephasing of a photon path that experiences n scattering events, denoted as $\Phi^n(t)$ and defined in equation 1 of [59], is determined by the sum of n terms of the form $\boldsymbol{k_i} \cdot [\boldsymbol{\Delta v_i} t]$. Here, $\boldsymbol{\Delta v_i}$ represents the velocity difference between the i+1 and i scattering centres, and $\boldsymbol{k_i}$ is the wavevector associated with the i-th scattering event. The temporal evolution of these dephasing terms, after appropriate averaging and weighting by path lengths, governs the decay of the heterodyne correlation function. Therefore, it is natural to introduce the root mean square value of the difference in creaming velocities as $\bar{v} = \sqrt{\langle(\Delta v)^2\rangle}$ and identify it with $v = \bar{\Gamma} \cdot l^*$.
The density difference $\Delta\rho$ between the drops and the continuous phase determines gravity-driven drifting, i.e. creaming or sedimentation of drops. The drift velocity v is given by the balance of the shear stresses at the drop boundary [6]. At first approximation, neglecting hydrodynamic correlations and interfacial effects, this velocity is given by the well-known Hadamard-Rybczynski formula:

$$v_{HR} = \frac{2}{9}\frac{\Delta\rho}{\eta} g r^2 \frac{\eta + \eta'}{2\eta + 3\eta'} \tag{3.9}$$

Where R is the drop radius, η' and η are the viscosities of the drop and of the continuous phase respectively and g is the gravity acceleration.

In ref. [60] it is shown that τ_s is related to the variance σ_v^2 of the distribution of ballistic velocities of drops during creaming $\sigma_v^2 = 15(\tau_s k_0)^{-2}$ which is related in turn to the 2.nd and 4.th moments of the drop size distribution via Hadamard-Rybczynski relation

$$\sigma_v^2 \stackrel{\text{def}}{=} \langle v^2\rangle - \langle v\rangle^2 = \left(\frac{2}{9}\frac{\Delta\rho}{\eta} g \frac{\eta + \eta'}{2\eta + 3\eta'}\right)^2 [\langle R^4\rangle - \langle R^2\rangle^2] \tag{3.10}$$

The practical result is that both the width and the average value of the drop size distribution contribute to the variance of creaming velocities.

It is crucial to highlight the significance of quantifying the difference in drop velocities in emulsions for two main reasons. Firstly, this parameter directly influences the likelihood of drop-drop collisions during the creaming process, which is a fundamental factor for coalescence events. This holds particular importance for less-stable emulsions where coalescence events occur on a similar timescale as creaming. In such cases, there may be a cross-correlation effect, wherein coalesced drops rise much faster, leading to a chain of subsequent events.
Furthermore, even in more stable emulsions where coalescence is not as rapid, the spread of the velocity distribution is associated with the drop size distribution $f(R)$ (eq. (3.10)). This is because the velocity of each drop is connected to its size, viscosity and a lesser extent, its coverage by surfactants [62–64].
Therefore, characterizing the dynamics of emulsions during the early stages of creaming yields information on the size distribution of drops beyond the standard DWS characterization of the average drop size through the measurement of l^*. Moreover, the light diffusion process is governed by the transport length l^* and numerical simulations [65] allow to relate l^* to the drop size, being governed by the refractive index mismatch between dispersed and continuous phases.
Specifically, the analysis techniques to be presented in the subsequent chapters offer a means to model the outcomes of Diffusing Wave Spectroscopy (DWS) and enable the investigation of emulsions under microgravity conditions. These methods facilitate the acquisition of dynamic, morphological, and structural information about the emulsions.

3.4 Optical Monte Carlo methods

In a typical laboratory DWS setup, detectors are placed in forward (or transmission) configuration, collecting light that has crossed the whole sample cell, and in backscattering configuration, collecting light emerging from the side illuminated by the laser beam. The sample cell and scattering geometry can be adapted to adhere as much as possible to a configuration that allows for analytical calculation of $P(s, l^*)$: slab sample of size much larger than the transport mean free path l^*, irradiated by an infinite plane wave [66]. In foams and emulsions, the destabilization processes that drives ageing typically leads to broader bubble/drop size distributions, and consequently to an increase of l^* [67]. At later stages of ageing, therefore, the assumptions used to build analytical $P(s, l^*)$ expressions would inevitably fail.
An experimental determination of $P(s, l^*)$ is possible by measuring the broadening of a narrow laser pulse crossing the turbid sample; however, this require a pulsed-DWS setup with dedicated hardware capable of sub-nanosecond resolution [51]. The numerical determination of $P(s, l^*)$ provide a more flexible approach; by using a realistic Monte Carlo simulation random diffusion of photons propagating in the volume of the sample before reaching a detector, $P(s, l^*)$ are modelled and then used to analyse experimental correlation functions obtained in any scattering geometry, even when specialized sample cells are employed [60].

While the classical analysis for DWS is based on analytical forms for P(s), which are only valid for idealized geometries [51], we recently shown that in realistic conditions this assumption might lead to drastically unreliable estimates for the time-dependent mean square displacement [60]. This can lead to incorrect assumptions regarding models of droplets. Therefore, the experimental correlation functions must be adapted using the explicitly calculated path length distribution function, which can be generated via Monte Carlo simulations in real geometry.

Simulations were performed in MATLAB processing environment; a detailed description of the simulation algorithm is given in ref. [60], the code is freely available in GitHub [68], and it is briefly summarized in the following. The code simulates in parallel the random diffusion of a bunch of photons within the sample, contained in a rectangular cuvette of known sizes. A value of l^* is chosen. The photons originate at a depth l^*

within the sample, on a point on the YZ plane chosen randomly according to a specified beam geometry; typically, either a gaussian beam of specified width, or a uniform plane. Then, the photons propagate with steps whose direction is randomly distributed along a sphere, and whose length follows a log-normal distribution of average value l^*, following assumptions first taken by Durian et al [69]. After each step, the position of each photon is checked. A photon is detected when it reaches the position corresponding to the collection optics of a given detector; after a specified number of simulated photons is reached, the software calculates the distribution of path length $P(s, l^*)$ for the given value of l^* of all photons detected by all specified detectors.

To model the experimental correlation functions, a set of $P(s, l^*)$ for each detector is generated over a range of l^* typically up to several mm, with step-size down to 10 microns. These weights on the path are used to simulate the corresponding correlation functions by trapezoidal integration of eq. (3.5).

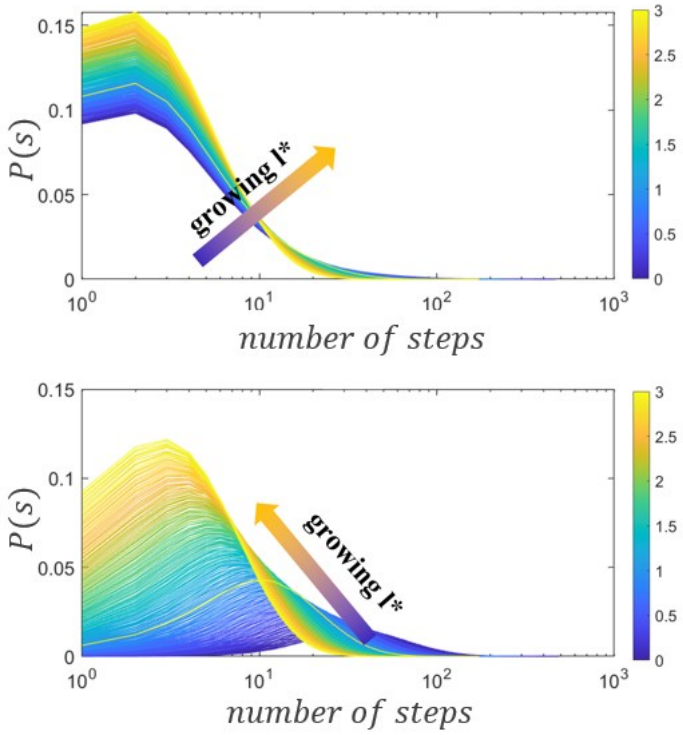

Figure 3.4 Example of distributions of path length s,$P(s, l^*)$, generated. Top panel: Backscattering detector; Bottom panel: Transmission detector. The colour indicates the value of l^* (from 100 micron up to 3mm) corresponding to each curve (from blue to yellow)

In this context, l^* plays a crucial role in quantifying the difference between the decays observed in Backscattering and Transmission. Once both decays are accurately determined through experiments, l^* is disentangled from the characteristic times τ_B and τ_S, as well as from baseline and contrasts during the fitting process. This decoupling enables a robust fitting procedure, wherein the best least squares fit is performed for each l^* value, and subsequently, the fit with the lowest value of the reduced χ^2 is chosen as the best fit.

$$\chi^2 = \sum_{FW,BS} \frac{1}{N-P} \sum_{t_i} \left(\frac{g^{(2)}_{exp}(t_i) - g^{(2)}_{theo}(t_i)}{\sigma(t_i)} \right)^2 \tag{3.11}$$

Where χ^2 is defined as in eq. (3.11) as the deviation between the experimental and theoretical correlation function $g^{(2)}_{exp}(t_i)$ and $g^{(2)}_{theo}(t_i)$. The $\sigma(t_i)$ is the corresponding uncertainty, P are the number of free parameters, and the sum is extended to the N values of times t_i.
In other words, this fitting routine minimizing the reduced χ^2 for a set of data acquired by two detectors can obtain the best fitting parameters: the relaxation time of the dominant dynamical regime (either Brownian motion or creaming) and l^*. This strategy solves the problem of minimizing different variables, decoupling fitting parameters.

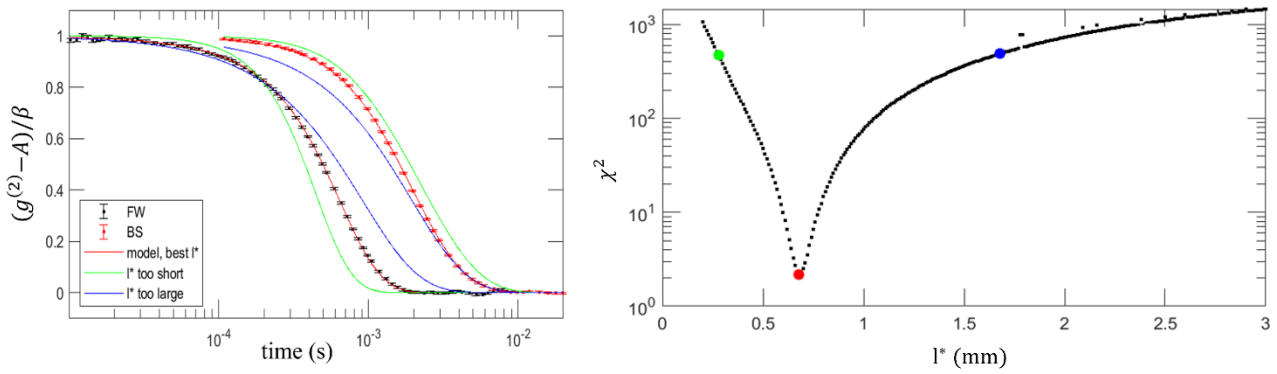

Figure 3.5 Left panel: reduced χ^2 of the fits for each value of l^*, the red point indicates the minimum value χ^2. Right panel: red lines are the best fits to the measured correlation functions, in green and blue are "wrong" fits: the model curves for BS and FW are either too far apart (l^* too short) or too close to each other (l^* too large).

4. The microgravity experiment platform “Soft Matter Dynamics”

In this section, an overview will be provided of the experiment container with light diffusion and image diagnostics for Soft Matter Dynamics (SMD) experiments conducted on board the ISS. The measuring capacity can be used to study different materials in interchangeable samples cellular units (SCU), indeed samples in independent SCU can be easily replaced to allow experiments with new materials. Optical and light diffusion diagnostics are crucial for soft matter studies, so the dynamics in opaque samples can be probed with scattering light. The experiment container with optical diffusion diagnostics is described in the following section. The story of this Soft Matter Dynamics dates to the late 1990s and is based on the "Foam Optical and Mechanical Project" financed by National Aeronautics and Space Administration (NASA) since 1992 for rheology studies on foams. After several proposals and experiments on foams, in 2014, the project was re-launched when ESA decided to include previously separate projects on granular media and emulsions.

The Fluid Science Laboratory (FSL) is a research facility located on the Columbus Orbital Facility. It is specifically designed for multi-user experiments focused on the investigation of fluid physics in the unique environment of microgravity. For this purpose, it can be operated automatically on station by the flight crew or remotely controlled from the ground in the so-called tele-science mode. The FSL modular design consists of a Master Control Unit to manage the communication between ground and facility and a Video Management Unit capturing and processing and store all video data. In addition, a Power Control Unit, a Thermal Environment Control System, and the Central Experiment Module provides the power supply, water cooling, and data connection. The SMD Experiment Container (EC) is a microgravity experiment container that can be placed inside the FSL.

Soft Matter Dynamics EC is an optically closed container (figure 4.1), meaning that all required diagnostic systems are integrated into the experiment container itself. It is designed to perform simultaneous DWS and imaging experiments on emulsions, foams, and granular materials in microgravity aboard the International Space Station. The instrumentation was built by Airbus D&S, along with two other replicas that will be used for the experiment described in this thesis. A laboratory replica known as the Elegant Breadboard (EBB), developed mainly for experiments on-ground and during parabolic flights, and an exact replica of the instrument currently aboard the ISS known as the Engineering Model (EM), used for validation of the on-flight experimental procedures.

4.1 Sample cell carrier

The main component of SMD consist of an experiment container of size $40x28x27\ cm^3$, containing the DWS optical diagnostic hardware and a sample cell carrier, i.e., a rotating tray driven by a stepper motor. Five sample cell units (SCU) can be accommodated simultaneously on the tray. The experiment container is mounted into a drawer, attached to the rest of the FSL rack that provides the power supply. Furthermore, accelerometers are attached to the drawer to continuously monitor the level of microgravity. The FSL microgravity measurement assembly is positioned in proximity to the experimental container to capture residual acceleration in all three axes. The micro-accelerometer has a sampling frequency of up to 1500 Hz. To filter the output signal from the micro-accelerometers, a decimating filter is employed.

FSL also furnishes a water-cooling circuit, connected to an isothermal housing where the sample cell holder is located. This ensures a constant target temperature for the sample cells and compensates for temperature changes due, for example, to the heat produced by the electronics or the emulsification process. The

temperature is measured by three sensors located between the cell and the inside of the SCU and is kept constant at about 20 °C.

Sample cell support facilitates remote control of the sample at the measurement position and exchange in orbit of the SCU. Each SCU can accommodate four sample cells. The tray can be rotated so that one of the SCU sample cells can be moved to the measuring position, where it can be accessed through optical diagnostics.

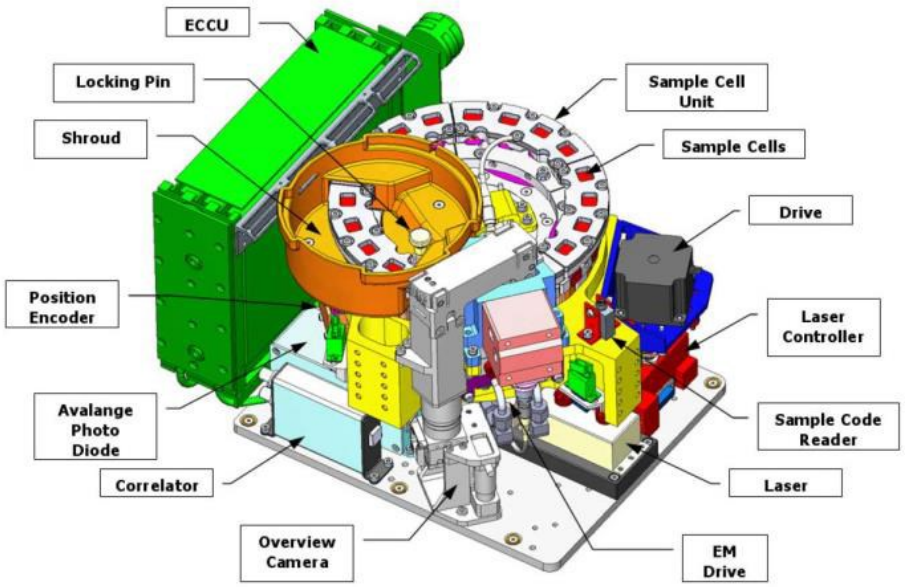

Figure 4.1 Interior of the SMD container. The main components are the experiment container controller unit, the sample cells (SC) in the sample cell units (SCU) and the stepper motor to drive the carousel with the sample cell units. The diagnostics consist of a laser, overview camera, line camera and avalanche photodiodes with a hardware-implemented intensity correlator (figure adapted from P. Born et al., Soft matter dynamics: A versatile microgravity platform to study dynamics in soft matter, Rev. Sci. Instrum. 92 (2021). doi:10.1063/5.0062946)

4.2 Optical diagnostics

The on-board analysis is mainly by Diffusing Wave Spectroscopy, complemented by a time-resolved multi-speckle line camera analysis applied to the backscattered light. In fact, the SMD is equipped with a multipixel detector in backscattering geometry and two APD-based detectors in Transmission and Backscattering geometry. The synergy of these two types of techniques allows us to explore not only the dynamics and structure of emulsions during the aging process, but also the characteristics of transient and intermittent events due to coalescence processes between drops. An Overview Camera is also used for monitoring/controlling the experiment.

- The Overview Camera (OVC) is employed to visually examine the progress of the experiment. Moreover, this camera allows us to investigate the sample also with optical microscopy techniques. To achieve the necessary high resolution and small pixel size for capturing detailed images of the target, a microscope has been specifically engineered as the optical component of the Overview Camera (high resolution camera type Point Grey P/N FL3-GE-50S5M-C), this is a monochrome camera with a CCD sensor giving 2448x2048 pixels of 3.45µm size. The camera is focusable on the

target via a modified motorized linear scan stage with high displacement resolution (focal plane sweep through the sample above 15 mm with 100 step/mm resolution). The full field of view (FOV) of the microscope is 14.4 x 12.2 mm^2 which can be recorded at a rate of 8 fps. High power LEDs emitting blue light are utilized as an incoherent light source for the overview diagnostic. These LEDs are positioned around the target area.

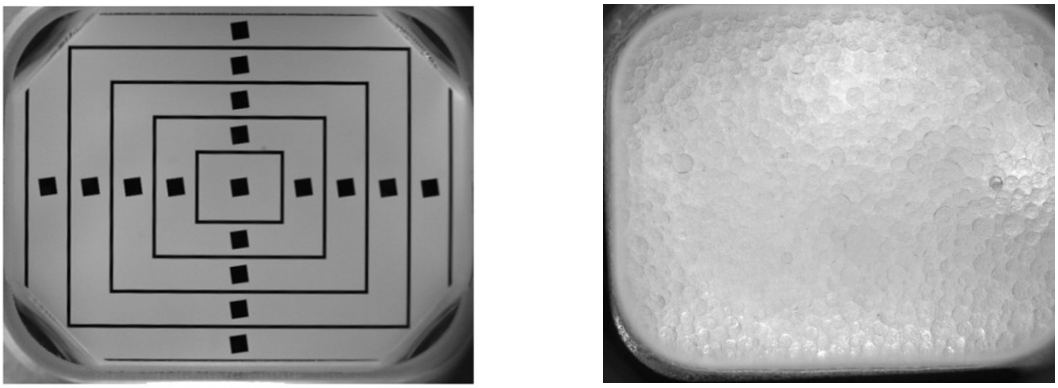

Figure 4.2 On the left calibration images from the OVC. On right examples images of an emulsion acquired with OVC.

- A multi speckle analysis through the line camera (LC) allows instead to investigate the dynamics of the drops resolved over time, through the dance of the speckles produced by the light thrown by the sample. The raw output from a high-speed line camera (Basler Racer, raL2048-48gm, 2048 pixel, 8bit) is a spatio-temporal speckle image, which is essentially a composition of multiple line images, typically ranging from 1024 to 2048 pixels per line and up to approximately 10000 lines in total. Each line image is captured at a specific timestamp determined by the specified line rate. By employing an algorithm outlined in the multi-Speckle analysis section, Time Resolved Correlation curves can be computed based on the raw spatio-temporal speckle image.

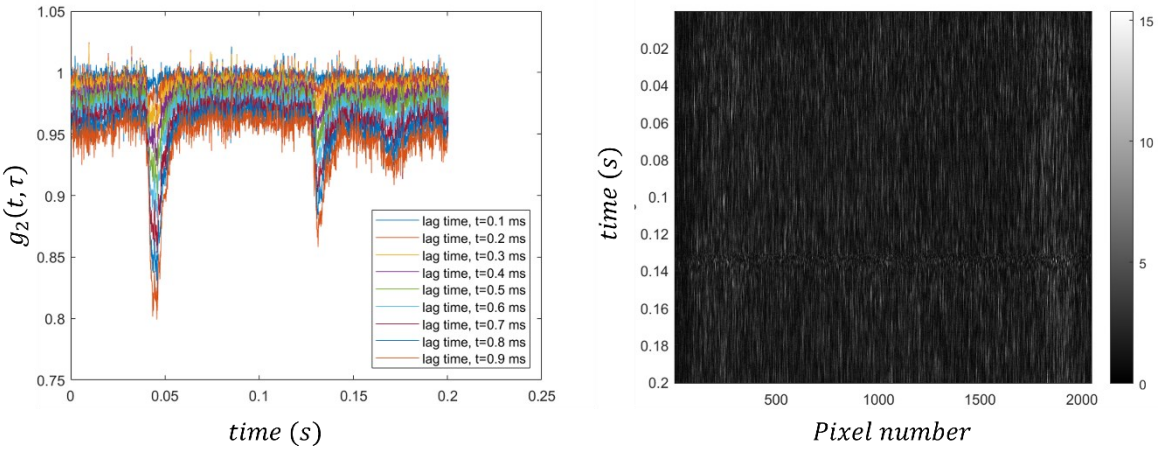

Figure 4.3 On the left Time Resolved intensity autocorrelation: each line corresponds to a specific delay time (ms). On right raw spatio-temporal speckles images.

- Corrtector/Avalanche Photo Diode (APD) module allows the acquisition of the functions of autocorrelation of the intensity of light that passes through the sample.

The APD-based detectors are 4-quadrants APDs “Corrtector” modules equipped with cross-correlation hardware (ALV, equivalent to an ALV-7004/USB correlator), capable of acquiring correlation functions with a minimum delay of 12.5 ns, which is the time required for calculating the correlation. In each scattering direction, namely backscattering or transmission, four avalanche photodiodes receive illumination (as shown in figure 4.4). The signals from these photodiodes are then directed to the input channels of the hardware-based intensity correlator. This correlator allows for remote selection to compute either the autocorrelation or cross-correlation of the input intensity traces. The autocorrelation is the measurement of correlation between a photon count trace and a delayed version of itself, with the correlation value varying based on the delay time. It provides information about the similarity between observations at different time lags. A correlation value of 1 signifies no change and indicates identical signals, whereas a correlation value of 0 suggests that the two signals are different from each other (figure 4.4). Finally, the monitoring and correlation channels of the hardware correlator, along with the intensity traces, are read out and stored.

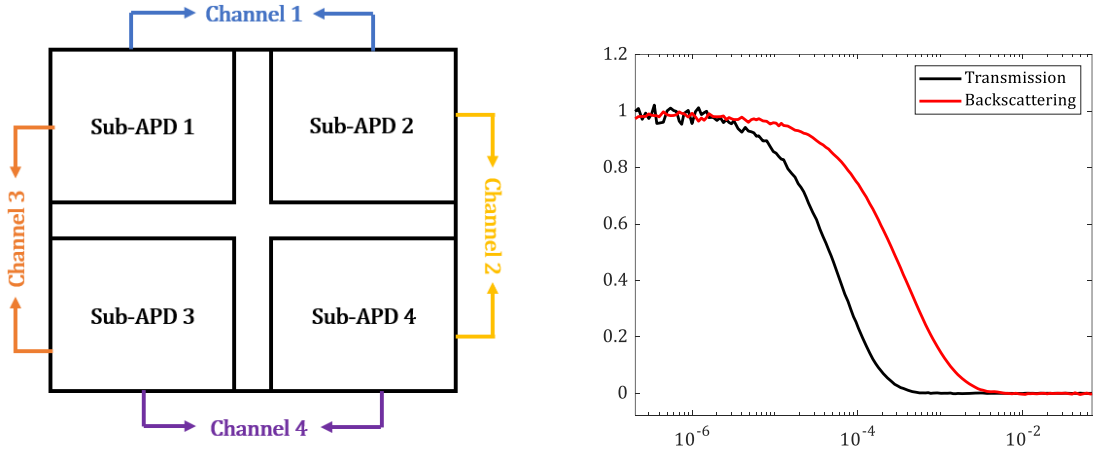

Figure 4.4 On left APD layout. An APD consists of 4 sub-APDs, resulting in four photon count channels. On right two typical DWS correlation functions for light collected respectively in backscattering (red line) and in transmission (black line). The characteristic time and the details of the shapes of the two decays reflect the propagation of light in the sample and the intrinsic dynamics of the scattering centres.

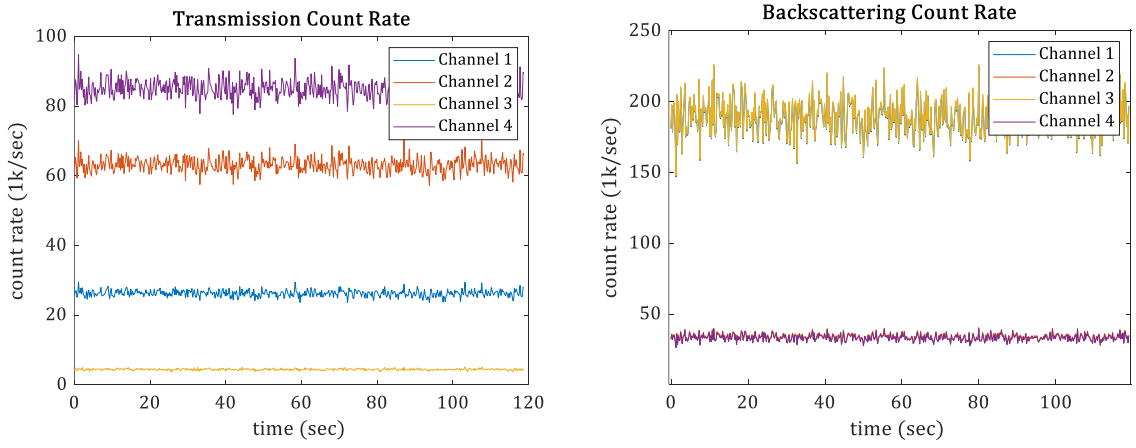

Figure 4.5 Examples of photon count traces for both Transmission and Backscattering geometry.

- Coherent Laser light is provided by a diode-pumped laser (Cobolt AB, DPL 532) with λ=532 nm and illumination power of 200 mW. Illumination is performed by single-mode polarization maintaining fiber, and a collimator is used. Line camera light collection is performed by a multimode fiber equipped with a collimator used to illuminate a 2.1 mm spot on the sample surface. The collection of light for APD detection is done by a non-polarizing single mode fiber. Polarizers are used to ensure that only multiply scattered laser light is collimated into the fiber.

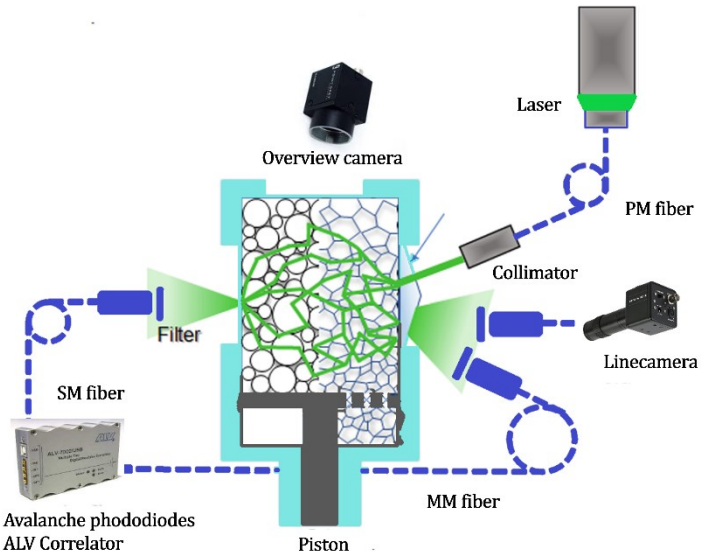

Figure 4.6 The optical diagnostics of the soft matter dynamics experiment container are presented in a schematic representation. At the centre of the setup is a sample cell, and multiple sample cells (up to four) are arranged as a unit on a carousel, as shown in Figure 3.12. By rotating the carousel, one sample cell at a time can be brought into the measurement position, enabling access for diagnostics. The sample cell unit consists of a body made of cyclic olefin copolymer (COC) and features a three-faceted prismatic interface for both the illuminating light and the light backscattered from the sample. Two collimators, positioned perpendicular to their respective facets, collect the backscattered light for the line camera (LC) and the avalanche photodiodes (BS). In the transmission direction, the collimator collects the light transmitted (FW) through the flat cell wall and directs it towards the photodiodes (APDs). The overview camera (OVC), equipped with a microscope objective, captures images of the sample from the top surface of the sample cell. To illuminate the sample, three light emitting diodes (LEDs) are employed. Additionally, a piston mechanism can be utilized for emulsifying the samples (figure adapted from P. Born et al., Soft matter dynamics: A versatile microgravity platform to study dynamics in soft matter, Rev. Sci. Instrum. 92 (2021). doi:10.1063/5.0062946).

4.3 Sample cell and Emulsification procedure

The experimental sample cell units consist of four sample cells that are hermetically sealed. Each sample cell is equipped with a magnetic piston, which can be magnetically activated to generate emulsion. The piston undergoes oscillatory motion within the lower region of the cell) [70]. For emulsion preparation, the sample is placed in a sample cell. This is made of cyclic olefin copolymer (COC), a plastic material that exhibits reduced permeability to aqueous solutions, and the probed sample volume occupies the upper part of the cell. The

piston, connected to a permanent magnet, is actuated by the time-dependent magnetic field generated by a couple of coils in which current is injected with square waves of constant frequency, for a chosen duration. Emulsification is performed by moving the sample cell piston at 18 Hz, for 4 cycles of duration 2 minutes each, with 1-minute pauses that separate the cycles. This procedure reliably generates the same emulsions, even when a previously aged emulsion is re-emulsified; this has been evaluated by verifying that the resulting DWS correlation functions measured by all detectors immediately after emulsification are reproducibly the same.

The upper part of the sample cell is specifically designated for measurements, with dimensions of 11.25 mm in the beam direction and 14.25 mm and 14.5 mm in the perpendicular directions. Refer to figures 4.7-4.8 for a visual representation of the sample cell. The emulsion, in direct contact with the top cover of the sample cell, can be examined using the overview camera. Laser light transmission and backscattering utilize the designated front optical interface and back optical interface.

On the front side of the cuvette, both illumination and light collection for BS-geometry detectors are accommodated in a small space. The sample cell front optical interface consists of a pyramid with three facets, with an angle of 25° with respect to the sample surface, and an angle of 33° with respect to each other (figure 4.8). A semi-focalized beam impinges on the sample ('spot-in' illumination), is scattered within the sample, and is collected from a location close to the illumination point ('spot-out' detection). For some technical issues, the DWS backscattering APD fiber collects light from a circular spot (beam diameter 0.7 mm) which is displaced by a small but a priori undetermined distance from the spot of the impinging laser radiation, which has a gaussian profile with $1/e^2$ diameter of 2.1 mm. The accurate knowledge of the distance travelled by light gauges determines the DWS determination of l^*, the light transport length, from which the mean drop radius is determined by DWS. Therefore, it is important to determine this distance accurately: for each of the two BS detectors, line camera and APD, we need to characterize accurately the distance d_{in-out} between "spot-in" and "spot-out" points (chapter 5.3).

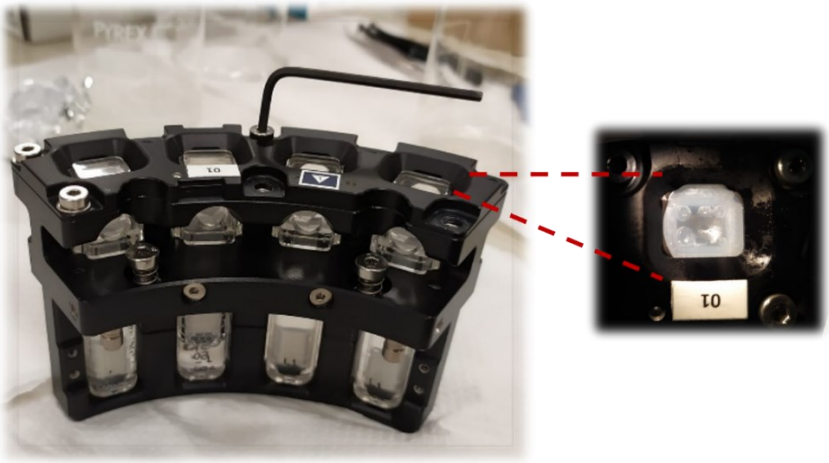

Figure 4.7 The sample container with four sample cells, each of which houses at the bottom the piston shaft, which ensures the emulsification process. At the top two optical interfaces (one on front and one on back) for laser diagnostics, while on the cell lid, a window, allows microscopy and imaging measurements.

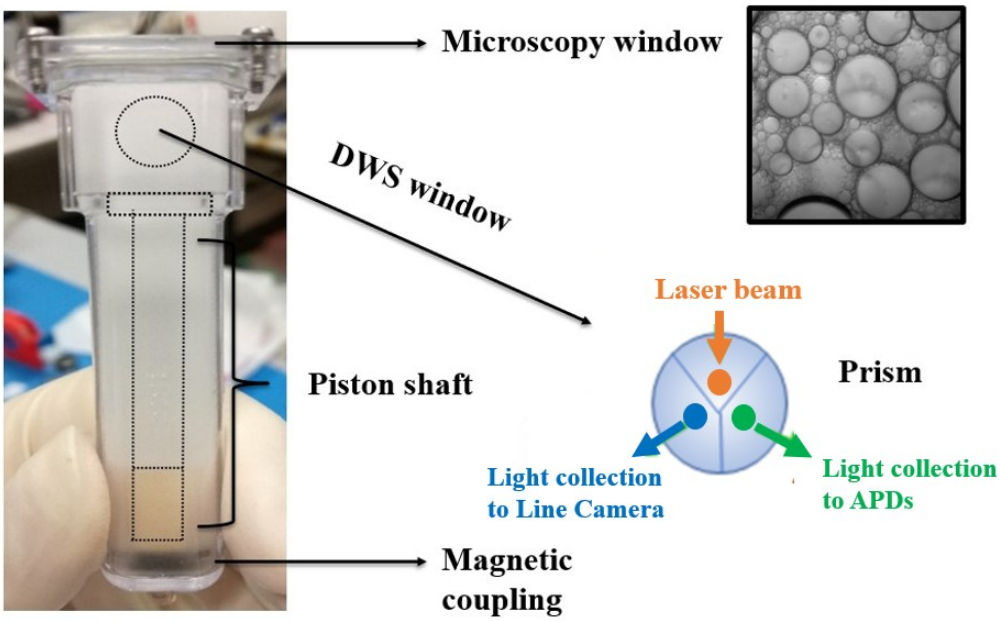

Figure 4.8 Here is a picture of the sample cell (SC). The upper part of the cell is used as a microscope window. The central part contains the sampled emulsion volume with the prism used to accommodate simultaneous lighting and light collection with APD and line camera. The Gaussian beam impinges one side of the pyramidal prism (spot-in lighting, orange point); the backscattered light is collected by several detectors from two different points, (spot-out collection, green and blue point) placed at a distance d_{in-out} *from the lighting point.*

5. Activities propaedeutic to the microgravity experiments

5.1 Preparation on ground: Elegant Bread Board

In preparation for microgravity experiment in orbit, the EBB (Elegant Bread Board) is utilized in University of Parma to conduct ground-based studies on the samples intended for the experiment. This allowed for a comparison of experimental data between the ground and the onboard conditions. Additionally, standard calibration is conducted on the ground. Subsequently, a second preparation and control experiment is conducted at the Belgian User Support and Operations Centre (BUSOC), involving the participation of a scientists' team from the University of Parma. At this stage, the science team from Parma provides continuous feedback to the operators at the BUSOC, enabling them to make necessary modifications and optimize certain measurement parameters before the EM is transported to the ISS.

As already mentioned in chapter 4, the EBB, developed mainly for ground experiments, is a prototype of the equipment on board with slight differences compared to EM in terms of diagnostic optics. EBB uses a 1024 pixels line camera (Basler, ruL1024-19gm, 1024pixel, 8bit), and two single-APD modules. Correlation functions for the APDs are calculated by an ALV-7004/USB correlator; since single APDs with no cross-correlation are used, the minimum accessible lag-time is $1\mu s$.

Before starting with the data analysis following the procedure outlined in chapter 3.4, it is important to determine certain vital parameters to accurately simulate P(s). Specifically, it is necessary to establish two detection areas, one for BS and one for FW. Additionally, the initial positions for each photon need to be generated within the sample at a depth of l^*. These positions can be generated using either uniform side distributions or Gaussian distributions, considering the two potential beam profiles.

The OVC enable the visualization of the Gaussian profile of the xy plane beam, allowing the determination of the sigma beam by conducting a Gaussian fit of the beam intensities profile. Then is employed to characterize the incident laser beam and the outcomes align with the specifications outlined in the optical design report provided by Airbus D&S.

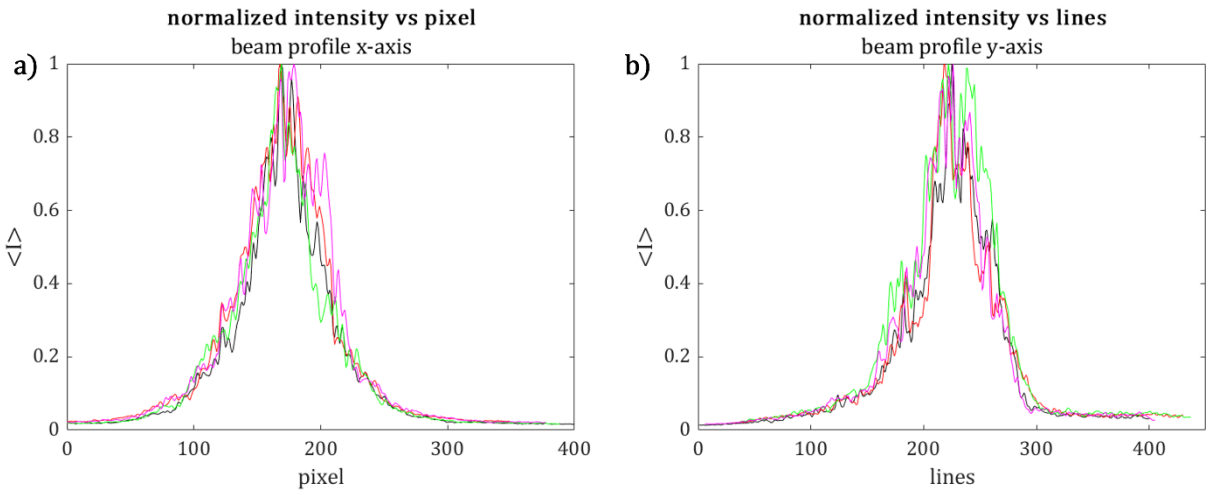

Figure 5.1 Beam profile along x-axis (panel a)) and y-axis (panel b)). The mean normalized intensity is here shown as a function of the pixel and lines.

One issue worth noting is the challenge posed by thermal expansion. Specifically, during the launch phase, the SMD cell experiences an overpressure due to the thermal expansion of the liquids it contains. Consequently, the samples undergo a significant and rapid pressure change, which can damage both the sample and the

cuvette housing it. As a result, many experiments conducted on the ground have focused on bubbly emulsions, characterized by a volumetric fraction of air within them. Therefore, for this investigation, it becomes essential to introduce a certain percentage of air into the samples and understand its impact on the dynamics and aging of the emulsion, in view of the forthcoming experiment on board.

Let's consider an initial volume of the cell at the absolute temperature T_0, which is filled with initial volumes of water, oil, and gas $V_0^{cell} = V_0^{wat} + V_0^{oil} + V_0^{gas}$. A temperature variation results in the expansion/contraction of these volumes and a variation of the pressure in the cell.

This condition is consequent to the assumed physical constraint that the final volume of the cell must be equal to the sum of the volumes of the liquids and gas after the expansion. Violation of such condition means that the variation of the cell and liquids volume cannot be compensated by the variation of the bubble volume.

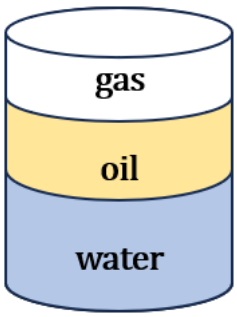

Figure 5.2 Diagram of a cell in which the fraction of oil, water and air is displayed. It is necessary to insert a percentage of air inside the water/oil sample to bypass the effect of overpressure in the SMD cell, due to the thermal expansion of liquids.

To comply with the overpressure limits, PASTA SC must be filled, leaving an air volume of 2-3-4% (exact value depends on oil fraction). Firstly, its effect on DWS is estimated theoretically. Then some DWS experiments are conducted in Parma on EBB to check our simulations.

In case of two components mixtures (A and B) in a continuous medium, such would be the case for oil drops and air bubbles in water, a reasonable approximation commonly found in the literature [71] is to have an effective transport length l^* given by the relation:

$$\frac{1}{l^*} = \frac{1}{l_A^*} + \frac{1}{l_B^*} \tag{5.1}$$

The transport length, denoted as $l^*_{A\ or\ B}$, represents the distance travelled by the hypothetical dispersion of component A (or B) alone in water. In this approximation, the dynamics probed by DWS are primarily influenced by the component with the shorter transport length. It is worth noting that $l^*_{A\ or\ B}$ is linked to the volume fraction of component A (or B), the corresponding size distribution, and the scattering power, which is also dependent on the refractive index mismatch.

Moreover, l^* is directly proportional to the scattering mean free path, denoted as l, which is connected to the scattering cross section σ and the density of the scattering centers ρ through the relationship $l = 1/\rho\sigma$. Additionally, it is important to highlight that the mean free path of transport is larger than l by a factor resulting from anisotropic scattering, particularly for large scattering centres.

By employing a computational code utilizing the Mie calculator [72], it is possible to simulate the trends of the average free path resulting from air bubbles and oil drops. This simulation assumes a dispersion of oil with

a refractive index of $m = 1.45$ (MCT oil) and considers air bubbles of equal size with a refractive index of $m = 1$.

Examining 50:50 oil in water emulsions as one of the samples under consideration, it is observed from the provided figure that when the air content reaches 4%, the transport length (l^*) due to air surpasses the l^* due to oil by a factor of at least two. By further investigation, it can be demonstrated that increasing the air content in the same emulsion or reducing the oil content leads to comparable values of l^* for both air and oil, regardless of the drop size. This indicates the increasing significance of air bubble dynamics in these scenarios.

However, it is reasonable to disregard the influence of air bubble dynamics and focus primarily on the dynamics of oil drops when studying emulsions with low air percentages and high oil contents using DWS probes. As can be seen from figure 5.3, the value of l^*_{air} due to air bubbles is much larger than l^*_{MCT} due to oil drops, making the effect of air bubbles on drop dynamics negligible.

However, it is important to note that these assumptions may not hold true if the air bubbles adhere to the walls of the sample cell instead of being uniformly distributed throughout the sample volume.

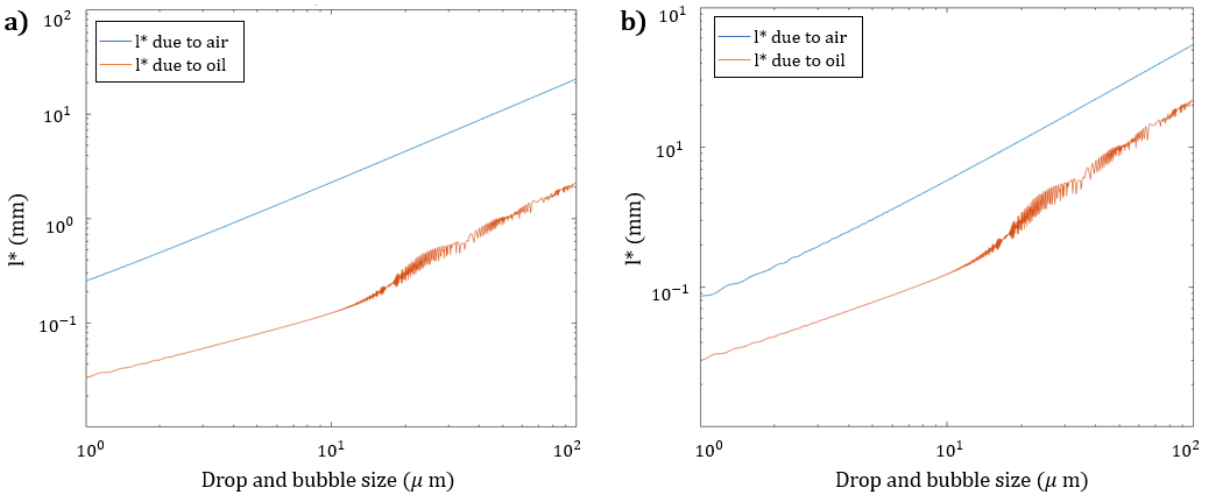

Figure 5.3 Transport mean free path l^* of oil in water (50:50) bubbly emulsion with 4% of air content. In panel a) air bubbles and oil drops have the same size, while in panel b) air bubbles are 4 times larger than oil drops because of the different surface tension of MCT/water and air/water at the given surfactant concentration.

Furthermore, in relation to the established standard PS, the impact becomes apparent when observing the simulations of the actual l^* (refer to figure 5.4). As we examine the effects of both air bubbles and 900 nm polystyrene nanoparticles on l^*, it becomes evident that the presence of air bubbles larger than 100 microns significantly alters the suspension's l^* value. Such alterations have the potential to influence the Brownian relaxation time and subsequently affect the diffusion coefficient. Consequently, an "effective diffusion" phenomenon arises that fails to discriminate between the dynamics of air bubbles and oil droplets. Certainly, this phenomenon is not observed under gravity since air bubbles experience faster creaming compared to oil droplets.

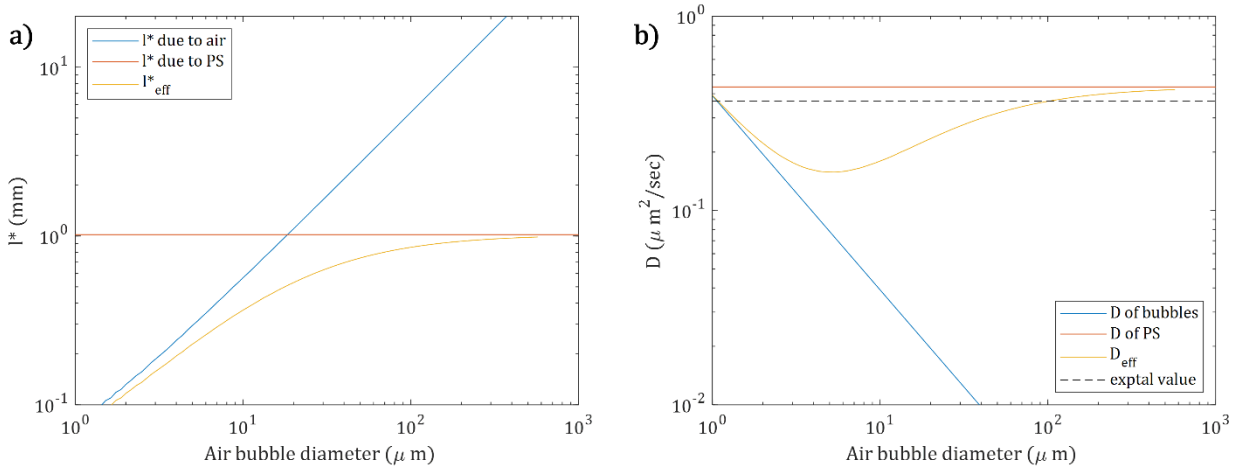

Figure 5.4 a) Mie simulation of the mean free path of transport l^* due to air bubbles, polystyrene nanoparticles (PS 900 nm) and ${l^*_{eff}}^{-1} = (l^*_{PS} + l^*_{air})^{-1}$. Up to 100 microns size of air bubbles both l^* values become comparable. This could result in an effective Diffusion coefficient (panel b)) which has a lower value than expected for the suspension of nanoparticles.

The preparation of samples involves several steps. Firstly, a solution of water or oil and the desired concentration of surfactant is prepared, considering the solubility limit. In this study, a solution of C12EO21 dissolved in H_2O with a molar concentration of $10^{-4}\ M$ and $2 \cdot 10^{-4}\ M$ was used. The samples selected for this study have a higher oil content (50:50 oil/water ratio) to ensure greater stability under gravity.

The cleaning process follows the standard procedure commonly used for plastic objects in the laboratory. During this process, the cells are emptied and washed with a neutral detergent while being heated in an ultrasonic bath at a temperature of 35 degrees Celsius for 30 minutes, following the guidelines provided by Airbus. Subsequently, the cells are subjected to thorough rinsing multiple times using generous quantities of ultrapure water and isopropanol.

Upon the completion of the cleaning and disassembly of SCs and SCU, the empty and filled volumes were determined according to the provided procedure. The obtained filled volume measures around 3.5 ml. It is worth noting that there is a 2% variation in the filled volume among the different SCs. Moreover, the probed volume is observed to be 1.7 ml.

The sealing phase of the cell is extremely delicate, as it is crucial to avoid trapping any air inside. While the nominal concentration is 0% air, precautions are taken to minimize the amount of air present. For subsequent measurements, specific percentages of known air volumes are introduced. The specially designed lid by our collaborator Professor James Ferri and Doctor Robert McMillin from VCU (Virginia Commonwealth University) for this experiment features a perforable membrane, which allows for the extraction of an emulsified liquid volume equal to the desired amount of air to be inserted into a 0% air emulsion.

The measurements are performed automatically once all the parameters are configured using the software provided on the EBB. In this research, measurements are conducted over an hour, with particular emphasis on the initial 10 minutes. The most interesting dynamics of bubbly emulsion under gravitational conditions occur during the initial stages of emulsion formation when the sample is subject to creaming.

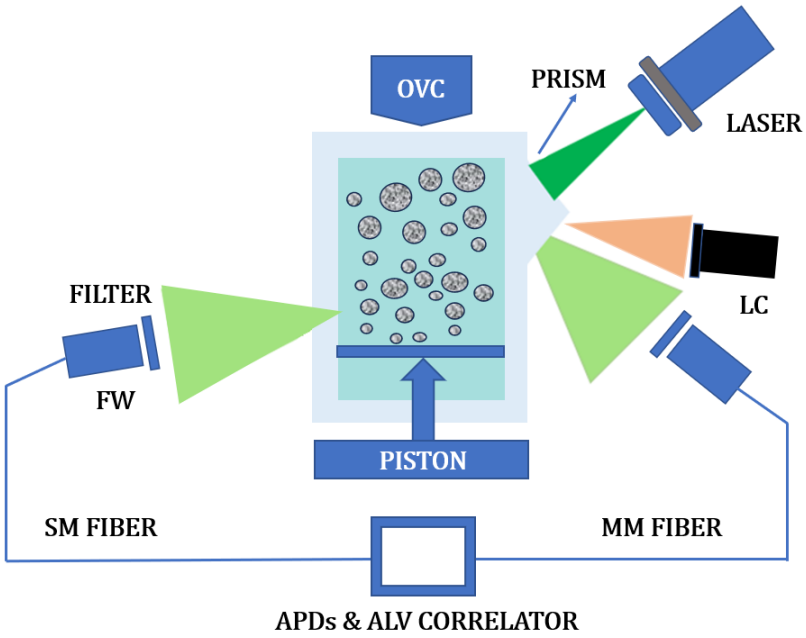

Figure 5.5: Schematic of the EBB, as a prototype of the equipment on board. The laser light is collided and impinges on the prism and then passes through the sample. The detection takes place in both geometries (BS and FW) thanks to photomultipliers that are connected to the correlator and then to the software. Complete the optical analysis OVC and LC.

Correlation functions in both BS (backscattering) and FW (forward scattering) configurations yield essential dynamic parameters. These studies employ the same fitting routine described in earlier chapters, utilizing Monte Carlo simulation to generate various probability distribution functions of the path length of photons $P(s)$ within the cell. This approach proves to be more robust compared to treating the path length l^* as a continuously changing fit parameter and gives us the dynamical parameters τ_B and τ_S.

The figure 5.6 shows the variations in both times τ_B, τ_S during different stages of emulsion aging and the changes in air content for an emulsion with 50:50 oil/water ratio and 10^{-4} M surfactant concentration. An immediate observation is that during the initial minutes when creaming occurs rapidly, a ballistic motion dominates: the characteristic time (τ_S) is smaller than the Brownian time (τ_B). As time progresses, the creaming process becomes less significant, as indicated by the fact that the characteristic time of creaming becomes much higher than the Brownian time ($\tau_B < \tau_S$). This result is important for interpreting the dynamics of the sample, as it suggests a transition from ballistic motion to solely Brownian diffusion after creaming takes place.

Furthermore, the figure reveals that as the percentage of air in the sample increases, the creaming process becomes faster (lower τ_S) and ceases earlier. Additionally, it is significant that the final state achieved after creaming appears unaffected by the air content.

The Peclet number (Pe) is a dimensionless parameter used in fluid dynamics to characterize the relative importance of advection (convective transport) to diffusion (molecular transport). It is defined as the ratio of the advective transport rate to the diffusive transport rate and is commonly used to describe the transport of mass, heat, or momentum in a fluid. The Peclet number can be calculated as $Pe = Lv/D$, where L is a characteristic length scale of the system (e.g., the size of the domain or a characteristic dimension), v is the characteristic velocity of the fluid flow and D is the diffusion coefficient of the transported quantity (e.g., mass diffusivity, thermal diffusivity, or kinematic viscosity). Such ratio can also be re-written in terms of times, as a ratio between the characteristic temporal intervals of the system:

$$Pe = \frac{diffusion\ time}{advection\ time} = \frac{\tau_B}{\tau_S} \tag{5.2}$$

The Peclet number helps determine the dominant mode of transport. When Pe << 1, diffusion is dominant, indicating that the transport is mainly driven by molecular random motion. On the other hand, when Pe >> 1, advection is dominant, meaning that the transport is mainly driven by bulk fluid motion. In the intermediate range, where Pe ~ 1, both advection and diffusion play significant roles in the transport process.

In figure 5.6 the Peclet number is initially higher with the smallest amount of air, and diffusion and advection occur at equal times, having the same influence on mass transport ($Pe \sim 1$). Even after creaming is ended, as expected, the number of Peclets tends to zero $Pe \to 0$ (with shear tending to infinity $\tau_S \to 0$), i.e., advection is negligible, and diffusion dominates mass transport.

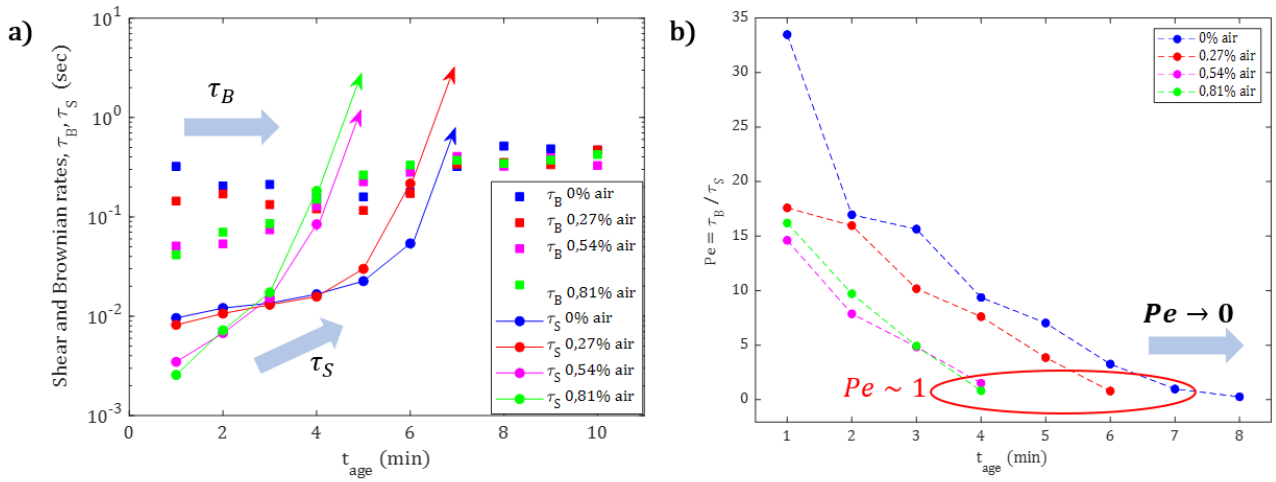

Figure 5.6 a) Brownian and Shear (or ballistic) time as function of aging time and varying air concentration from 0% to 1%, for freshly emulsion with 50:50 MCT oil/water and stabilized by C12EO21 10^{-4} *M. b) Trend of Peclet number* $Pe = \tau_B/\tau_S$.

The same situation is visible by emulsion with 50:50 oil/water ratio but with molar surfactant concentration in solution of $2 \cdot 10^{-4} M$ (figure 5.7). In the first few minutes of the creaming process, a ballistic motion takes over, and as the air content in the sample increases, the creaming becomes quicker and stops earlier.

In this final state, the diffusion coefficient obtained from the Brownian time allows the estimation of a drop radius of 5 μm, which remains consistent regardless of the varying air concentration. This consistency aligns with expectations since the same sample composition, water/oil ratio, and surfactant are maintained throughout the experiment. Notably, air quickly goes up on ground and therefore does not impact the dynamics of the droplets. Moreover, the occurrence of "extra creaming" in samples containing air, as evident from the shear time trend depicted in figure 5.7, where creaming concludes a few minutes earlier for air-containing samples, closely aligns with the duration required for an air bubble to travel in the probed volume. For instance, the computation of Stokes' velocity for a 30 μm bubble indicates an estimated duration of approximately 2.5 minutes for the bubble to exit the probed volume of 10 mm^3.

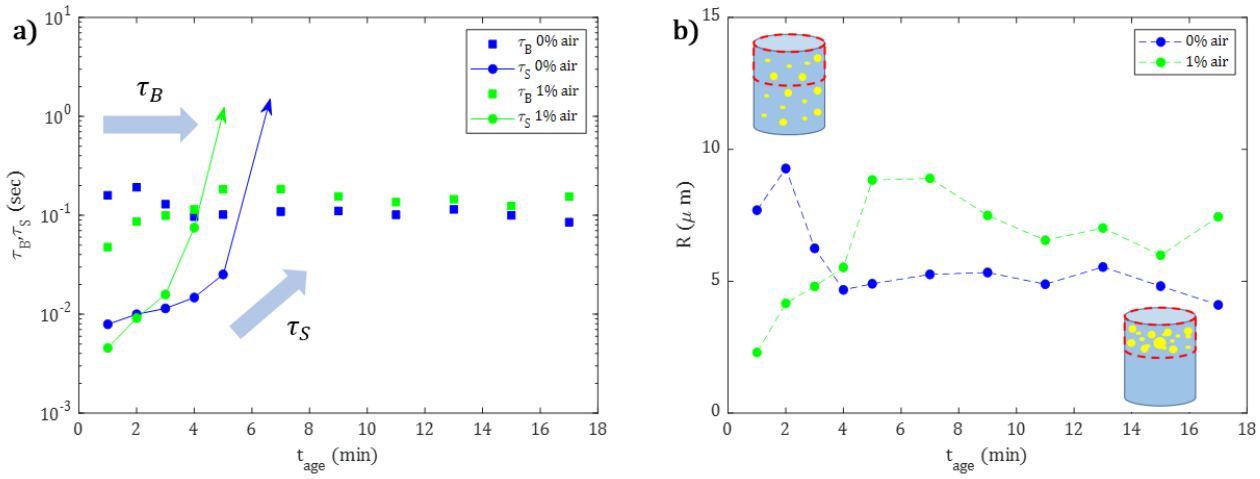

Figure 5.7 a) Brownian and Shear (or ballistic) time as function of aging time and varying air concentration from 0% to 1%, for freshly emulsion with 50:50 MCT oil/water and stabilized by C12EO21 $2 \cdot 10^{-4}$ *M. b) Trend of the rays obtained from Brownian diffusion coefficient (linked to* τ_B*). After about 5 minutes from emulsification procedure, the creaming take place.*

The emulsion mentioned earlier (with a ratio of 50:50 oil/water $2 \cdot 10^{-4} M$) is further analyzed by introducing higher air percentages in the sample, ranging from 1% to 4% (figure 5.8). The mean free path values are measured for four different bubbly emulsions containing 1%, 2%, 3%, and 4% of air. Interestingly, the percentage of air added does not appear to have any impact on this parameter. Similarly, the average radius of the drops in the emulsion remains unaffected by the varying air percentages on ground. Based on the analysis conducted, it is now possible to accurately calculate the relative displacements between the scattering centres. This becomes feasible due to our practical findings, which demonstrate that both the width and mean value of the drop size distribution contribute to the variance of creaming velocities. The standard deviation of velocities σ_v (chapter 3.3) decreases with aging, independently of the air fraction.

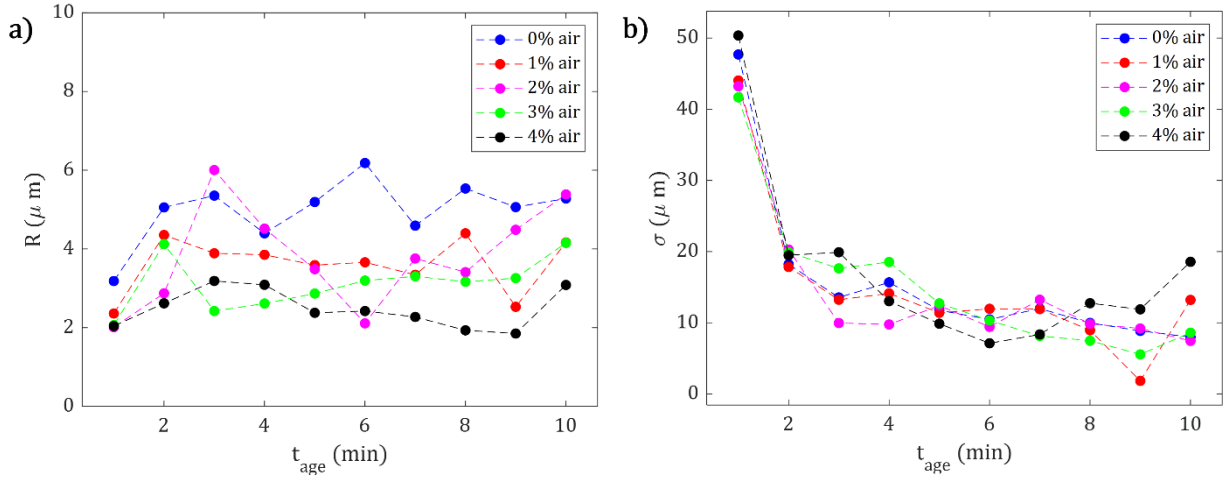

Figure 5.8 a) Drop radius as function of aging time and varying air concentration from 0 % to 4 %, for freshly emulsion with 50:50 MCT oil: water and stabilized by C12EO21 $2 \cdot 10^{-4}$ *M. b) Standard deviation of velocity* σ_v *as function of aging time and varying air concentration from 0 to 4 %, for freshly emulsion with 50:50 MCT oil: water and stabilized by C12EO21* $2 \cdot 10^{-4}$ *M*

5.2 Definition of standard sample reference

Some optical parameters of the instrument require experimental determination, such as the precise measurement of the distance between the laser illumination spot and the BS Corrtector detection area. This is accomplished by measuring a well-defined and stable standard sample. In a broader context, this same standard sample is employed whenever- any uncertainty regarding the data's quality arises during the course of the experimental campaign.

The calibration sample is a suspension of carboxylate-modified polystyrene nanoparticles (CLB9, MDL MFCD00131492, Merck https://www.sigmaaldrich.com/IT/it/product/sigma/clb9) of nominal size $900 \pm 50\ nm$. The surface modification of the nanoparticles provided by the manufacturer prevents aggregation; to further enhance the suspension stability against sedimentation, nanoparticles are suspended in a density matched aqueous phase obtained by mixing normal water H_2O (ultrapure MilliQ) and heavy water D_2O (99.96% D, VWR Chemicals) in a volumetric ratio of 55:45. The density of this mixture, $\rho = 1.05\ g/cm^3$ matches suitably the nominal density of the polystyrene particles at ambient conditions. The stability against sedimentation of this suspension was tested in a standard laboratory centrifuge, applying a 10 g acceleration for 1 minute. No sign of sedimentation was observed.

In DWS experiments, a particle concentration of 0.3 % w/w was chosen, aiming at an optical transport length l^* of the order of 1 mm, close to a typical initial value encountered in the emulsions to be investigated. DLS investigations were conducted on a sample at concentration 10^{-3} % w/w. In both cases, nanoparticles were suspended in the same H_2O/D_2O mixture.

5.3 Calibrations of the apparatus by standard sample

This instrument is developed to perform simultaneous DWS and imaging diagnostics on soft matter samples contained in cuvettes that integrate a piston-based emulsification/foaming device [70], enabling sample generation and characterization to be performed automatically from the ground. Due to technical issues, the detection optics in backscattering collect light from a circular spot, which is offset by a small but a priori not completely determined distance from the spot of the impinging laser radiation. Since this unknown parameter gauges the DWS determination of the mean drop radius in emulsions, it is important to determine it accurately (chapter 4.3).

This chapter sets out the calibration procedure for DWS configurations; this procedure provides a validated data analysis procedure, based on the Monte Carlo simulation of light scattering within the sample, which may be used for the interpretation of any future DWS experiment performed with that configuration. The calibration procedure consists of comparing the DWS experiments on model nanoparticle suspensions, performed on the calibration setup and a reference setup.

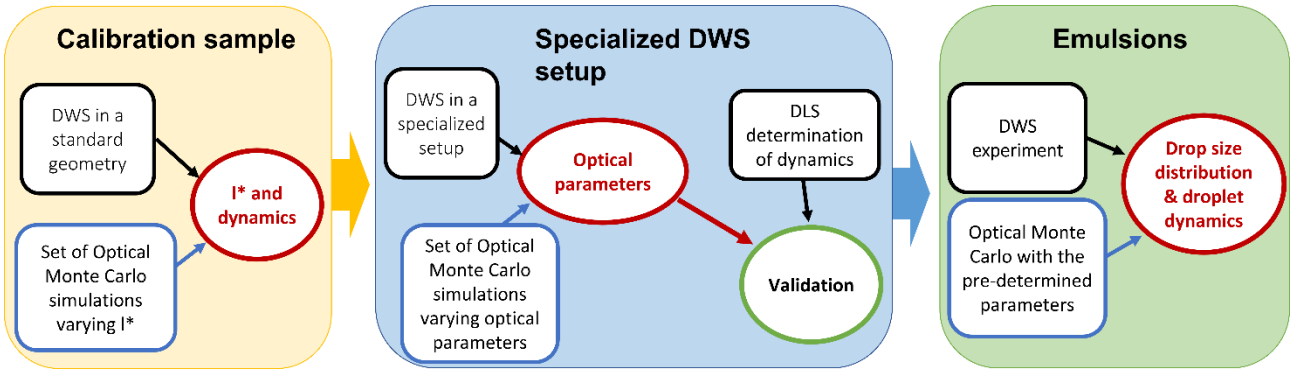

Figure 5.9 The proposed procedure: from left to right, by DWS experiments and a set of Optical Monte Carlo (OMC) simulations, a calibration sample is fully characterized concerning its internal dynamics and the photon transport mean free path l^*. Then, this same sample is measured by the specialized DWS to be calibrated; by analysing the results in the light of MC simulations, the optical parameters of this setup are determined. Finally, this is used (right panel) to investigate the emulsions of interest.

The proposed calibration procedure of a DWS setup is schematized in the diagram reported in figure 5.9. It consists of the following steps:

- Firstly, a calibration standard is prepared, consisting of a stable suspension of polystyrene nanoparticles of uniform size undergoing Brownian diffusion, paying particular care to suppress sedimentation, by a density – matched water phase prepared by mixing normal H_2O and D_2O. Then, this standard is characterized using a DWS laboratory setup based on plane-wave illumination of a wide rectangular cuvette. Analysis with a suitable set of Monte Carlo simulations of $P(s, l^*)$ yields a measurement of l^* and the diffusion coefficient D of the nanoparticles.
- The measurement on the calibration sample is repeated on the specialized DWS setup to be validated, i.e., characterized by one optical/geometrical parameter ("x") whose value is unknown, or is not possible to determine with the required accuracy. The analysis of the data uses a series of $P(s, l^*, x)$ where l^* is fixed to the previously determined value, and "x" is varied on an appropriate range. By finding the $P(s, l^*, x)$ yielding the fit with minimal reduced χ^2, the value of "x" is measured. The approach is validated by consistency checks of the measured value of the diffusion coefficient D. In the case of interest, this parameter corresponds to the unknown distance between the laser entrance spot and the area of collection of light in quasi-backscattering geometry.
- A new set of Monte Carlo simulations of $P(s, l^*)$ is computed for the specialized DWS setup, now validated. They are used to interpret DWS experiments on relevant samples, such as emulsions undergoing ageing, to characterize their drop size distribution and internal dynamics.

As discussed in the previous section, by utilizing a set of simulated $P(s, l^*)$, a fitting procedure can be employed to minimize the reduced χ^2 value for a dataset acquired by two detectors. This fitting routine enables the determination of the optimal fitting parameters.

- For the calibration sample (of known l^*) in an "un-calibrated" setup, the Brownian time τ_B and a geometrical parameter such as optical distance spot-in / spot-out d_{in-out}.
- For a sample measured in a calibrated setup, the relaxation time of the dominant dynamical regime (either Brownian motion or creaming) and l^*.

Chapter 3.2 provides a detailed description of the optical arrangement employed in the laboratory setup of DWS (Parma). In this setup, laser light interacts with the sample and the diffused light is collected in either BS (backscattering) or FW (forward scattering) geometry for subsequent cross-correlation analysis. The signals captured by the two detectors are then directed to an FPGA correlator, utilizing a Xilinx SP605 card, which performs the computation of the autocorrelation function.

DLS experiments were performed using a commercial instrument (Zetaplus, Brookhaven Instrument Corporation) operating in a 90° scattering geometry, equipped with a solid-state laser (λ=658 nm). The instrument has a Peltier stage, stabilizing the sample temperature at T=25°C. Correlograms were analysed by the instrument's proprietary software (DLS software v. 3.34, Brookhaven Instruments) and by our software.

The first step of the calibration procedure consists in the determination of the value of l^* of the calibration sample with a DWS measurement performed with the laboratory setup. Measurements in BS and FW geometries are performed for a total accumulation time of 2 minutes, with typical count rates in the 500-700 kHz range.

$P(s, l^*)$ is calculated by Monte Carlo simulation of photon diffusion within the sample, assuming uniform illumination on the wide side of the cuvette. The simulated $P(s, l^*)$ are then used to model correlation function according to eq. (3.5), to simultaneously fit experimental BS and FW correlograms. The result of the fitting routine is shown in figure 5.10; it results in $l^* = 0.98 \pm 0.1\ mm$. The measured diffusion coefficient of the polystyrene nanoparticles is $D = 4.31 \cdot 10^{-13}\ m^2/s$, in nice agreement with the determination by Dynamic Light Scattering and the expected particles radius $r = \frac{KbT}{6 \cdot \pi \cdot \eta_0 \cdot D} = 450\ nm$.

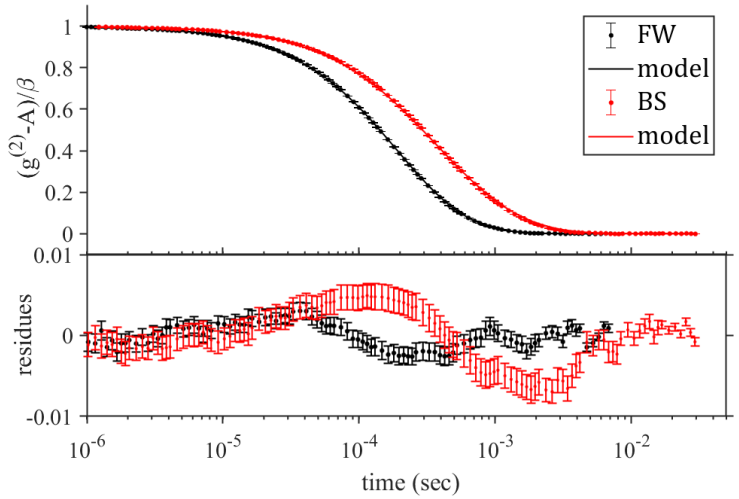

Figure 5.10 DWS transmission (FW, black dot) and backscattering (BS, red dot) correlations function, simultaneously measured on a polystyrene suspension and in laboratory set up. The best fit (black and red lines) results in a determination of l^* and of the diffusion coefficient of the nanoparticles

The DWS experiments on the calibration suspension are repeated on the setup to calibrate the BS APD and the BS line camera of the Engineering Model (EM) on-board equipment, described in chapter 4. The calibration suspension is placed in the Sample Cell (SC) and correlation functions are detected by FW APD, BS line camera and BS APD. The correlograms from Corrtectors are fitted with curves of the model obtained from eq. (3.6), using $P(s, l^*, d_{in-out})$ calculated from Monte Carlo simulations taking the value of $l^* = 0.98\ mm$, previously determined, and varying din out in an interval of 0-3 mm in steps of 10 microns.

Alternatively, the correlations obtained with BS LC and FW APD are used for the validation of l^*. In the case of the LC detector, there is no optical distance between the input and output points d_{in-out}. Thus, when the

correlation functions are adapted at the same time as $P(s, l^*)$, it becomes possible to determine the value l^* obtained with the laboratory configuration even in a different configuration (EM configuration).
Thus, the approach for determining the mean free path of transport, intrinsic parameter of the sample, remains unaffected by the equipment employed.

Note that the variation of the mismatch of refractive indexes $m = \frac{n_{ps}}{n_w}$ of nanoparticles and medium, due to using laser light of different wavelength in the two setups (633 nm in the Laboratory setup and 532 nm on EM) is of the order of $6 \cdot 10^{-3}$[73,74], and therefore it does not affect significantly the value of l^*.

A fitting routine that minimizes χ^2 determines the best fitting parameters, τ_B and d_{in-out} for BS APD and τ_B and l^* for BS line camera. Results of the fit are reported in figure 5.11 and figure 5.12 for BS APD and BS line camera respectively; the best fit values of d_{in-out} and of the diffusion coefficient D are reported in table 2.

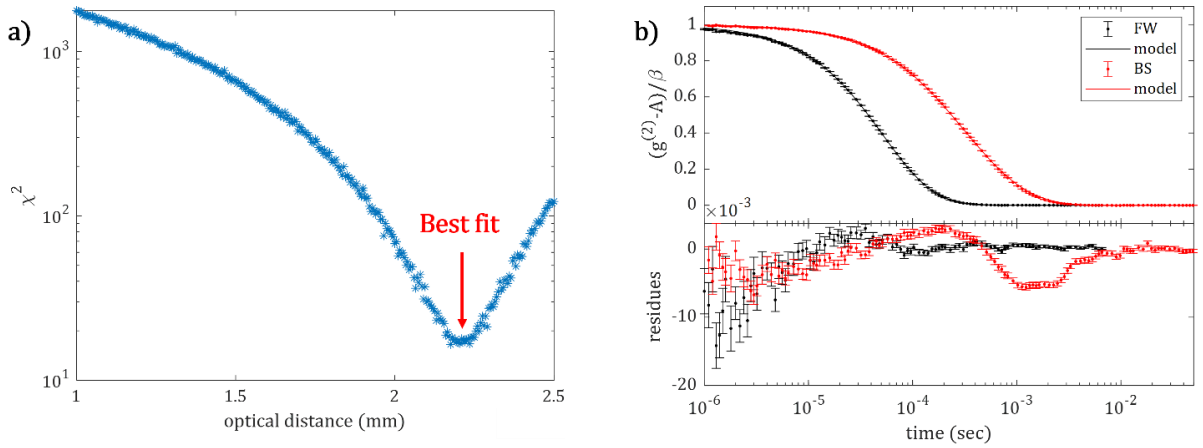

Figure 5.11: a) Reduced χ^2 of the fit for each value of optical distance between spot in and spot out d_{in-out}. The minimum value of χ^2 corresponds to an optical distance $= 2.175 \pm 0.005$ mm for this specific setup geometry. b) DWS transmission (FW APD, black dots) and backscattering (BS APD, red dots) correlations function, simultaneously measured on a polystyrene suspension in Engineering Model set up. The best fit (black and red lines) results in the determination of optical distance d_{in-out} and Brownian time τ_B.

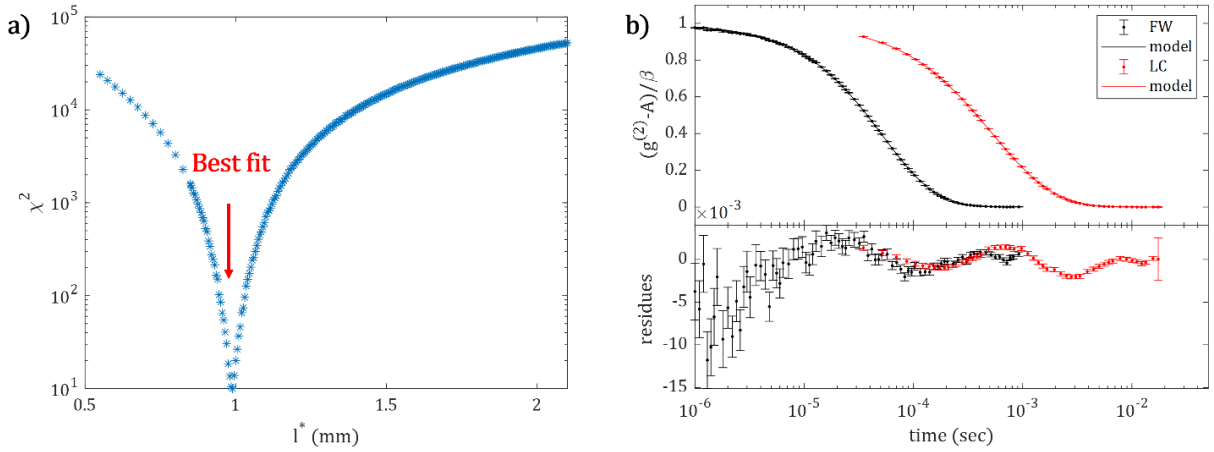

Figure 5.12 a) Reduced χ^2 of the fit for each value of mean free path of transport l^*, without optical distance d_{in-out}. The minimum value of χ^2 corresponds to an $l^* = 0.99 \pm 0.02$ mm b) DWS transmission (FW APD,

black dots) and backscattering (BS LC, red dots) correlations function, simultaneously measured on a polystyrene suspension in Engineering Model set up. The best fit (black and red lines) results in the determination of mean free path of transport l^* and Brownian time τ_B.

	Laboratory setup	***EM setup Corrtector***	***EM setup LC***
Incident light	$633\ nm$ Expanded beam	$533\ nm$ Fiber coupled laser sigma = 0.5mm	$533\ nm$ Fiber coupled laser
$\boldsymbol{d_{\text{in-out}}}$	*N.A.*	$2.175 \pm 0.05\ mm$	*N.A.*
$\boldsymbol{D}$	$4.3 \cdot 10^{-13} \pm 10^{-17}\ m^2/s$	$4.5 \cdot 10^{-13}\ m^2/s$	$4.5 \cdot 10^{-13}\ m^2/s$

Table 2. Results of DWS measurements on the calibration sample. The table reports the value optical distance d_{in-out} and of the diffusion coefficient D measured with the laboratory DWS setup, and with the two BS detectors of the EM setup.

A careful discussion of the intrinsic correlation between the fitting parameters τ_B and d_{in-out} is mandatory to retrieve the experimental error on the value of the diffusion coefficient D. The error over τ_B is evaluated as the half width of the range of τ_B values corresponding to the 2σ width of the minima observed in the dependence of the reduced χ^2 as a function of d_{in-out} (see figure 5.11). This error over τ_B is propagated to obtain the error over the determination of D. The difference of relative errors in the diffusion coefficient measured with APD and with LC (4% and 11% respectively), is due to the slower sensor in the camera, which prevents access to the shorter time scales (see red dot in figure 5.12).
The fact that the values obtained for the diffusion coefficient reported in table 2 are consistent within these errors confirms the validity of our approach and justifies the use of the optical parameters thus obtained to model the interpretation of DWS experiments on emulsion.

5.4 Definition of protocols for the experiments on ISS

The PASTA experiment includes three distinct protocols, each focusing on a different topic and/or optical diagnostic. These protocols are as follows:

- Experimental Protocol for detecting intermittent dynamics with OVC, rough emulsification (referred to as the A0 protocol)
- Experimental Protocol for detecting intermittent dynamics and investigate the first hours of aging with DWS and LC, intensive emulsification (referred to as the A1-2 protocol)
- Experimental Protocol for investigating long aging, intensive emulsification (referred to as the B protocol)

Additionally, there is an extra protocol specifically designed for spot-in/spot-out calibration. It is important to note that this final protocol is exclusively intended for use with sample S123 (see Table 1, polystyrene particles). To obtain calibration measurements for the Corrtector, the sample cell is emulsified, and a 5-minute data collection of Corrtector and LC is conducted. This protocol is repeated five times.

Not all protocols are performed for each sample cell. During Protocol A, the PASTA scientific team decides whether repetitions of Protocol A and/or Protocol B should be performed for a particular sampling cell.
Finally, to ensure stable temperature throughout the experiment's science runs, thermal control is activated.

The A0 protocol is conducted for all PASTA sample cells as a primary diagnostic using the OVC. The sample must be in a pristine, non-emulsified state before performing the A0 protocol. Therefore, the A0 protocol is conducted before any other protocol for the sample cell. Before commencing data recording for the A0 protocol, the uniform illumination and appropriate focus of the top of the sample cell are confirmed by monitoring real-time OVC images. If necessary, adjustments are made to the scan-stage and LED power supply. The ideal scan-stage position is determined in real-time for the installed Sample Cells with the assistance of the PASTA science team. The OVC is set to continuous mode, enabling a live stream of images to be transmitted to the ground. The operator manually issues commands to adjust the scan-stage position based on the live images. Together with the PASTA science team, it is determined whether the current scan-stage position achieves satisfactory focus or requires further adjustments. Once an acceptable focus is achieved, the piston inside the Sample Cell is moved to the top position, near the top window. This facilitates easier targeting for focusing purposes and allows for further fine-tuning of the scan-stage position. Since the scan-stage optimization is conducted before Protocol A0, it is performed using un-emulsified Sample Cells. The determined optimal scan-stage position is incorporated into the parameter tables for all subsequent protocols. This ensures that the designated scan-stage position is directly used during the initialization of the run.
During the recording phase, a single piston stroke is executed within the sampling cell to generate sufficiently large drops that can be effectively monitored using the OVC technique. Utilizing more strokes or fully emulsifying the sample would generate smaller drops that would not be ideal in terms of OVC resolution. After this piston stroke, the recording continues for a duration of 10 minutes before concluding and terminating the recording process.

Protocol A is currently divided into two parts: in the initial phase, a brief duration of data (5 minutes) is being recorded and played back on the ground. The PASTA scientific team determines, based on this data, whether the remaining sections of Protocol A and/or Protocol B should be conducted for the respective sample cell. The primary optical diagnostics employed for Protocol A encompass the LC and the Corrtectors (DWS).
The initial part of Protocol A is performed for every PASTA sample cell. The first step in Protocol A involves emulsifying the sample. To prevent overheating, the emulsion generation system cannot be continuously activated for an extended period. If longer emulsification times are required, the emulsion generation system is activated multiple times for shorter durations, with cooling intervals in between. The standard approach involves using a frequency of 18 Hz and emulsifying for a total of 8 minutes, divided into 4 activations of 2 minutes each with a 1-minute cooling interval. The frequency, duration, amount, and cooling time between activations have been carefully optimized by a set of experiments performed on ground. With the aim of generating a reproducible emulsion, DWS experiments have been performed on emulsions generated by increasing the number of agitation cycles. It was found that for 4 or more cycles, the results where independent on the number of cycles, thus indicating that a reproducible situation can be obtained by this protocol.
After the sample is emulsified, certain settings, such as LED power and scan-stage position (determined during Protocol A0) can be fine-tuned if necessary.
Depending on the time spent on fine-tuning, the sample may need to be re-emulsified before starting the science data recording. Alternatively, recording can commence without re-emulsification. The decision to re-emulsify is made by the PASTA science team.
A five-minute duration of scientific data is recorded. The LC can then be post-processed onboard using default delay times (τ-values) measured in microseconds. The data are subsequently played back to the ground. Both raw and post-processed data for the LC are transmitted to the ground.

The continuation of Protocol A is exclusively conducted when the initial part of Protocol A detects observable intermittent dynamics within the emulsion. This investigation primarily focuses on samples with the lowest concentrations of surfactants, as it is expected that intermittent dynamics will be more evident in such samples. To ensure that the observations begin with a completely emulsified sample, the second part of Protocol A involves re-emulsifying the sample, regardless of whether it remains partially emulsified by the initial part of Protocol A. After achieving complete emulsification, the observation phase commences, during which all the diagnostics are employed to record 2 hours of scientific data. This procedure is iterated three times, with three repetitions dedicated to each sample in the second part of Protocol A.

Protocol B, which is dedicated to studying the aging of emulsions, represents a significant portion of the overall experiment duration. The estimated time required for this protocol is 120 hours, varying depending on the specific samples under investigation. The duration of Protocol B is determined based on the assumption that the samples will not completely de-emulsify within this time frame.

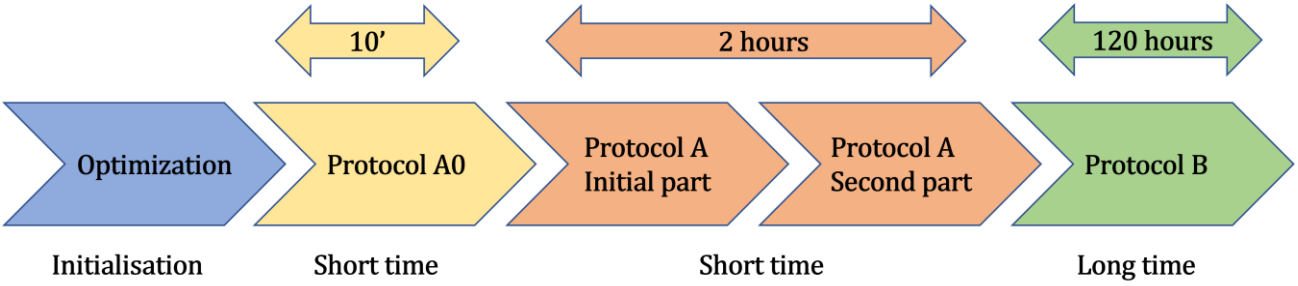

Figure 5.13 Diagram illustrating the initialization and acquisition protocols of the PASTA experiment conducted aboard the International Space Station (ISS). The sequence progresses from left to right and outlines the sequential execution of the various protocols: starting with optimization and progressing through shorter investigation times, a 2-hour Protocol A, and concluding with the extended 120-hour Protocol B, which focuses on studying sample aging.

5.5 Mission Readiness Test

The Mission Readiness Test ensures that the EM operates correctly from a technical standpoint following the re-manufacturing and filling process for the PASTA mission. Additionally, selected ground samples are tested to provide a basis for comparison with the onboard results. This activity encompasses two distinct tests. Firstly, it includes technical check-outs to validate experimental parameters and ensure the proper functionality of both general and PASTA-specific modifications. For example, the laser stability. Secondly, it involves verifying modifications to the microgravity measurement assembly (MMA) data acquisition, optimizing the polarizer loop, validating the A0, A, B processes, and determining l^* on the calibration sample (chapter 5.3).
The polarizers are incrementally rotated in 15-degree steps to conduct reflex diagnostics, and the transmission intensity is recorded at each step. The identified minimum intensity position, the maximum intensity position, and the angle between them are determined until a full 360-degree rotation is completed. The optimum positions of the polarizers correspond to the points of minimum intensity.

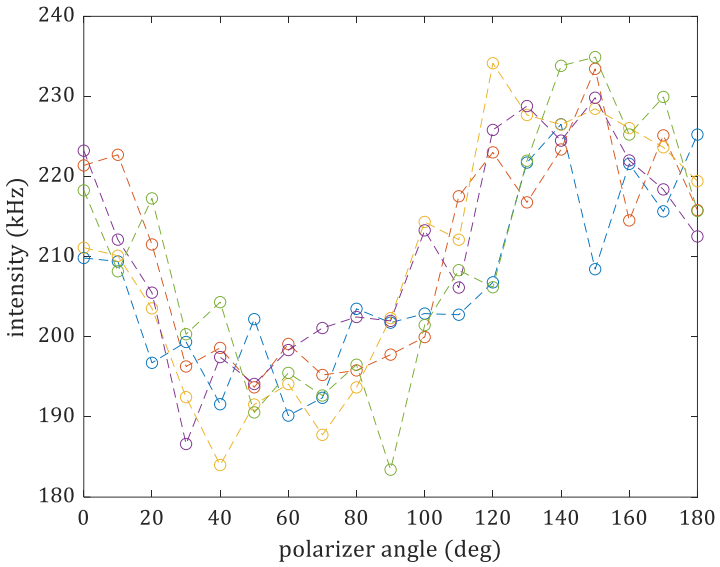

Figure 5.14 Figure shows 5 repetitions of polarizer optimization loop. Then polarizers identified the intensity minima at about 60 degrees, while the intensity maxima is at 150 degrees.

Having determined the optical distance for the EM setup, the same fitting routine used in the first step of the calibration procedure is employed to retrieve dynamical and structural parameters for an emulsion. The value of the optical distance obtained with the calibration procedure is assumed fixed; Monte Carlo simulations of $P(s, l^*)$ for BS and FW are produced, spanning a wide range of l^* with a spacing of 10 μm. For this sample, the model assumes a linear superposition of Brownian and ballistic motion to describe an emulsion subject to creaming.

The experimental correlograms are fit with model curves for BS and FW geometries generated from the simulated $P(s, l^*)$. The fit with the lowest χ^2 yields the desired parameters, namely the transport mean free path l^*, Brownian time τ_B and ballistic time τ_S .

An attractive feature of DWS investigations of emulsions is the possibility to measure drop dynamics as a function of process parameters and aging time and to gain insight into incipient destabilization processes, often hallmarked by fast creaming/sedimentation, as opposed to Brownian diffusion. These two dynamical regimes are characterized by different laws of growth of mean square displacement between scattering centres, and correspondingly by different shapes of decay of the correlation function. Often, as aging proceeds there will be a crossover between these regimes.

Following the analysis scheme described in chapter 3 the standard deviation of velocity distribution σ_v is calculated as follows: from the extracted relaxation shear time τ_S, a decay rate is calculated. This term multiplied by the length scale on which it is calculated (l^*) gives the root of the mean square value of the creaming speed. That is to say $\bar{v} = \sqrt{\langle (\Delta v)^2 \rangle} = \bar{\Gamma} \cdot l^* = 2\sigma_v^2$. Afterwards, σ_v is reported as a function of the aging time. As it can be naturally expected, the highest values of σ_v ($\sim 50 \frac{\mu m}{s}$) are found at early stages, immediately after emulsification phase, where the drops undergo fast creaming. Already in the next few minutes, the value drastically decreases and remains constant for the remaining minutes.

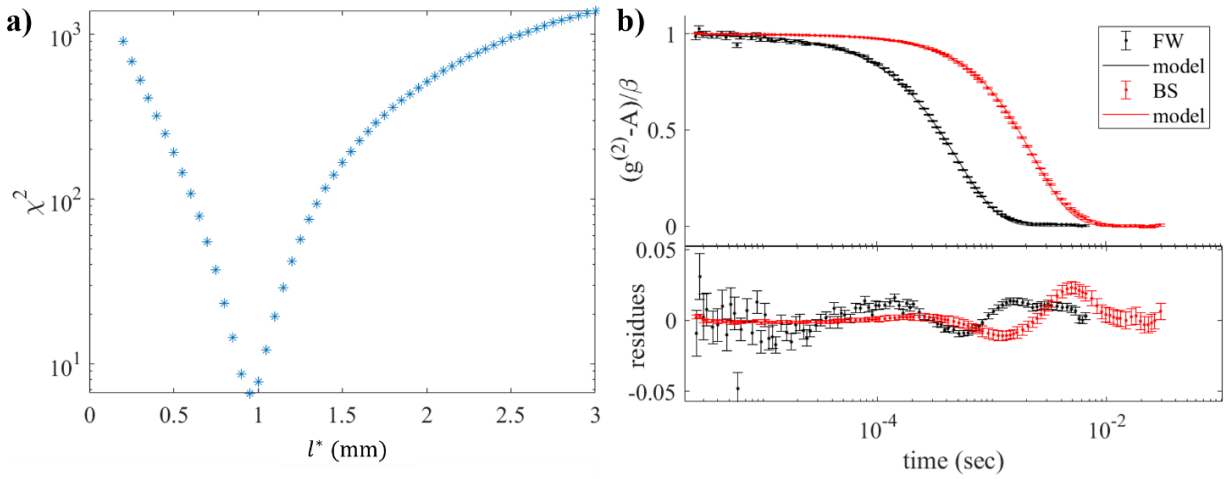

Figure 5.15 a) Reduced χ^2 of the fit for each value of l^* for freshly prepared emulsion with 50:50 MCT oil: water and stabilized by C12EO21, $c = 10^{-4}M$. The minimum value of χ^2 corresponds to a $l^* = 0.95 \pm 0.1\,mm$. b) DWS transmission (FW, black dot) and backscattering (BS, red dot) correlations function, simultaneously measured on a polystyrene suspension and in Engineering Model set up. The best fit (black and red lines) results in a determination of l^*, τ_B, τ_S.

It is evident that the most suitable emulsions for ground-based studies, both on EBB and EM, are those containing a high amount of oil and surfactant. Emulsions with an equal percentage of water and oil (50:50), ideally combined with a higher concentration of surfactant, exhibit greater stability under certain emulsification energies and when using specific sample cells (SC).

On the other hand, emulsions with different compositions, designed for on-board experiments, are not ideal for gravity studies. Due to gravity-driven creaming, these emulsions experience rapid phase separation, leading to destabilization within a very short time. Consequently, extracting the free mean transport path from simultaneous fits of correlation functions in the two transmission and back-diffusion configurations becomes challenging. The correlation functions approach closer at small aging times and eventually overlap, causing an l^* value that quickly saturates to a value near the cell size. This renders the DWS analysis not significant and corrupts the form of the correlation function due to rapid demulsification. In contrast, the behaviour of emulsions changes entirely in microgravity, as we will see in the following chapters. Emulsions with a higher percentage of oil, while more subject to coalescence events, experience faster demulsification compared to those with a lower percentage of oil.

6. The experiment in microgravity on the ISS

Following the initial phase involving preparations for the experiment on the International Space Station (ISS), the four SCU (Sample Container Units) of the PASTA experiment, along with the upgraded SMD EM (Soft Matter Dynamics Engineering Model), are launched together. The SCU units are maintained in a moist environment to ensure the contained liquid does not disperse. Ground operations encompass several activities. Firstly, measurements are conducted on control samples from the EBB (Elegant Bread Board) at the University of Parma. Additionally, new diagnostics are implemented at Airbus Defence and Space in Germany. Mission Readiness Tests take place at the Belgian User Support and Operations Centre (BUSOC) to validate protocols and perform standard calibration procedures. All tests were conducted abroad are supervised by the PhD candidate. The onboard experiment commences with the docking of the spacecraft at the ISS shortly after its launch in February 2022. The experiment extends over a period of six months, during which data are collected in the unique microgravity environment of the ISS. After the completion of the six-month experimental period, the collected samples are carefully transported back to the ground for analysis of the effects of microgravity on the samples.

6.1 Commissioning and optimization

During the installation activities, the crew retrieves the SMD EM and the reference Sample Cell Unit (SCU) for installation purposes. Once the Experimental Container is installed, a functional checkout is conducted, which is entirely managed from the ground. This checkout process involves verifying the proper functioning of various SMD subsystems.

After the installation, the experimental protocol is uploaded, and the first activation of the Experimental Container takes place in orbit. The voltages of the power supply lines from the Fluid Science Laboratory (FSL) to the Experimental Container are checked. Furthermore, all the sensors and actuators, including those for temperature, humidity, illumination, and detectors, are evaluated to ensure they are functioning correctly. Additionally, the operation of the Laser and Corrector subsystems, which encompass attenuators and polarizers, is verified. The PASTA experiment primarily operates from the ground, and under normal circumstances, the crew's involvement is limited to mechanical activities. The ground operations can be divided into two key components: Commissioning/Functional tests, conducted within the first week following the docking of the spacecraft to the ISS, and the PASTA experiment science runs. Ground command operations are predominantly conducted using experimental protocol commands. For routine activities like the science runs, parameter tables are prepared and executed, enabling a semi-automatic execution of the experiment. This approach allows for efficient and standardized procedures during the experiment, reducing the need for continuous crew intervention and ensuring smooth operations.

Following the successful activation of the laser, the intensity of the laser light is measured using various diagnostic tools, such as the line camera, and the Corrtectors in both backscatter and transmission configurations. To assess the laser stability, two separate records are taken, each spanning a duration of 20 minutes. These records utilize a stabilized polystyrene sample (chapter 5.2) placed in SCU 12-3 (flat field). During the long recording, the count rate for both the backscatter and transmission Corrtectors is monitored to ensure good laser performance. Moreover, it is verified that the laser has been operational for at least 1 hour before the recording, and the Moving Tray (MT) has been thermally equilibrated for at least 30 minutes.

In addition to the laser light intensity measurements, the images captured by the line camera are thoroughly analysed. The raw images indicate that sufficient contrast has been achieved. To further evaluate the image

quality, intensity distribution plots, including gray values and normalized values relative to the maximum intensity, are provided. These plots prove the comparability of the obtained results with ground tests.

During the flat field test, the line camera settings are configured to capture the full line width of 2000 pixels at an acquisition rate of 29.000-line rate (lines per second). This setting ensures comparability to the Mission Readiness Test, where the same intensity distribution was observed on the same sample using identical camera settings. This consistency in results reinforces the reliability and reproducibility of the experimental setup.

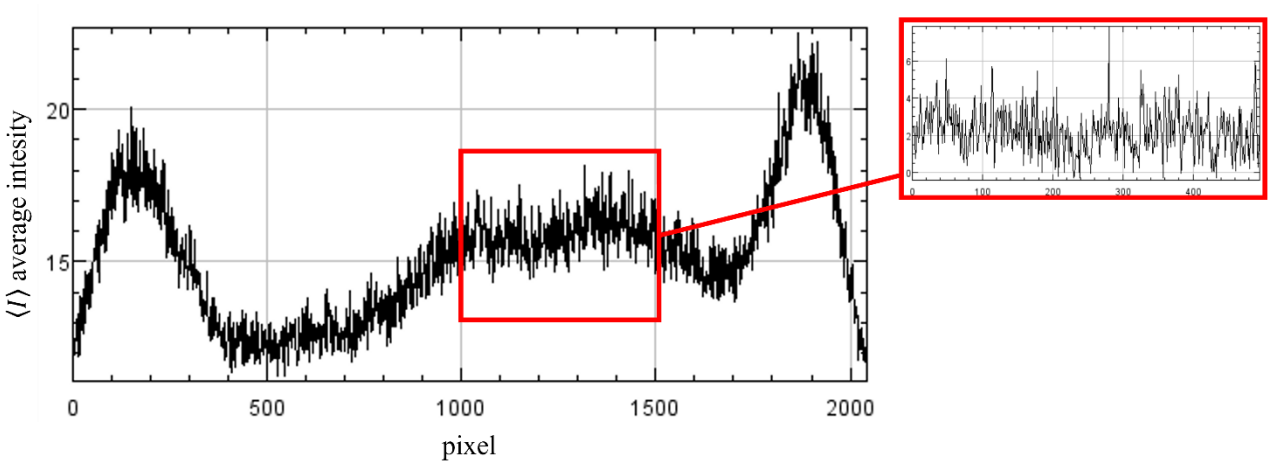

Figure 6.1 Gray value for runs flat field (polystyrene nanoparticles standard sample). The average intensity as a function of pixels is homogeneous in the central 500 pixels ROI (red square).

As part of the commissioning activities, the settings of the Over View Camera (OVC) are thoroughly examined. To accomplish this, the reference SCU was positioned in the observation position, allowing for the acquisition of overview camera images at varying Field of View (FoV) and frame rates. The aim is to validate and verify the intended regions of interest at different digital resolutions, including both 8-bit and 16-bit, as well as increased frame rates of up to 23 frames per second (fps). These tests are conducted to ensure that the desired regions of interest (ROI) are accurately captured by the OVC and that the camera settings functioned as intended. OVC focus occurs by focusing on the upper cover frame of the sample cell and then 4.2 mm below (just below the upper window). In our case, the focus is moved inside the cell, and the cell cover is in a scan stage position of about 2500. The OVC exposure time is fixed at 900 ms and the ROI is 2448 x 2048.

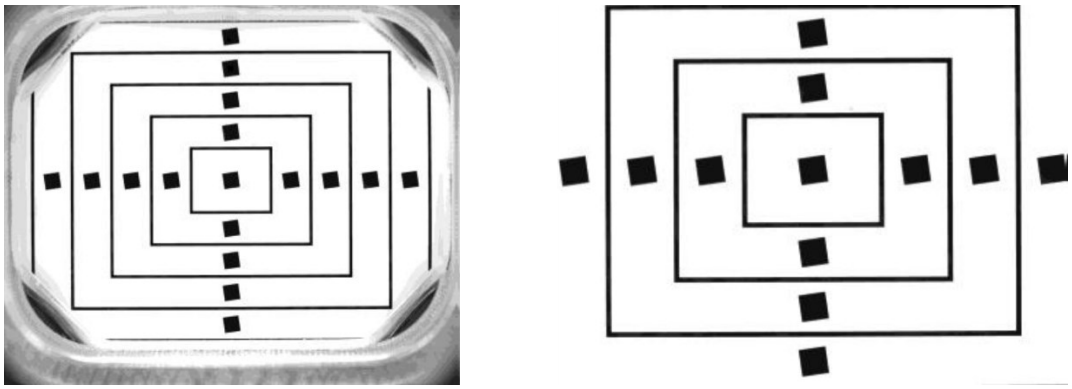

Figure 6.2 Over View camera images acquired for 16-bit depth with FoV of 2448 x 2048 (left), 1600 x 1200 (right)

The successful validation of the functional performance of the A0 and A1-2 protocols is confirmed through various means, including the examination of OVC images. These images provide visual evidence of the sample cell's condition before and after the shaking process. In the OVC images (figure 6.3), the images at the top of the panel represent the virgin sample after its installation in orbit, while the image at the bottom shows the same sample after the application of shaking protocol A0. The presence of an air bubble in each sample is a deliberate inclusion to compensate for thermal expansion. In the left images, the air bubble is partially visible at the top of the sample cell, whereas in some cases, multiple bubbles can be observed near the top or even throughout the sample, showing the presence of floating air within.

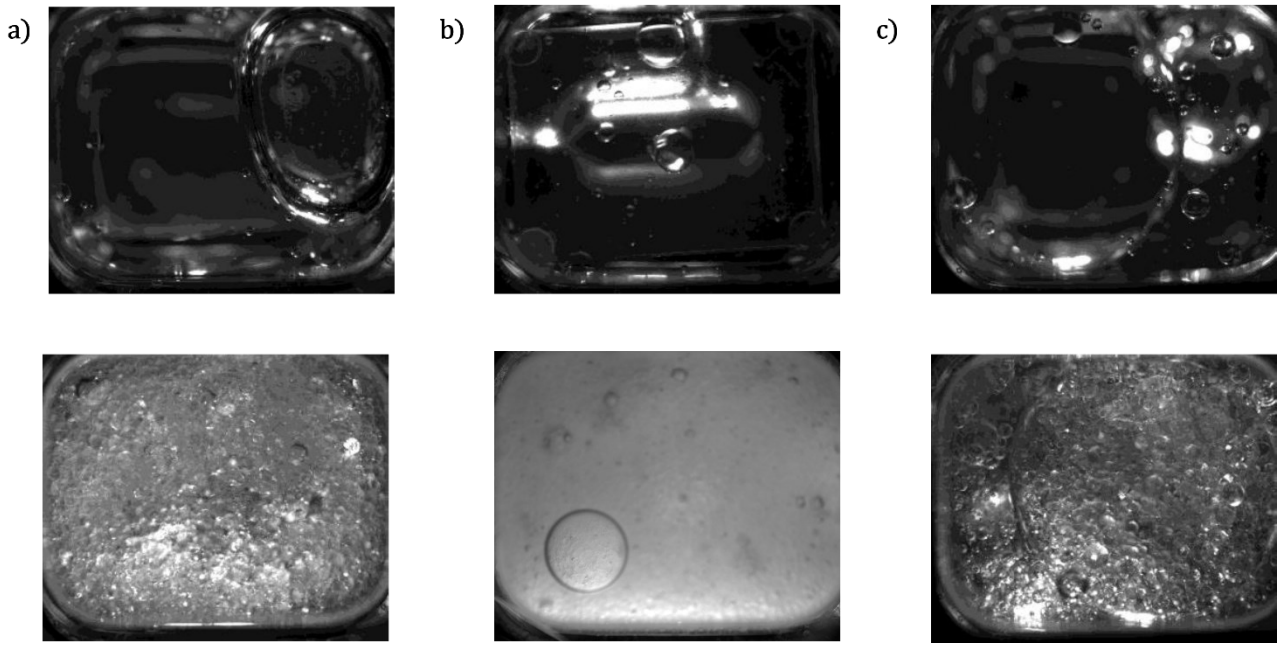

Figure 6.3 OVC Images of processed SC's before / after A0 protocol (initial emulsification of samples): in panel a) is shown sample SC 09-1 (20:80 o/w 10^{-5} *M), in panel b) is shown sample SC 10-1 (30:70 o/w* 10^{-5} *M) and finally in panel c) is shown sample SC 11-1 (50:50 o/w* 10^{-5} *M).*

The verification of Corrtector data for the A0 protocols confirms that they exhibit the expected behaviour. The recorded Corrtector data during the A0 runs demonstrates reasonable characteristics, with relatively high transmission count rates and lower backscatter count rates. These results indicate a high level of transparency in the samples, achieved after only a short emulsification process. As an illustration, the SC 09-1 runs following the A1 to A2 protocols are presented. The emulsification process is successful, although some larger droplets are visible in the samples. These droplets are presumed to be air bubbles that are dispersed and floating throughout the sample. The ratio between transmission and backscatter intensity is significantly close to that of an on-ground experiment and the intensities fall within the typical count rates for a fully emulsified sample. This behaviour is consistently observed in both A1 and A2 recordings. Variations in the emulsion structure can be observed in the raw line pattern and the plotted gray values, indicating the presence of different emulsion structures within the samples.

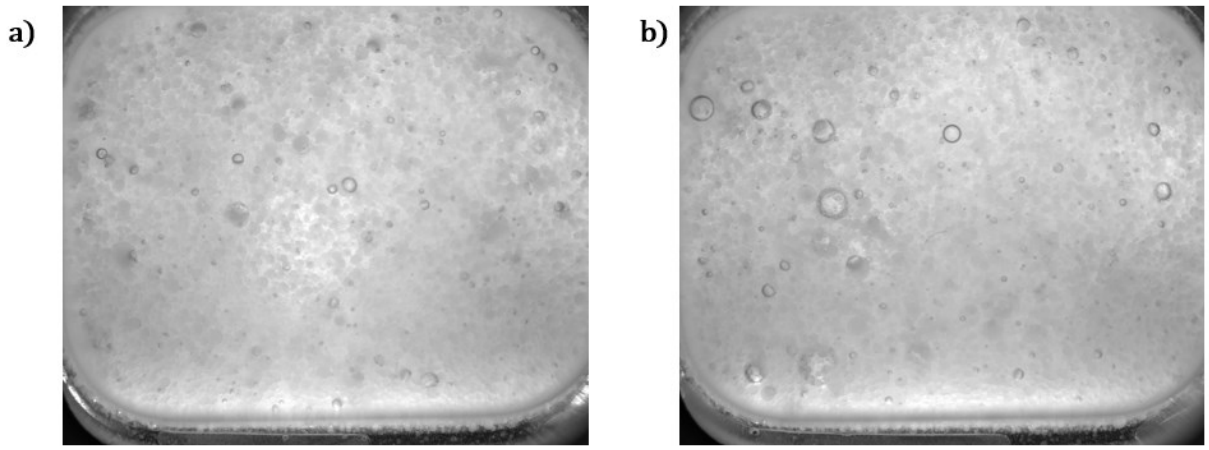

Figure 6.4 Sample SC 09-1 (20:80, $10^{-5}M$) images from OVC data. The a) panel shows the sample in A1 protocol recording, while the b) panel shows the sample in A2 protocol recording.

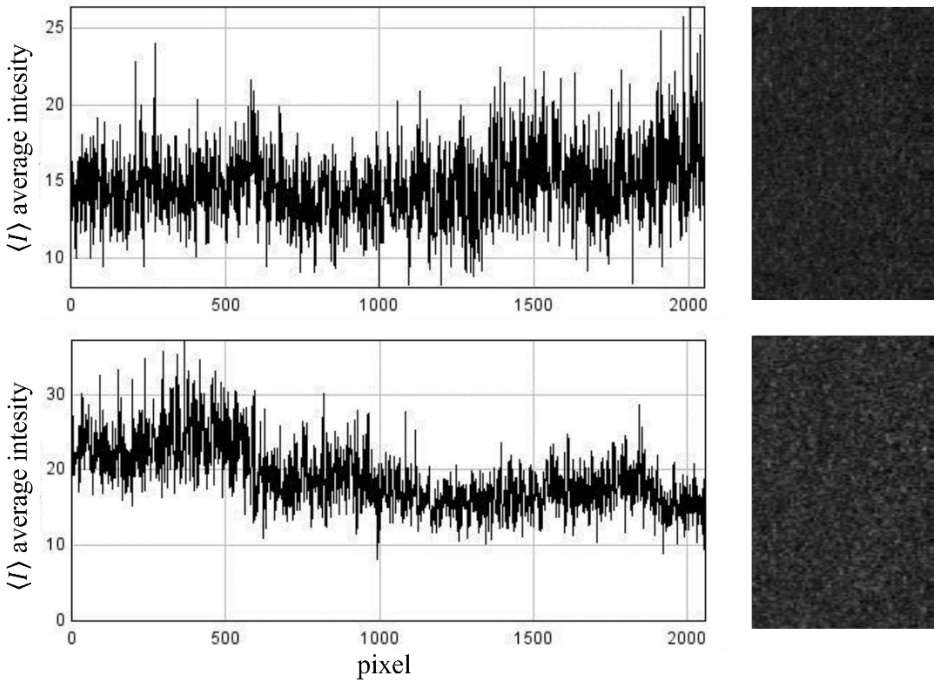

Figure 6.5 Sample SC 09-1 (20:80, $10^{-5}M$) average intensity as function of pixel from LC data. The top panel show the sample in A1 protocol recording, while the bottom panel show the sample in A2 protocol recording.

Upon successful validation of all acquisition optics on board, the calibration sample, consisting of diameter 900 nm polystyrene particles used during the Mission Readiness Test on the ground, is employed. Correlation functions for the nanoparticle suspension are acquired in both backscattering and transmission configurations using the line camera and Corrtector.

To determine the mean free path of transport l^* for the calibration sample, a series of measurements is conducted. Initially, two-minute measurements are taken without shaking the sample, and this process is repeated five times. Subsequently, another set of two-minute measurements is performed, but this time after vigorously stirring the sample at 18 Hz for 2 minutes with four cycles as the complete emulsification process.

For these measurements, the polarizers used in the Corrtector are set in the same manner as the preliminary ground-based measurements: the backscattering configuration is set with a rotation of 60 degrees (representing minimum intensity), and the transmission configuration is held at 0 degrees. The parameters of the line camera remain unchanged, employing the minimum allowed exposure time with a ROI where the average intensity in the working pixels is consistent across the central 500 pixels and full height, as illustrated in figure 6.1. In addition to the standard measurements, longer duration measurements are performed on the calibration sample to obtain the flat field and dark field data, which are crucial for calibration and background subtraction purposes.

The subtle variation in the decay of the correlation function (figure 6.6) acquired before and after the shaking process likely arises from the presence of bubbles within the polystyrene, leading to sample heterogeneity once the shaking process is completed. While the difference in the decay of the correlation function acquired using DWS or LC is due to the variation in the optical distance between the input and output lighting spots for the two different detectors.

A slight change in the decay of the correlation function has a small impact on the calibration parameters. By employing the fitting procedure outlined in the previous chapter, it is deduced a mean free transport path l^* of 0.99 ± 0.02 mm for the sample acquired before the shaking process, i.e., before undergoing "emulsification procedures". However, this value slightly increases to 1.02 ± 0.02 mm after the shaking process. The diffusion coefficient $D \sim 4.34 \cdot 10^{-13}$ m^2/s obtained from the Brownian time τ_B remains nearly unchanged, showing a particle radius of approximately $r \sim 450$ nm, as expected. These findings demonstrate the sensitivity of DWS technique to even minor changes in the correlation function's decay, allowing to extract crucial parameters like l^*, D or the Corrtector optical distance d_{in-out} with precision.

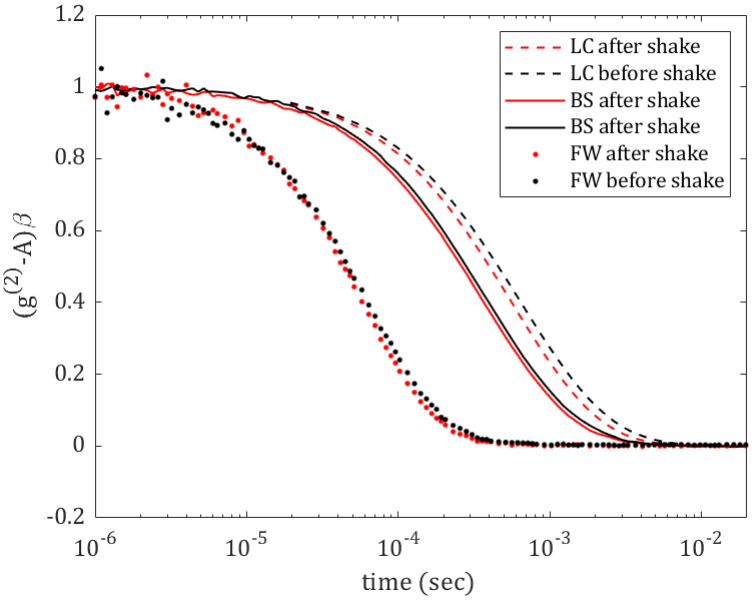

Figure 6.6 Polystyrene Correlation function in Backscattering from APD (line), Backscattering from LC (dashed line) and Transmission (dot) acquired on board the ISS before (black) and after (red) the full shaking procedure.

The following images show the simple relaxation time in Backscattering and Forward before and after the calibration sample shaking process. Upon analysing the OVC images, noticeable air bubbles are observed in the sample following the emulsification procedure. Furthermore, the decay of correlation function exhibits

slight shifts towards longer times after the shaking process. This phenomenon likely occurs as larger bubbles are being released from their adherence to the wall, as the figure shows.

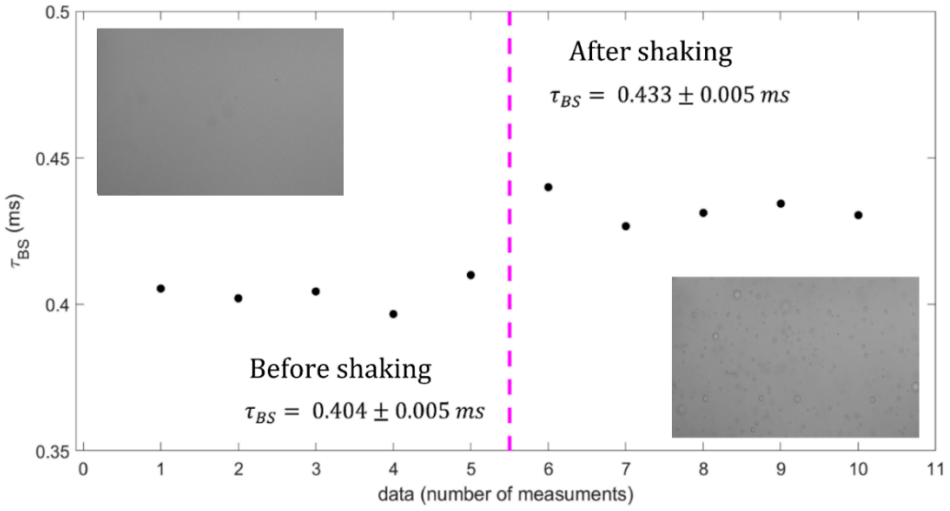

Figure 6.7 In this figure the relaxation time of Backscattering Correlation function from APD for each measurement of polystyrene sample (5 measures of 120 seconds) before and after the "emulsification" procedure (i.e., shaking of the sample at 18 Hz for 2 minutes and 4 cycles) is shown.

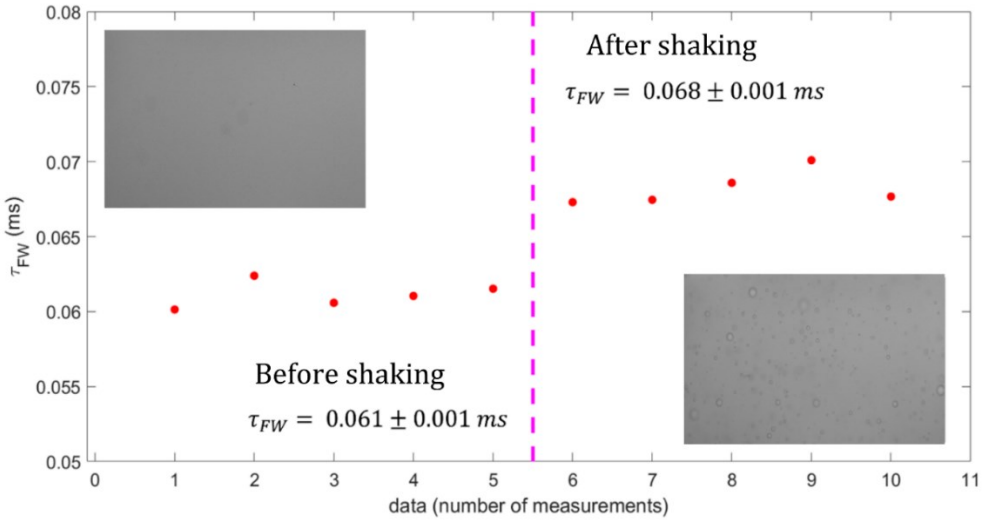

Figure 6.8 In this figure the relaxation time of Transmission Correlation function from APD for each measurement of polystyrene sample (5 measures of 120 seconds) before and after the "emulsification" procedure (i.e., shaking of the sample at 18 Hz for 2 minutes and 4 cycles) is shown.

6.2 DWS investigation of emulsion: average values and relaxation time

Previous studies [53,75–78] have unequivocally proved the effectiveness of DWS in situ for investigating the colloidal behaviour of emulsions. It allows the study of destabilization mechanisms without the need for dilution or other invasive methods. This section provides a preliminary heuristic analysis, conducted in real-time during the campaign. This analysis serves as a guide in the selection of experiments to be performed, revealing the principal trends in sample evolution, contingent upon their composition and time. The detailed analysis, which is based on the $P(s)$ framework outlined in chapter 7.1, subsequently provides precise values for the relevant parameters.

Simultaneously analysing DWS correlation functions in transmission and backscattering on the same samples enables the determination of the photon mean free path of transport, denoted as l^*. In emulsions and foams, experimental observations have revealed that l^* is proportional to the ratio of decay times in backscattering and forward scattering. Additionally, the decay of DWS correlation functions holds valuable information about internal dynamics. When an overlap exists between the two decays, it indicates that the mean free transport path is approximately equal to the size of the sample cell. For emulsions, these dynamics can include translational diffusion of individual droplets, fluctuations in droplet shape, or rearrangements involving multiple droplets. By analysing the decay of the correlation function, one can obtain the mean square displacements (MSD) [51,79] associated with these motions.

Temporal analysis of the intensity of backscattered and transmitted laser light in DWS provides relaxation times for correlation functions that can be linked to the internal dynamics and structure of the emulsion. Generally, the backscattering signal corresponds to the size of scattering objects (droplets), while the transmission signal is more indicative of the number of these objects. A qualitative analysis of the decay of the correlation function acquired onboard and, on the ground, provides insights into the type of dynamics. Firstly, it is observed that the ground measurements exhibit a more compressed decay shifted towards shorter times, indicating the creaming of oil drops driven by gravity. Such effects are suppressed in measurements collected onboard.

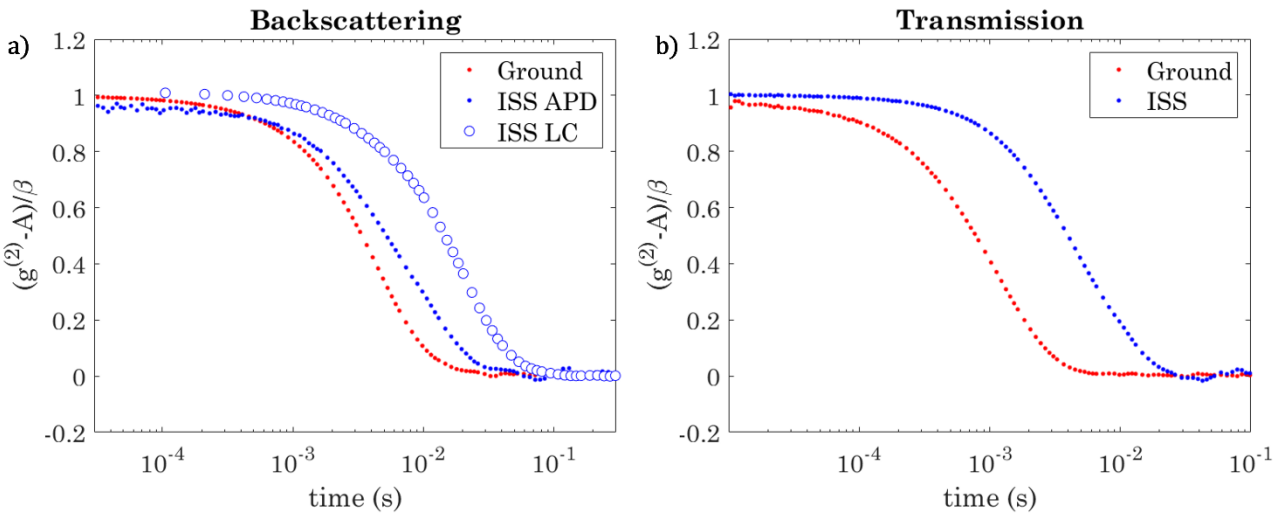

Figure 6.9 Emulsions 11-3 ($2 \cdot 10^{-4}M$ 50:50 o/w) Correlation function in Backscattering (panel a)) and Transmission (panel b)) acquired on ground (red dot) and on board the ISS (blue dot from APD and blue circle from LC). The difference in the decay of the correlation function acquired using DWS or LC can be

attributed to the variation in the optical distance between the input and output lighting spots for the two different detectors.

In the presented figure (figure 6.10 and 6.11), the relaxation time is plotted against the age of the emulsion, with a focus on three distinct water/oil fractions used during preparation. The temporal evolution of the samples reveals distinct trends and indications of coalescence.

Interestingly, at higher concentrations $2 \cdot 10^{-4}\ M$ (figure 6.10), the average free path of transport, represented qualitatively by the dynamic ratio in transmission and retro diffusion acquisition, remains relatively constant across different oil-water concentrations. The relatively constant value of l^* at low oil content (20:80 o/w and 70:30 o/w), obtained through an approximation of the first order $\sqrt{\frac{\tau_{BS}}{\tau_{FW}}} \approx L/l^*$ (with L = size of the cell) suggests that the average drop size remains unchanged in time: $\tau_{Brown} \sim 6 \cdot \tau_{BS}$ implies $drop\ size \sim 3 - 10$ µm.

While, as the amount of oil increases (50:50 o/w), a greater number of drops are formed during emulsification process, and their sizes become larger with ageing.

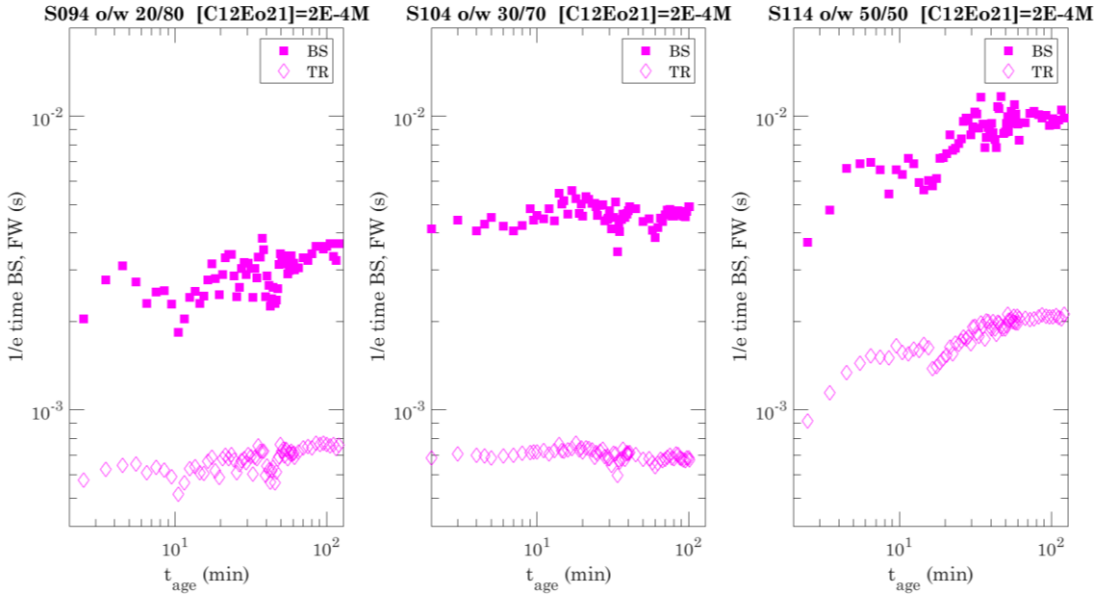

Figure 6.10 Relaxation time of the backscattering (filled squares) and transmission (empty diamonds) correlation functions, as a function of the time from emulsification for the PASTA samples: from left to right increase of oil fraction (20:80, 30:70, 50:50 oil/water ratio) and surfactant (C12EO21) concentration $2 \cdot 10^{-4} M$ *in water.*

In contrast, for lower concentrations of surfactants (figure 6.11), the mean free transport path varies depending on the amount of oil present in the emulsion, and the drops tend to be larger on average. As the oil fraction in the water increases, it exhibits clearer signs of coalescence: l^* grows faster in time as a result of more frequent drop collisions.

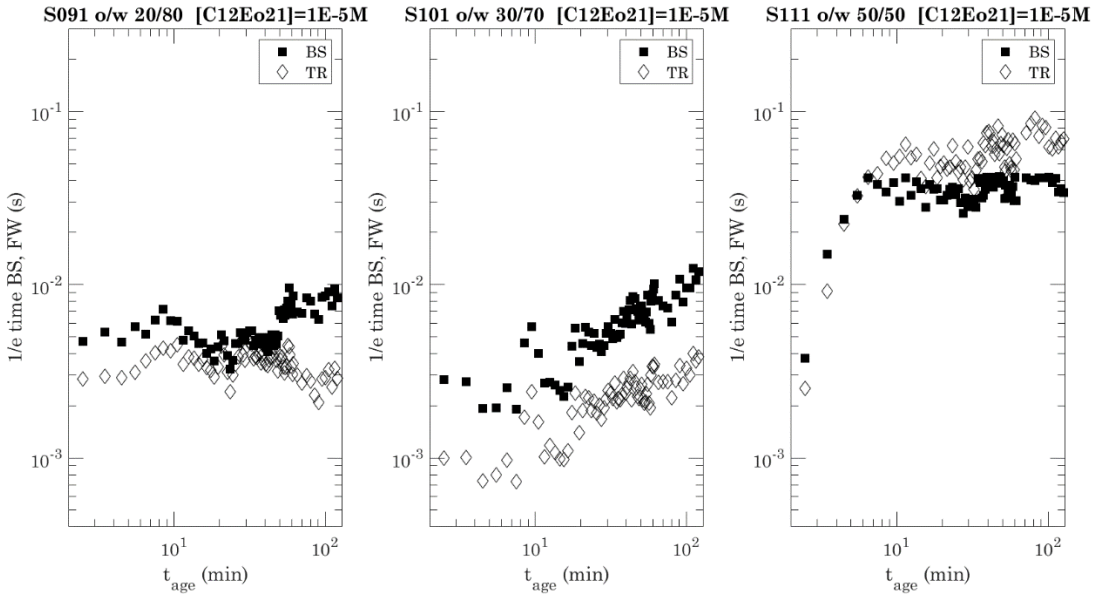

Figure 6.11 Relaxation time of the backscattering (filled squares) and transmission (empty diamonds) correlation functions, as a function of the time from emulsification for the PASTA samples: from left to right increase of oil fraction (20:80, 30:70, 50:50 oil/water ratio) and surfactant (C12EO21) concentration 10^{-5} *M in water.*

The first analysis of the mean values of l^* and relaxation times obtained from the DWS data in the PASTA experiment offers a qualitative understanding of the emulsion ageing phenomena under conditions that cannot be replicated on the ground. However, to delve deeper into the underlying processes involved in the evolution of emulsions (such as coalescence, aggregation, and Ostwald maturation), the subsequent chapter will present a more detailed analysis (chapter 7.1). By employing specialized modeling techniques with DWS, it becomes possible to move beyond average values and gain insights into the specific characteristics of these processes.

7. Main results from detailed analysis

7.1 Intrinsic evolution of relevant parameters

The following analysis is compared with the measurements conducted by our collaborators at AUTH, Thessaloniki, Greece.

As previously described in chapter 3, our method involves fitting pairs of DWS correlation functions measured in both backscattering and transmission. This fitting process allows us to accurately determine the parameters that capture both the structure and dynamics of the system. Additionally, it enables us to disentangle the contributions of Brownian and ballistic movements, which are responsible for the relative displacement of emulsion droplets acting as light diffusion centres.

When Brownian and ballistic motions coexist, assuming the eq. (3.5) the decay of g_1 is modelled by considering both diffusive and ballistic dynamics.

$$g_{1,s}(t) = \exp\left(-\frac{1}{3}\frac{s}{l^*}k_0^2\,(6Dt + (vt)^2)\right) \tag{7.1}$$

in which k_0 is the light wave vector in the medium. This relation accounts for both diffusive and ballistic dynamics, the former being characterized by the Brownian diffusivity D, the latter by the "ballistic velocity" v representing the average velocity of displacement between scattering centres.

This becomes significant in emulsions, especially under microgravity conditions, where the stationary dynamics are expected to be predominantly diffusive (possibly affected by confinement at higher volume fractions of the dispersed phase). However, ballistic motion may arise due to creaming or sedimentation under standard gravity conditions or appear as a transient acceleration of dynamics in microgravity, as explained in the following. In the context of normal gravity, ballistic motion primarily results from creaming or sedimentation, which is excluded under microgravity conditions. On the contrary, in microgravity, a possible source of ballistic motion is the occurrence of drop-drop coalescence, driven by hydrodynamic correlations or Marangoni-like forces generated by surfactant gradients. This mechanism is illustrated in figure 7.1 below and deserves to be discussed in detail: the coalescence of two drops leads to a merged drop with an interfacial area smaller than the sum of the initial individual interfaces. This brings out of equilibrium the surfactants adsorbed at the oil/water interface, prompting some surfactant molecules to desorb, returning the system to equilibrium. Consequently, a gradient of surfactant concentration emerges in the surrounding continuous phase near the site of coalescence. This gradient generates Marangoni-like forces that act on nearby droplets, inducing ballistic movement in the region where the coalescence event occurred. Aside from this effect, hydrodynamic correlations may also play a significant role. For instance, when two relatively large drops merge, a flow field is generated nearby, which can drag smaller droplets from the surroundings, thereby inducing transient ballistic motions.

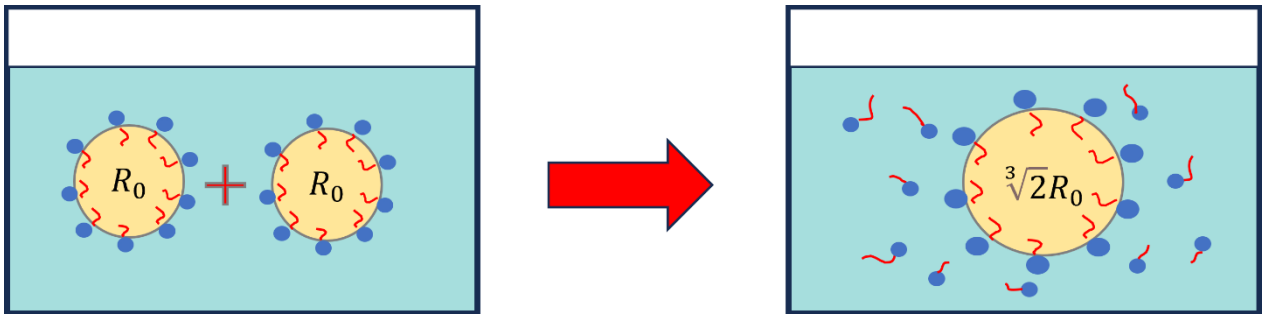

Figure 7.1 The Marangoni effect arises when there is a gradient in surface tension on the liquid's surface, caused by differences in temperature, concentration, or composition. Regions with lower surface tension tend to experience a net inward flow, pulling liquid from regions with higher surface tension. As a result, the liquid moves and generates flow patterns that can lead to a range of interesting effects, such as the spreading of liquid droplets. The figure demonstrates an event where the merging of two drops results in a reduction of the interfacial area. This reduction triggers the desorption and release of surfactant in solution. Therefore, a gradient of surfactant concentration forms in the continuous phase, giving rise to a Marangoni effect.

7.1.1 Droplet Size Distribution from microscopy

Before presenting the analysis, it is essential to understand the concept of a bimodal distribution, employed by our colleagues at AUTH for their data analyses. A bimodal distribution is a statistical distribution that has two distinct peaks, or modes, in its frequency distribution. In other words, the data in a bimodal distribution tends to cluster around two different values. Bimodal distributions often indicate that the data being analysed comes from two different subpopulations or processes that have distinct characteristics.

In AUTH, emulsification experiments took place using the same experimental conditions and were conducted on-ground with an experimental device developed for the evaluation of emulsion dynamic behaviour and stability under low gravity conditions. Droplet breakup is accomplished by the periodic up-and-down movement of a plate, fixed at the tip of a piston, inside a cell triggered by a stepper motor. The gap between the plate and the cell walls is the same as in the Soft Matter Facility. A detailed description of the hardware can be found in [73]. After the end of the emulsification process, the bottom valve of the experimental cell is opened, and the emulsion is drained into a polypropylene tube that contains a dense solution of sodium dodecyl sulfate (SDS) to inhibit droplet coalescence. The diluted emulsion is then mildly shaken to become homogeneous, and a sample of 0.2 mL is placed on a microscope slide with a cover glass above. A transmitted light optical microscopy (Axiostar Plus, Zeiss) combined with a Canon Powershot A640 video camera is used to obtain high-resolution (10 megapixels) images of oil droplets. These images are finally analysed with BubbleSEdit software to determine droplet size distribution. Each experiment involves the measurement of a substantial population, consisting of a minimum of 1500 droplets. Typical images processed to estimate droplet size probability density functions appear in figure 7.2.

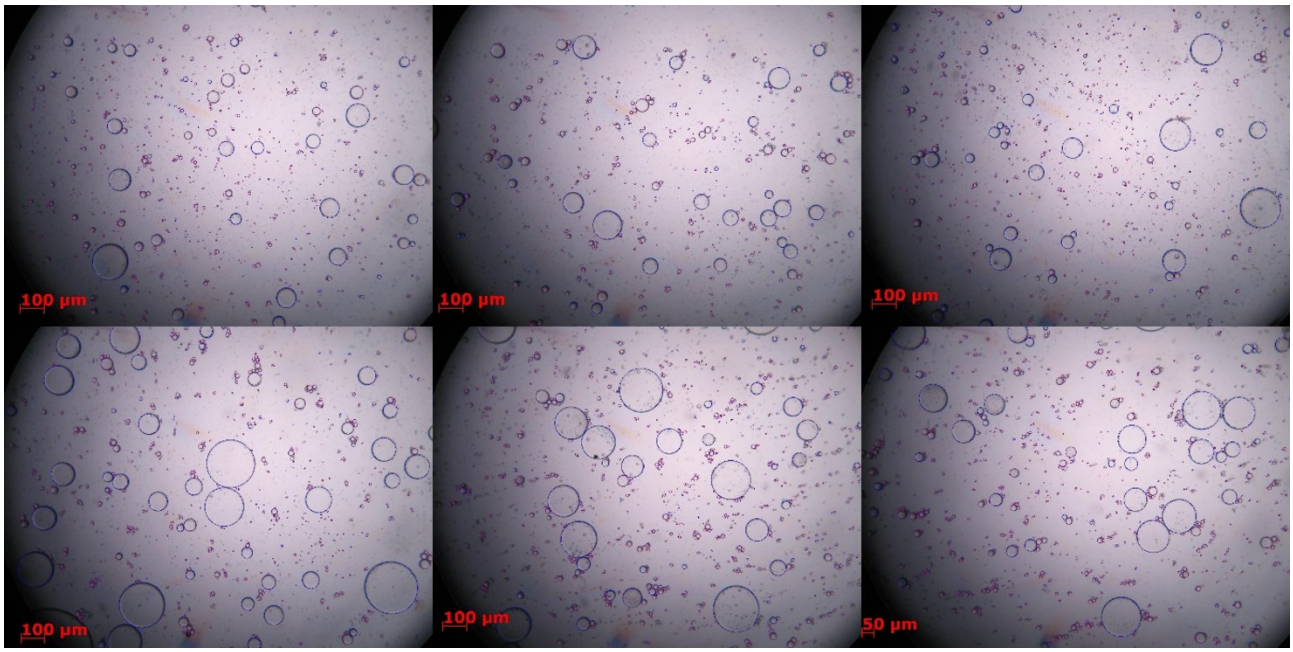

Figure 7.2 Representative microscopy images of droplet population in emulsion S092. Images provided by AUTH, Thessaloniki, Greece

The radius of the measured droplets is exported from the software, and after some mathematical calculations, the droplet size distribution is obtained. The distributions are determined in terms of the probability density function (PDF).

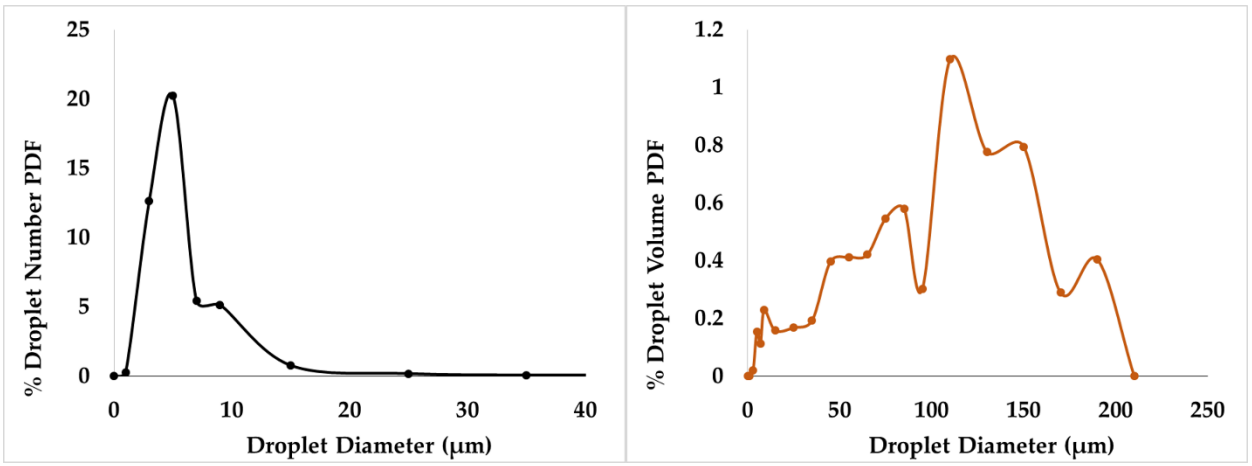

Figure 7.3 Droplet Size Distribution for S092. Respectively droplet number density function (left) and droplet volume probability density function (right). Distribution provided by AUTH, Thessaloniki, Greece.

That image-based techniques possess a detection threshold for droplet sizes, the minimum discernible droplet size stands at 1.64 µm. The fact that the droplet number PDF and droplet volume PDF have very different maxima is a direct outcome of the broad nature of droplet size distribution. To address this, the proposed procedure involves approximating the distribution with a bidisperse model. This particular distribution can distribute the droplet number and volume in separated droplet size regions, as is the case for the observed experimental distributions.

The moments of a distribution are often used to characterise broad or multimodal distributions. Moments are defined as density functions of a random variable. The assignment of the experimental distribution to a bidisperse one is performed employing the so-called quadrature method of moments. Let us assume that there are registered N droplets with diameters d_i (i = 1, 2… N). The normalized moments of the droplet size distribution can be computed as follows:

$$M_k = \frac{\sum_{i=1}^{N} p_i d_i^k}{N} \tag{7.2}$$

The k-th order of moments is associated with various parameters, including the number of drops, diameter, surface, and volume employed. A bidisperse distribution involving two diameters of droplets d_s (small) and d_L (large) is then considered. This analysis assumes the counting of small droplets w, the counting of large droplets 1-w and the values of their diameters, the moments of which align with a system of three non-linear equations. The M_0 moment is automatically matched by such a choice. The other three moments are matched by finding proper values for d_s, d_L, w. The resulting equations are:

$$\begin{aligned} M_1 &= w d_s + (1-w) d_L \\ M_2 &= w d_s^2 + (1-w) d_L^2 \\ M_3 &= w d_s^3 + (1-w) d_L^3 \end{aligned} \tag{7.3}$$

The results of the calculations appear in the following Table 3

Sample	Small droplet diameter (μm)	Large droplet diameter (μm)	% Volume fraction of small droplets	% Number fraction of large droplets	Mean diameter (μm)
S091	4.89	125	0.75	0.7	5.81
S092	6.04	94	1.3	1.9	7.78
S101	6.76	105	1.8	1.4	8.17
S102	5.29	128	0.65	1	6.58
S111	6.87	108	0.55	4.4	11.37
S112	8.38	191	0.35	2.4	12.70

Table 3 The distinct droplet diameters within the resulting broad distribution are closely cantered around 5 μm for small droplets and around 100 μm for large droplets. Specifically, the larger droplets make up approximately 1% of the total droplet count, while the smaller droplets constitute about 1% of the total droplet volume. Data provided by AUTH, Thessaloniki, Greece.

7.1.2 DWS investigation of emulsion evolution

Based on the methods developed by us, as explained in chapter 3.1, drop dynamics can be extracted and interpreted. Brownian diffusion is primarily observed in the smaller droplets, enabling the determination of the drop radius and the identification of potential superimposed ballistic velocity. The inherent dynamics of Brownian diffusion are observed in microgravity across all samples and at every stage of ageing. In contrast, the presence of ballistic velocity suggests the occurrence of transient dynamics. Remarkably, the decay of the DWS correlation function is minimally influenced by the contribution of large droplets, in fact very large drops (tens and hundreds of microns in size) do not contribute significantly to the decorrelation of the scattered intensity in DWS formalism. However, by comparing the volume fraction of large droplets with that of small droplets, the volume occupied by the larger ones is deduced.

From Brownian diffusivity D, the Stokes-Einstein relation yield the average droplet radius R

$$R = \frac{k_B T}{6\pi\eta D} \tag{7.4}$$

The validity of our analysis is supported by the remarkable agreement between the initial drop radius, R_0, determined by DWS shortly after emulsification, and the independent measurements obtained through microscopy observations for corresponding compositions (indicated by thick lines labeled as "microscopy" in figure 7.4).

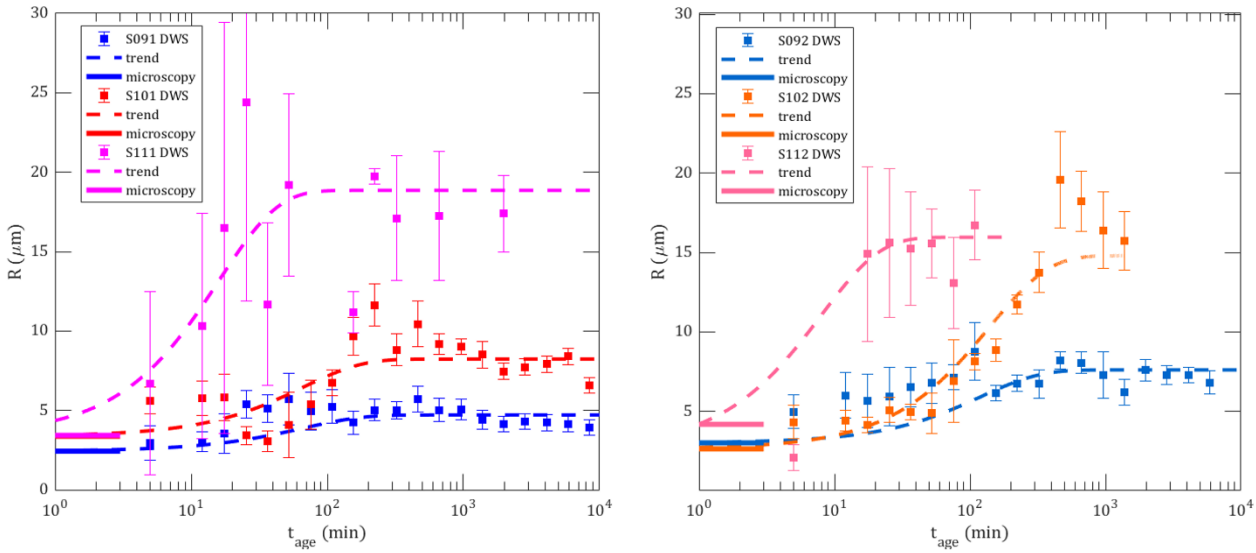

Figure 7.4 Hydrodynamic droplet radius as a function of emulsions aging, for the small droplets. DWS data (symbols) and phenomenological trends (dashed lines), compared with the corresponding initial values obtained by microscopy (horizontal lines at initial times). In the left panel are shown the samples SXX-1, with surfactant concentration $c = 10^{-5}M$ and in the right panel the samples SXX-2, with surfactant concentration $c = 4 \cdot 10^{-5}M$.

The photon transport length l^* typically shows growth with ageing (figure 7.5), although there are considerable uncertainties due to the limited size of the sample cell. For samples S091 and S101, an apparent asymptotic trend emerges as a function of age, prompting an attempt to fit a phenomenological power law of times to the data. In contrast, for the remaining samples, l^* rapidly saturates, in some case reaching values that exceed accurate measurement capabilities.

Regarding the ballistic velocity (figure 7.6), associated with coalescence events, a clear decreasing trend is observed as emulsions age. This trend holds true for all samples, although notable differences exist among them. Specifically, when comparing different samples, a faster decay of ballistic velocity in emulsions with higher oil content is observed while maintaining constant surfactant content. Moreover, in emulsions with lower surfactant content, at a constant oil content, the ballistic velocity generally decays faster, except for the case of S111, where it decays slower compared to S112.

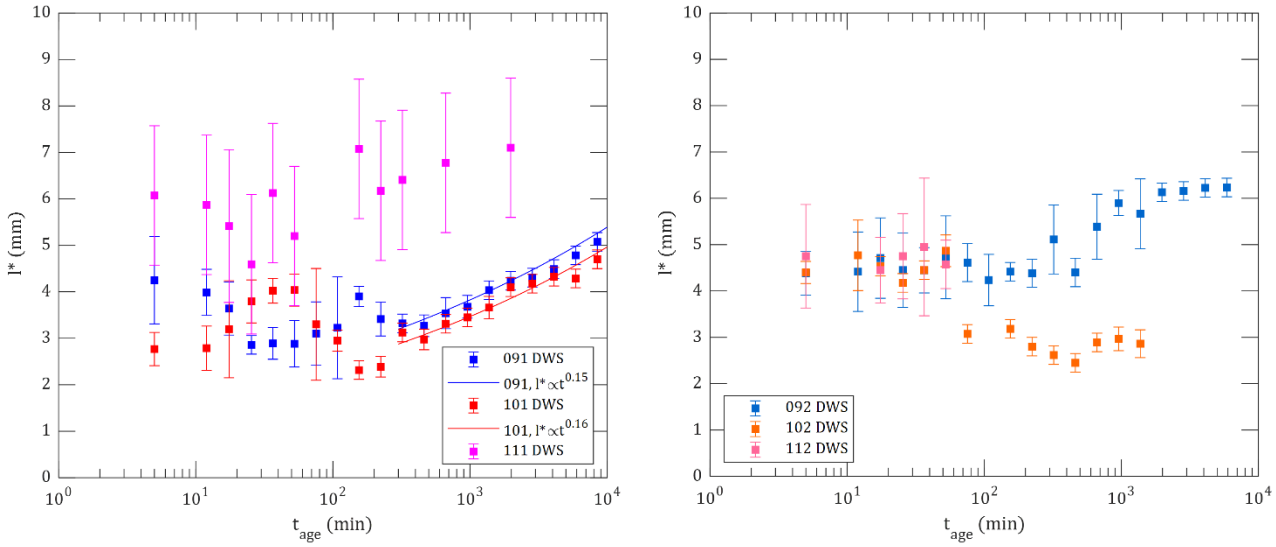

Figure 7.5 Mean photon transport length l^*, as a function of emulsion aging, for SXX-1 (left panel, surfactant concentration $10^{-5}M$) and SXX-2 (right panel, surfactant concentration $4 \cdot 10^{-5}M$)

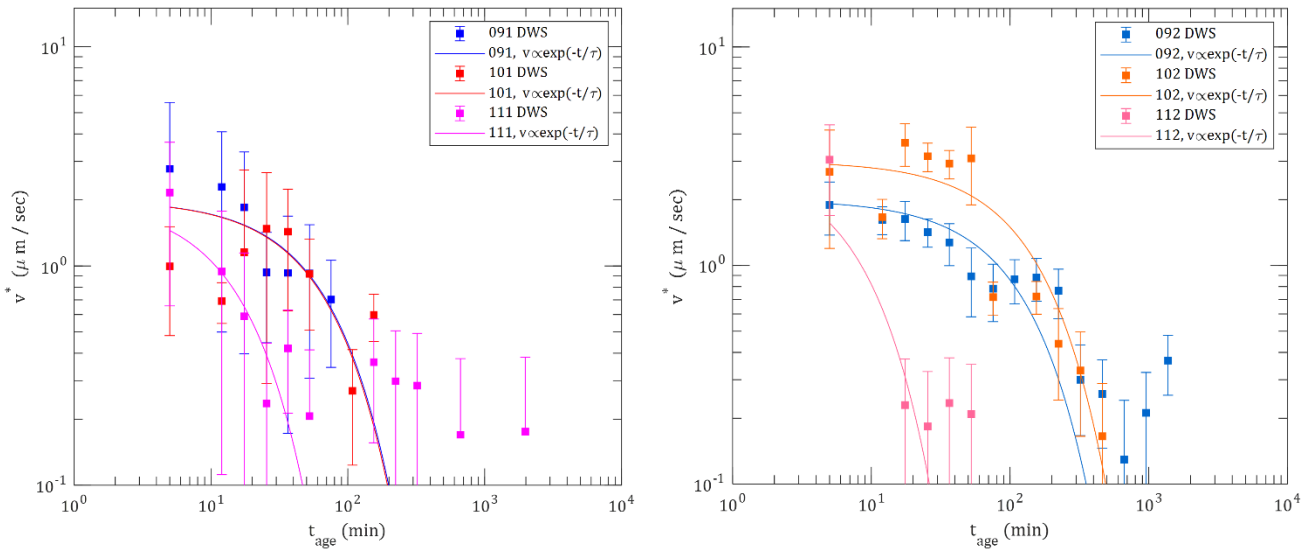

Figure 7.6 Ballistic velocities, as a function of emulsion aging, for SXX-1 (left, surfactant concentration $10^{-5}M$) and SXX-2 (right, surfactant concentration $4 \cdot 10^{-5}M$)

In the following discussion, it is important to recall that DWS correlation functions primarily provide insight into the dynamics of small drops. Then, the number density of small drops can be accurately quantified, and their movements can be characterized. However, the total volume of the larger drops can be deduced by subtracting the volume occupied by the small drops from the initial oil content of the emulsion.

In case of binary mixtures of small and large particles, it can be hypothesized under reasonable assumptions, that the DWS results from the ensemble can be described by an effective mean transport length l^*_{eff} and an effective relaxation time τ_{eff}. Using subscripts A and B to denote quantities corresponding to the small and large drops, it can be observed that

$$l^*_{eff}{}^{-1} = l^{*-1}_A + l^{*-1}_B \tag{7.5}$$

where l^*_X (X=A or B) are the transport lengths of an hypothetical dispersion of the component A (or B) alone in the same medium. Note that l^*_X depends on the volume fraction ϕ_X of each component, and of course on its mean radius R_X. At first approximation, within Mie theory, and for non-interacting spheres, for each component X we have

$$l^*_X \propto \frac{R_X}{\phi_X} \tag{7.6}$$

while the effective relaxation time is given by:

$$\tau^{-1}_{eff} = \frac{l^*_{eff}}{l^*_A}\tau^{-1}_A + \frac{l^*_{eff}}{l^*_B}\tau^{-1}_B \tag{7.7}$$

It is thus evident that the dynamics probed by DWS is mostly dominated by the component with the shortest transport length, which, for reasonable values of volume fractions, can be safely identified with the population of smallest drops, while any populations with R larger than a few tens of microns contributes only marginally to the DWS signal.

The occurrence of Ostwald ripening is unlikely in the present case due to the extremely low solubility of the dispersed MCT oil phase (< 0.001 g/l, http://www.uspbpep.com/ep60/triglycerides%20medium-chain%200868e.pdf) in the continuous aqueous phase. Additionally, the relatively large mean drop size would result in negligible growth rates, further ruling out Ostwald ripening. However, drop-drop reversible aggregation and irreversible coalescence processes remain viable possibilities. And if DWS is mostly sensitive to the population of smaller drops, for which it yields information on the coalescence rate, it appears reasonable to attribute the coalescence rate to events involving small droplets

Recalling the observation by microscopy that the initial drop size distribution is bidisperse [80], three types of aggregation/coalescence processes may occur:

1. Between two small drops.
2. Between one small and one large drop.
3. Between two large drops.

Among these, only types 1. and 2. have an impact on the population of small drops. Generally, it is expected that if emulsion ageing is primarily driven by type 1. events, the mean radius will grow over time. In contrast, type 2. events will only affect the photon transport length l^*, which is proportional to the number density of small drops.

For type 1. events, the specific law governing the growth of drop radius can provide valuable insights into the type of drop-drop interaction, helping to distinguish between reversible aggregation and irreversible coalescence.

The growth pattern directly reveals the kinetics of the primary mechanism driving emulsion ageing. Drop coalescence, a second-order process, leads to exponential growth in the drop size. On the other hand, drop-drop aggregation is generally considered an intermediate process.

In all the samples the mean drop radius grows steadily with time up to a critical time τ which is different for each sample. In the same time interval, the value of l^* shows no appreciable trend, while the average ballistic

velocity decreases with time. After τ , the mean radius does not increase anymore, while l^* starts to increase, and the ballistic velocity becomes vanishingly small.

This scenario can be rationalized assuming that initially most of the surfactant is adsorbed at the droplet interfaces and the small droplets, in their rapid motion, collide with high probability with another small droplets (type 1 events), and as a result they either coalesce or they aggregate, forming aggregates with radii increasingly larger, still in the range of tens microns. In this process, surfactant is released from interfaces, providing increasingly effective stabilization to the remainder of the population. After critical time τ, the surfactant coverage of the small droplets inhibits further frequent coalescence, hence negligible ballistic motion is observed, and at the same time, rare coalescence events of type 2 effectively reduce the drop number density, which causes the growth of l^*.

The evolution of the mean drop radius can be phenomenologically described by an offset and a saturating exponential:

$$R(t) = R_0 e^{-t/\tau} + R_\infty \left(1 - e^{-t/\tau}\right) \tag{7.8}$$

In which only the long-time asymptotic value R_∞ is determined by fitting, while the initial value R_0 is fixed to the initial radius for the small drops determined by microscopy, and the characteristic time is assumed to be the same as for the decay of the ballistic velocities, under the implicit assumption that the ballistic velocity and the growth of radius are related, both being due to coalescence events.

Sample	**Oil content**	$\boldsymbol{R_0}$ $\boldsymbol{(\mu m)}$	$\boldsymbol{R_\infty}$ $\boldsymbol{(\mu m)}$	$\boldsymbol{\tau}$ $\boldsymbol{(min)}$
S091	20%	2.4	4.7 ± 0.2	$66' \pm 30'$
S092	20%	3.0	7.2 ± 0.2	$120' \pm 50'$
S101	30%	3.4	8.3 ± 0.5	$66' \pm 30'$
S102	30%	2.7	17.5 ± 1.3	$140' \pm 60'$
S111	50%	3.4	19 ± 1	$16' \pm 6'$
S112	50%	4.2	16 ± 2	$8' \pm 8'$

Table 4 The table shows the observed value of radius saturation value R_∞, radius initial value R_0 and the characteristic time τ.

Analysing in detail the dependence of τ and R_∞ on surfactant content, whose values are reported in table 4. For the series 09X and 10X, τ increases with increasing surfactant content, while R_∞ grows. This is a natural consequence of higher coalescence rate for those sample with less surfactant content. Samples 11X show instead a comparable characteristic time.

The saturation value, R_∞, is observed to increase with higher oil content for a given surfactant content (S111 being larger than S101 and S091, and S112 being larger than S102 and S092). This relationship can be easily understood: an increase in oil content leads to more droplets and, consequently, less surfactant coverage per droplet. This explains why S111 practically de-emulsifies in just a few minutes due to its high oil content.

However, what is particularly surprising is that the final value of drop radius is larger for higher surfactant content (SXX-2 being larger than SXX-1). This observation suggests an anomaly in interfacial properties at surfactant concentration $c = 4 \cdot 10^{-5} M$. It is possible that the increased surfactant concentration from $10^{-5} M$

to $4 \cdot 10^{-5} M$ leads to alterations in the interfacial properties, affecting the droplet coalescence or aggregation dynamics and resulting in a larger final drop sizes.

Now let's shift attention to the ballistic velocity, which is linked to coalescence events, as described in the mechanism above. After emulsification, there is an immediate cascade of coalescence events, which decays over time, presumably reaching a steady state where coalescence events become infrequent and no longer distinguishable. To model phenomenologically this phenomenon is used an exponential decay, with an arbitrarily fixed initial amplitude, yielding the following results (Table 6):

Sample	Initial v_0 $(\mu m/s)$	Decay time τ (min)
S091	2	$66' \pm 30'$
S092	2	$120' \pm 50'$
S101	2	$66' \pm 30'$
S102	3	$140' \pm 60'$
S111	2	$16' \pm 6'$
S112	3	$8' \pm 8'$

Table 6. Initial ballistic velocity v_0 at early ageing time ($t_{age} = 5'$), characteristic decay time τ of $v(t)$. The ballistic velocity as function of aging time is phenomenologically modelled with a single exponential decay $v(t) \propto v_0 \cdot \exp\left(-\frac{t}{\tau}\right)$.

Emulsions containing 50% oil content demonstrate a remarkably faster decay compared to the others, surpassing the decay rate by at least an order of magnitude. This noteworthy effect is likely attributed to two concomitant phenomena, both stemming from the substantial oil fraction resulting in a high number density of drops:

- The frequency of drop-drop collisions increases significantly.
- The interfacial coverage decreases, making coalescence more probable, rather than reversible aggregation.

In emulsions with lower oil content (20% and 30%), the ballistic velocity is initially nearly independent of surfactant content. However, as time progresses, the decay in samples with lower surfactant content accelerates, presumably due to a higher frequency of coalescence events.

The photon transport length l^* carries valuable information about both the number density of drops and their scattering properties. In a simple model featuring uniform drop sizes, l^* would be directly correlated to the mean drop size and oil volume fraction. However, the observed scenario diverges from this, as the drop size distribution, through AUTH microscopy, reveals a bimodal nature. Additionally, considering some level of polydispersity, the Mie scattering efficiency of the drops does not exhibit significant size dependence. Under this assumption, the evolution of l^* becomes solely tied to the number density of smaller droplets $\rho \propto \frac{1}{l^* \sigma_{sca}}$.

$$\rho = \frac{1}{l^* q_{sca} \pi R^2 (1 - < cos\theta >)} \tag{7.9}$$

Where q_{sca} and $\langle cos\theta \rangle$ are respectively the Mie scattering efficiency and asymmetry parameters. Consequently, the changes in l^* become a potent indicator of type 2. coalescence events, which primarily lead to a reduction in the number density of small drops.

However, the observed values of l^* are notably large, often exceeding half of the sample cell's size, which indicates a low drop density and poses limitations on the accuracy of calculations. The results are presented, taking into consideration that for samples S111 and S112, l^* is of significant magnitude, making it challenging to obtain reliable data.

A meaningful comparison can be made between the time evolution of the mean drop radius and the decay of ballistic velocity. As depicted in the figures 7.4 and 7.6, they exhibit a similar trend at early times, supporting our interpretation that ballistic motion is linked to type 1. coalescence events involving small drops, at least up to ages of 60-100 minutes.

Interestingly, the time evolution of l^* is dissimilar to that of the radii, it is found to remain constant -within the experimental uncertainty- on the same time scale in which the mean radius grows. This would be an obvious contradiction in a monodisperse sample. The growth of the radius, together with mass conservation, would imply a reduction of number density of drops, and a growth of l^*. On the contrary, in a polydisperse sample this may happen.

On the other hand, the scenario is quite different for the diluted emulsions with low surfactant content, S091 and S101, especially at later stages (from 300 minutes onwards). In these cases, the mean drop radius does not increase significantly, remaining roughly constant, while l^* steadily increases following a power-law trend $l^*(t) \propto l^* t^{\alpha}$ with an exponent $\alpha \sim 1/6$. This indicates a decrease in the number density of small drops without a considerable increase in their mean size, implying that emulsion aging in this context primarily occurs through interactions between small drops and larger ones. This behavior aligns with the characteristics of an emulsion in the late stage of de-emulsification.

One observation is a slight decrease in the mean radius in this last case. To ensure there is no other influencing factor, it would be prudent to repeat the experiment for a double check. Another interesting observation is that the number density can be converted to the fraction of oil by considering the mean drop radius and the oil content of each emulsion. The general outcome, as shown in figure 7.7, reveals that approximately 10% of the oil volume in all emulsions is contained within the small droplets, the rest being obviously associated with the formation of larger droplets. This finding supports qualitative microscopy observations, which indicate that only about 1% of the oil volume is involved in the formation of small droplets.

It is worth noting that the traditional approach to DWS analysis would prove entirely impractical for samples characterized by large values of l^*. In such cases, only the Monte Carlo approach, although with certain significant limitations, could potentially yield viable results.

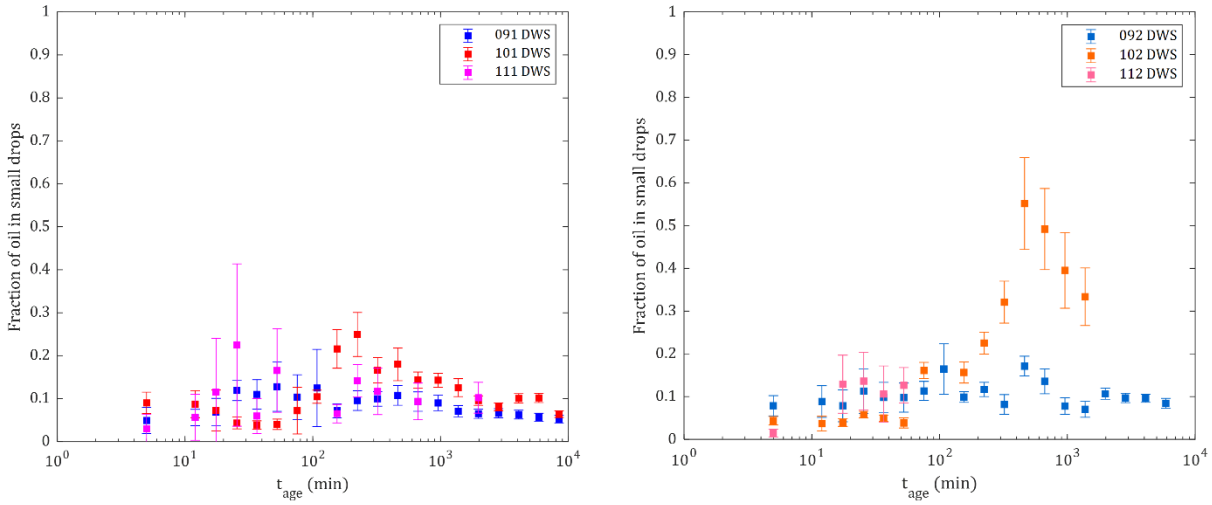

Figure 7.7 Fraction of oil in small droplets as a function of emulsions aging. On the left the surfactant concentration in solution is $10^{-5}M$, while on the right $4 \cdot 10^{-5}M$. Roughly 10% of the oil volume in all emulsions is found within the small droplets, with the majority being clearly associated with the formation of larger droplets.

By detailed analysis of mean drop radius, of the type of dynamics (Brownian vs ballistic) and by measuring the light transport length l^* it is possible to identify different de-emulsification mechanisms. This mechanisms occurs mainly via interaction between small droplets (type 1.) in most cases, but also via interaction between small and large droplets, particularly at late stage of de-emulsification.

7.2 Multi-speckle analysis

This technique presents a multi-speckle time-resolved approach to Dynamic Light Scattering. Its primary purpose is to characterize the duration of rearrangement events and the speed of droplet motion during such events by measuring the temporal correlation, $g_2(\tau, t)$, of the speckle pattern at a specific time lag τ versus time t. Essentially, g_2 is the correlation function of pairs of images captured by a CCD camera. To gain insights into the size of events, adjustments in illumination/detection spots can be made. However, it is important to note that only the backscattering geometry in Time-Resolved Correlation experiments allows for resolving individual rearrangement events. In contrast, transmission experiments result in the superposition of signals from numerous individual events, making the analysis more challenging.

The multi-speckle approach offers the advantage of simultaneous detection of multiple points; however, the acquisition time is constrained by the exposure time. Ensuring uniform illumination on the sample is crucial to prevent any deviations from the baseline, maintaining it close to unity. Additionally, the dimensions of the speckles should be comparable to the size of the detection channel to optimize the signal-to-noise ratio and prevent a decrease in the contrast of the correlation function. To achieve accurate analysis, it is essential to identify proper time and frequency intervals. These intervals are limited by the time window within which the autocorrelation function evolves.

The data is collected sequentially from the line camera and stored as 2D images. The acquisition frequency sets the time distance between consecutive lines. Multiple time lags are employed for the same data set, and the results are compared. To avoid normalization and mitigate speckle/detector size effects, the key quantity

of interest is the degree of correlation between pairs of images captured at a time lag τ, represented by the function:

$$g_2(t,\tau) = \frac{\langle I(t)I(t+\tau)\rangle_s}{\langle I(t)^2\rangle_s} \tag{7.10}$$

Where $I(t)$ is the intensity measured at time t for the s-th CCD pixel, and $\langle \dots \rangle_s$ denotes averaging over the pixels. It is essential to ensure that the time lag τ is considerably shorter than the duration of rearrangement events.

The computation proceeds as follows: the current line and the line at a distance t are processed using the equation (7.10). This process is repeated for different values of τ (multi-τ autocorrelation) on the same data set and starting line. The outcome consists of several plots, each depicting the autocorrelation as a function of time, corresponding to different values of τ. This comprehensive analysis allows for a detailed examination of the temporal dynamics of the system under investigation.

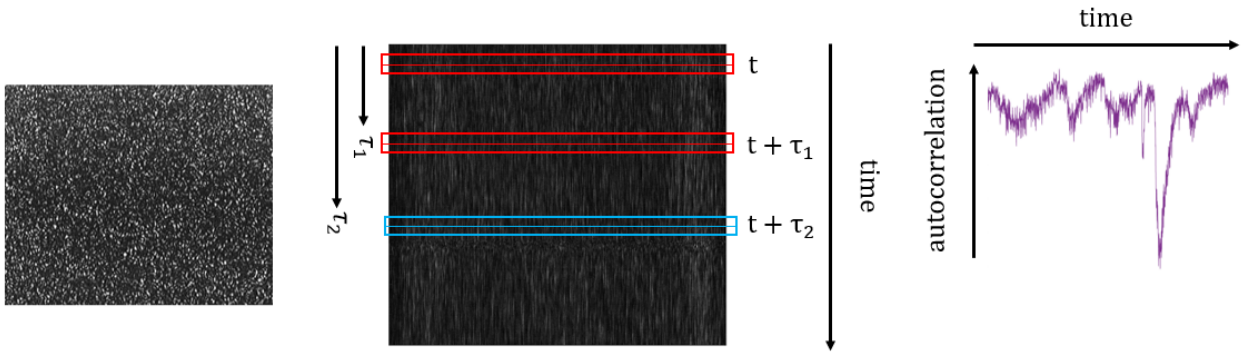

Figure 7.8 A speckle pattern is generated on the camera optical plain, and a single line is acquired from line camera detector. Single lines are collected into 2D images incrementally and set the of data is processed with a fixed lag time τ. Several τ are used to produce the autocorrelation function at each lag time as a function of time.

The data processed by the line camera allows access to correlation functions at non-standard lag times. The selection of correlation times varies for each sample and its aging, and this difference is particularly evident between gravity and microgravity conditions. The presence of creaming in the emulsions studied on the ground needs distinct correlation times compared to the microgravity environment.
The figure 7.9 illustrates the creaming phenomenon of the emulsion observed on the ground, where gravity drives the phase separation due to the difference in density between water and oil. Additionally, intermittent events, depicted as dark spikes in the g_2 plot as a function of aging time, can be observed. These events indicate rapid accelerations in the decay of the correlation function.

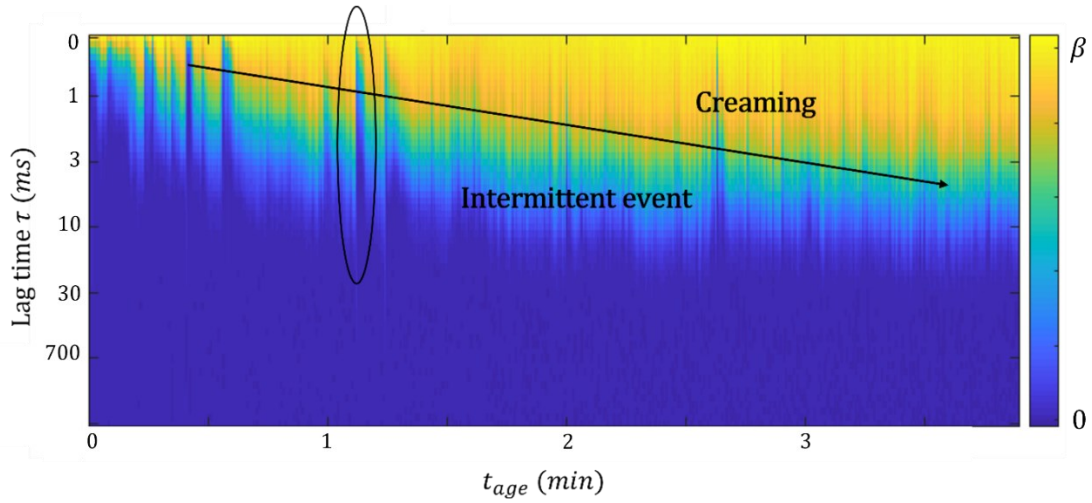

Figure 7.9 Time resolved $g_2(t_{age})$ for freshly prepared emulsion with a 50:50 oil/water ratio and 10^{-5} M surfactant (sample S 11-1) content at different lag times τ (ms).

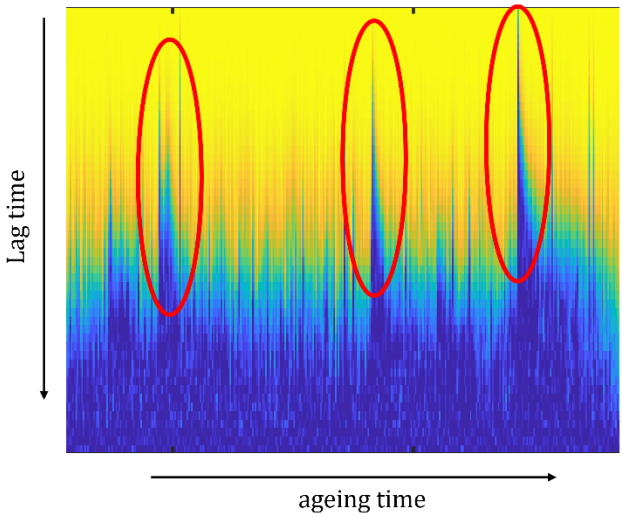

Figure 7.10 Examples of Time resolved $g_2(t_{age})$ at different lag times τ (ms) from the elaboration of the SMD line camera data, at the early stage of the aging sample 11-1: oil/water ratio 50:50; surfactant (C12EO21) concentration $10^{-5}M$ in water. Transient events, depicted as dark spikes in the g_2 plot as a function of aging time, can be observed. These events indicate rapid accelerations in the decay of the correlation function.

7.2.1 Frequency of transient and intermittent event

Concentrate emulsions undergo complex structural changes during aging, and understanding the dynamics of intermittent events is crucial in this context. In this study, time-resolved analysis of line camera BS signals is employed to explore the frequency and nature of intermittent events in emulsions as aging proceeds. The frequency of these transients in the early stages of aging is monitored as an indicator of the structural evolution of the emulsions. The rate of intermittent events is observed to decrease steadily with aging, reflecting the evolution of the emulsion's structure over time. However, the presence of spikes indicates abrupt accelerations in the aging process, highlighting the significance of these events in the overall aging dynamics. Detailed

analysis of these spikes enables the identification of avalanche phenomena, characterized by bursts of coalescence events. These avalanche features involve a drastic change in the emulsion's structure, followed by a relaxation process occurring over a fraction of a second. Our findings suggest a superposition of ballistic dynamics and diffusive (Brownian) dynamics, providing a comprehensive framework for understanding these intermittent events during aging.

The figure 7.11 illustrates the number of individuated and counted transients in various samples on board, as a function of the ageing time of the emulsion. The four panels represent different concentrations of surfactant, ranging from the lowest in the top left to the highest in the lower right.

Within each panel, three distinct datasets are presented, each with its specific water-oil concentration (S09-X 20:80 o/w, S10-X 30:70 o/w, and S11-X 50:50 o/w). Notably, there is a rapid decrease in the number of transients across all surfactant concentrations, indicating that most events occur during the initial hour from emulsification. In samples with a surfactant concentration of $10^{-5}\ M$, there are more such events. However, as expected, events become increasingly rare with higher surfactant concentrations, reflecting the enhanced stability provided by a higher concentration of surfactant in the emulsion.

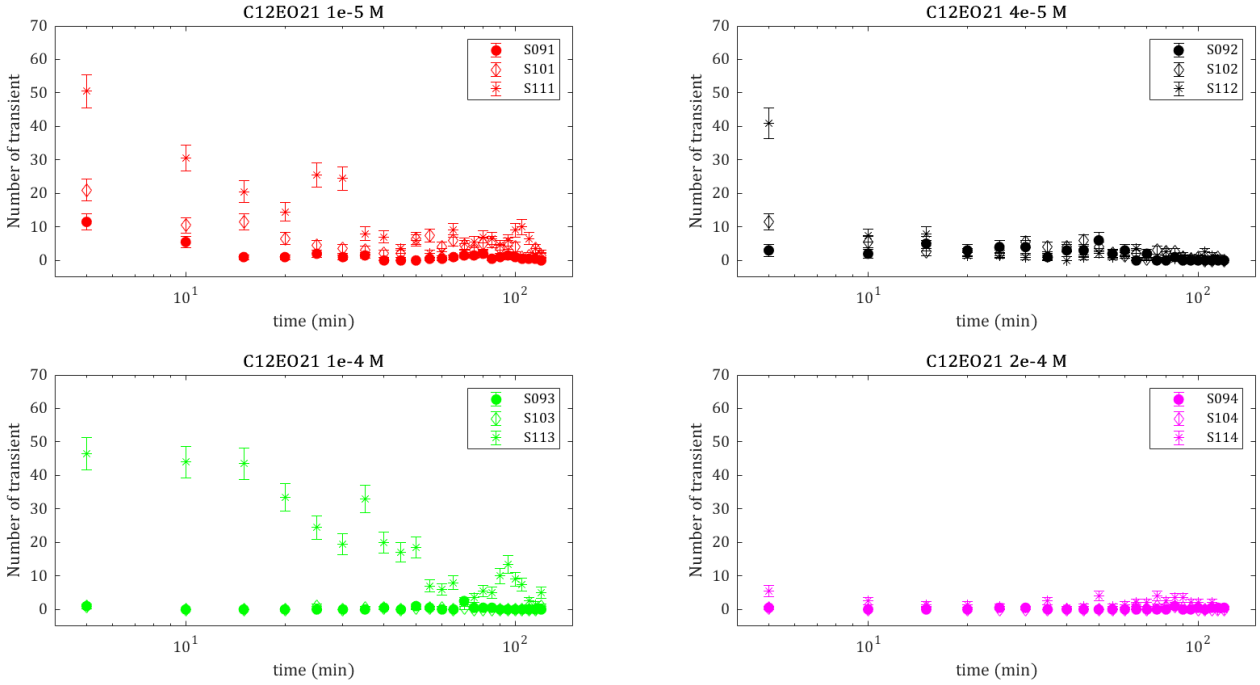

Figure 7.11 The figure presents the frequency of transients as a function of surfactant concentration and ageing time. Starting from the top left panel, emulsions contain C12EO21 in quantities of $1 \cdot 10^{-5}\ M$. *Immediately to the right are emulsions with a surfactant content of* $4 \cdot 10^{-5} M$. *Moving to the lower left panel, the surfactant content increases to* $1 \cdot 10^{-4} M$, *and finally, the bottom right panel shows emulsions formed with* $2 \cdot 10^{-4} M$ *of C12EO21 in aqueous solution.*

Interestingly, the occurrence of intermittent events shows a direct correlation with the oil content in water. As the oil content increases, the number of intermittent events also rises. Another noteworthy observation is the decreasing trend in the number of transients as the emulsion ages.

For emulsions with lower oil content, the rapid decrease in transients occurs within the first 20 minutes after emulsification. However, as the oil content in water increases, this decrease is delayed and happens after about an hour. Beyond the initial hour of measurement acquisition, events become sporadic and sometimes

negligible, particularly in samples where the de-emulsification process is rapid. Such occurrences are common in samples that exhibit numerous events in the initial minutes after emulsification, often showing a "cascade" effect (e.g., S091, S101, S111), or in samples known for their exceptional stability, such as S114.

The general trend in all samples aligns with an exponential decay, except for sample S113, which exhibits a delay of approximately 20 minutes. This anomaly can potentially be explained by the concurrent influence of two distinct factors:

- Reduction in the number of droplets. This factor is expected to decrease the occurrence of transient events.
- Adsorption Effect: initially, the concentration of surfactant in the water phase is insufficient to induce Marangoni-like forces. However, as coalescence progresses, resulting in a reduction in interfacial area, the surfactant concentration gradually increases. This evolution leads to a phase in the isotherm where the release of surfactant starts affecting interfacial tension, resulting in Marangoni-like behaviour.

To summarize: Figure 7.12 shows the number of transients as a function of the aging time of the emulsion, focusing on the samples with less surfactant (10^{-5} M and $4 \cdot 10^{-5} M$). In general, the lower concentrations of surfactant 10^{-5} M (in red) show more events in relation to the samples with more oil, 30% compared to 20%. Therefore, less surfactant increases the probability of transient events, and the same effect occurs in samples with more oil (S111 and S112, 50% o/w). In the context of the recent figure, it emphasizes a decreasing trend in the number of events over time, aligning with the ballistic velocities observed through DWS analysis. The velocities exhibit a faster decrease for those same samples characterized by a higher number of events in the early stages after the emulsification process.

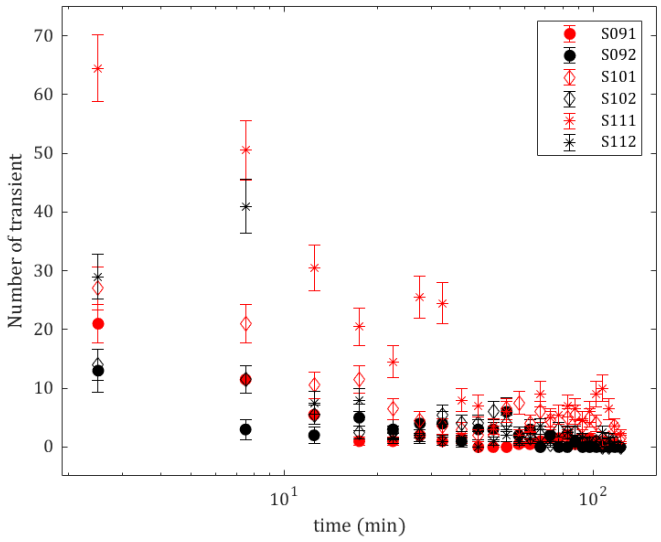

Figure 7.12 Transient frequency as a function of ageing time. From red to black increases the concentration of surfactant, while the dots represent the fraction of oil in water lower (20%), which increases with squares (30%) up to asterisks (50%)

7.2.3 Time-resolved dynamics: Ballistic bursts

In this section, the analysis of transient events is based on the multi-speckle technique, in which, as explained in chapter 6.3, it is possible to analyze the correlation functions resolved over time $g_2(\tau, t)$.

Beginning a thorough analysis means firstly identifying significant transient events. These events are extracted while filtering out instances in which accelerometer oscillations exceed a predefined threshold. This selective process is facilitated by the microgravity measurement assembly (MMA) incorporated on board the ISS.

Subsequently, the acquisition using the line camera reveals the speckle dance pattern within the sample. The presented figure 7.13 displays a temporal image plotted against pixels around a specific transient event. It's important to observe that a τ_{start} point can be identified (as indicated by the red arrow in figure 7.13). This temporal marker is defined as the time when the transient event begins, followed by a substantial change in the speckle configuration to indicate an acceleration in the correlation function. Then, the multi-τ correlation function is computed from τ_{start} according to equation (7.7). This function quantifies the correlation between pairs of images captured in a lag time interval. Different correlation functions with high temporal resolution are obtained, revealing the sample's evolution during the transient event. Thus, the initial correlation function calculated at τ_{start} exhibits a slow decay, rapidly transitioning to a faster and compressed profile, an explicit indication of acceleration, before getting back to its original shape.

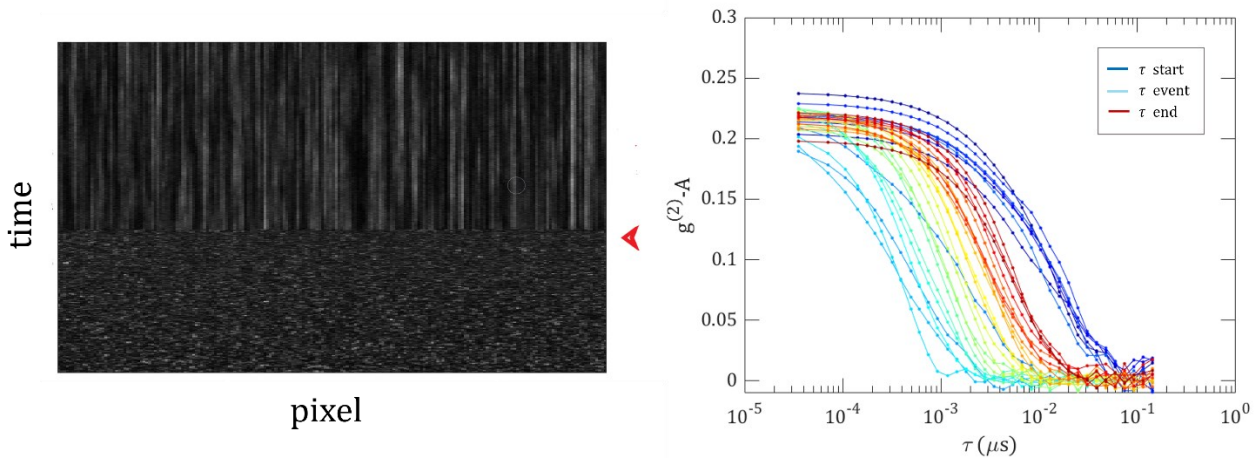

Figure 7.13 Image from the elaborated line camera data of time against pixel. Series of normalized correlation functions $g_2(\tau)$ during the temporal evolution of transient event. The time resolved correlation function in blue is computed at the beginning of the event τ_{start}, then in light blue is the correlation function computed during the event at τ_{event}. The colour scale of the correlation functions continues with green, yellow, and orange to finish with red when the event is over at τ_{end}.

After obtaining the time resolved correlation functions from the backscattering images captured by the line camera, the $g_1(t)$ function is inverted to derive the mean square displacement $\langle \Delta r^2(t) \rangle$ from equation (3.6).

The form of $g_1(t) = \exp\left(-\frac{1s}{3l^*} k_0^2 \langle \Delta r^2(t) \rangle\right)$ is governed by both the mean square displacement (MSD) and the mean free path of transport l^*. It is important to determine the value of l^* to accurately deduce the MSD through the inversion of g_1. To achieve this, the pre-established values of l^* that are retrieved from the concurrent fitting of correlation functions in transmission and backscattering from DWS. These values were earlier computed using the model detailed in the preceding chapter 3.

Subsequently, it is possible to attempt a fitting procedure on MSD utilizing a generalized diffusion model.

$$\langle \Delta r^2(t) \rangle = 6Dt^{\alpha} \tag{7.11}$$

Across almost all samples, many remarkable events are present, especially in the minutes immediately following the emulsification. In stationary dynamics, dominated by normal diffusion, the mean square displacement (MSD) grows linearly in time, with a value of $\alpha = 1$, while during transient phases this power coefficient undergoes rapid growth, signifying a transition towards super diffusive dynamics. The trends of α during typical transient events are shown in (figure 7.14).

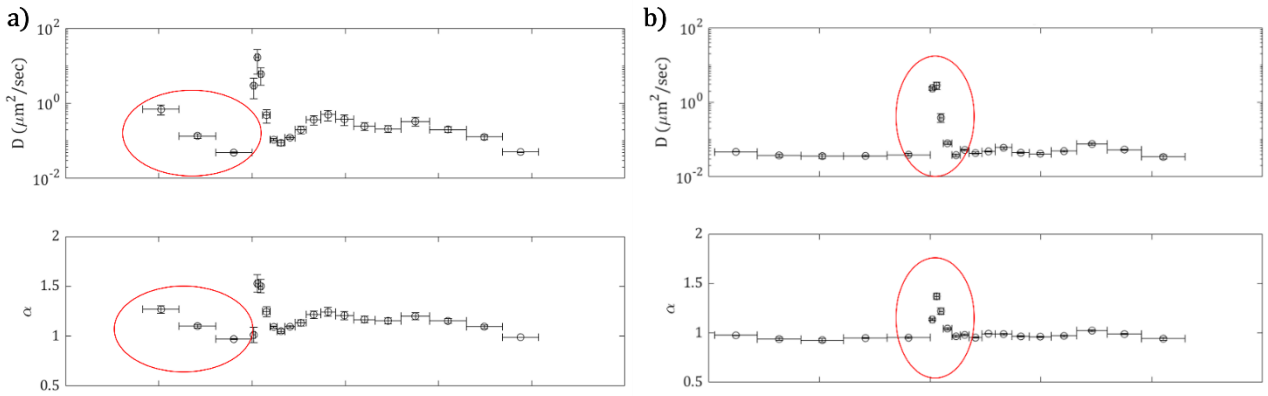

Figure 7.14 ***a)*** *α and D trend for the sample 09-1 (20:80 o/w, $10^{-5}M$) immediately after emulsification at about 4 minutes aging time. The residues of the emulsification process are observable both in the coefficient of anomalous diffusion D and in the fitting parameter α, circled in red.* ***b)*** *α and D trend during the transient event for the sample 09-1 (20:80 o/w, $10^{-5}M$) at about 20 minutes from emulsification. The transient event is circled in red and can be identified by a peak and a subsequent relaxation of the anomalous diffusion parameters D and α.*

A further step forward in the analysis of transient events from backscattering data acquired and processed by line camera consists in analysing the time-resolved correlation functions through our ad hoc analysis, already explained in previous chapters.

By simultaneously fitting the correlation function derived from backscattering data elaborated by the line camera and the correlation functions obtained through transmission data processed by the Corrtector, this enables an in-depth exploration of transient events. Furthermore, when examining Brownian dynamics in this context, in addition to the previously determined fit, it is possible to incorporate a ballistic velocity component.

$$\langle \Delta r^2(t) \rangle \sim \left((6Dt + (vt)^2) \right) \tag{7.12}$$

$$\left((6Dt + (vt)^2) \right) \rightarrow \left(\frac{t}{\tau_B} + \left(\frac{t}{\tau_S} \right)^2 \right) \tag{7.13}$$

Initially, during the analysis of DWS correlation functions, the coexistence of a Brownian dynamic is observed alongside an average ballistic velocity of displacements from scattering centres. However, in the investigation of correlation functions time-resolved by the line camera, the exact speed at which the transient event occurs can be extracted.

The graphs below show Brownian τ_B and shear τ_S relaxation times. The time τ_B is established through the preceding fit involving solely the DWS correlation function, while the presence of τ_S signifies an acceleration of the correlation function precisely at the onset of the transient event. In turn, the ballistic speed is derived, exhibiting its influence exclusively within the transient event, both before and after $v^* = 0$, with its peak value occurring during the event itself.

In figure 7.15 the presence of shear time or ballistic velocity, due to emulsification is still noticeable when the event takes place shortly after emulsification, as shown in panel a). In panel b), the same sample exhibits an event occurring well after emulsification process. In this case, Brownian relaxation dominates, and ballistic velocity is zero before the event. When the event occurs, the velocity increases until $v^* \sim 8\ \mu m/sec$ and decreases progressively during the transient.

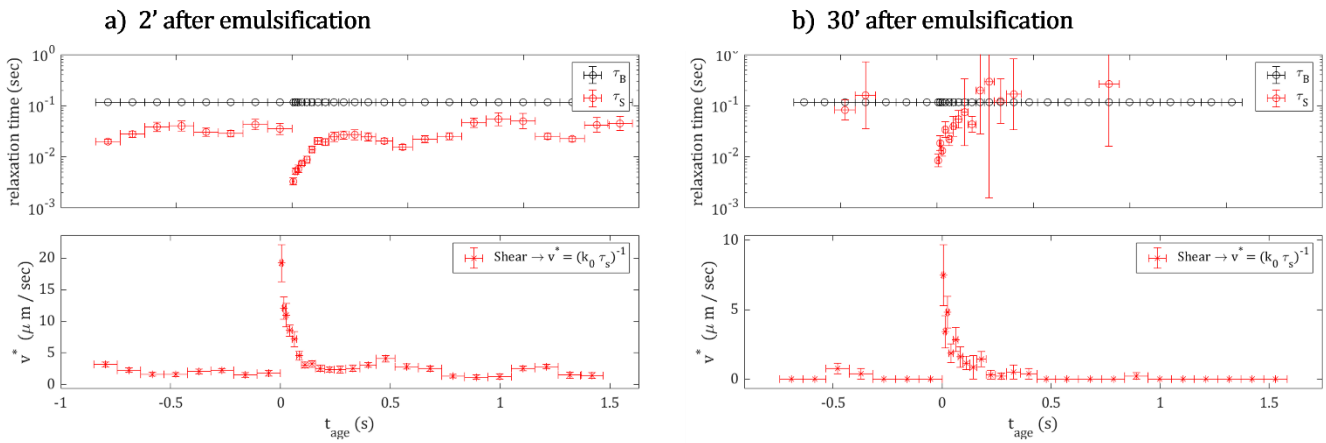

Figure 7.15 Trend of relaxation time, both Brownian time τ_B and shear time τ_s, on the top of a) and b) panels. Ballistic velocity on the bottom of a) and b) panels, during the transient event for sample 09-1 (20:80 o/w, $10^{-5}M$) shortly after emulsification (a) panel) and at aging time about 30 minutes from emulsification (b) panel)

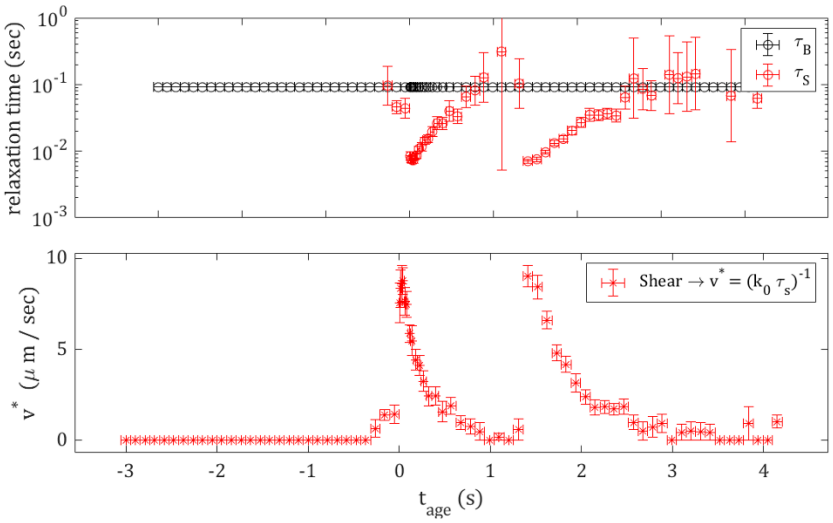

Figure 7.16 Trend of relaxation time, both Brownian time τ_B and shear time τ_s, on the top of the figure. Ballistic velocity on the bottom of the figure for sample 11-4 (50:50 o/w, $2 \cdot 10^{-4}M$). Example of double event.

In figure 7.17 a wide event is shown. Such events progress slowly and conclude within a matter of seconds. Large events are clearly visible in the time-resolved g_2 map, where the rapid colour change represents an abrupt acceleration of the correlation function. It is reflected in the trend of the relaxation time τ_s during the transient and consequently in the ballistic velocity.

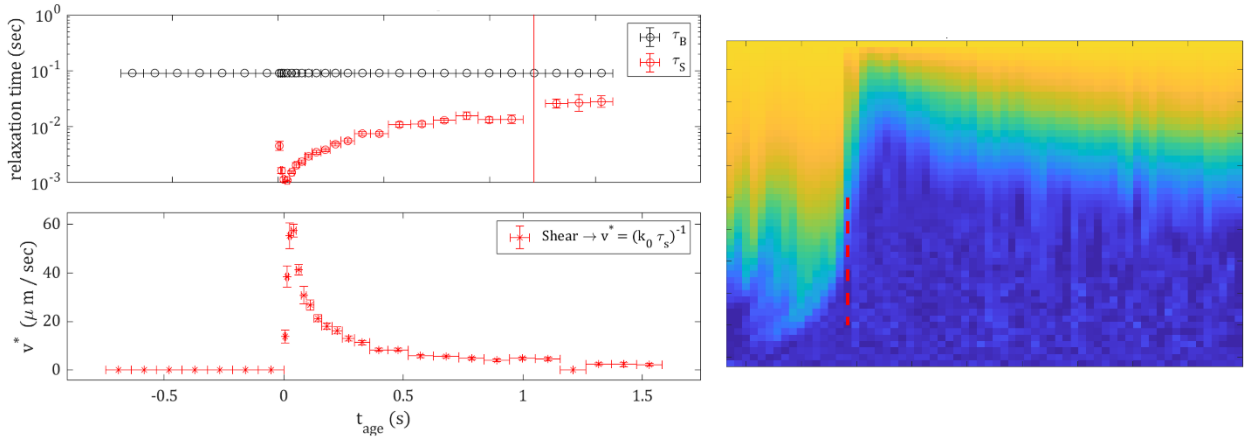

Figure 7.17 Trend of relaxation time, both Brownian time τ_B and shear time τ_s, is at the top of the figure. Ballistic velocity on the bottom of the figure for sample 10-1 (30:70 o/w, 10^{-5} M). On the right is a time-resolved $g_2(t_{age})$ where the intermittent events is depicted as dark spikes in the g_2 plot as a function of aging time. The event takes place about 70 minutes after emulsification, and it ends in 1.5 seconds.

Complementarily, figure 7.18 show a narrow event. These kinds of events end very quickly, in a tenth of seconds.

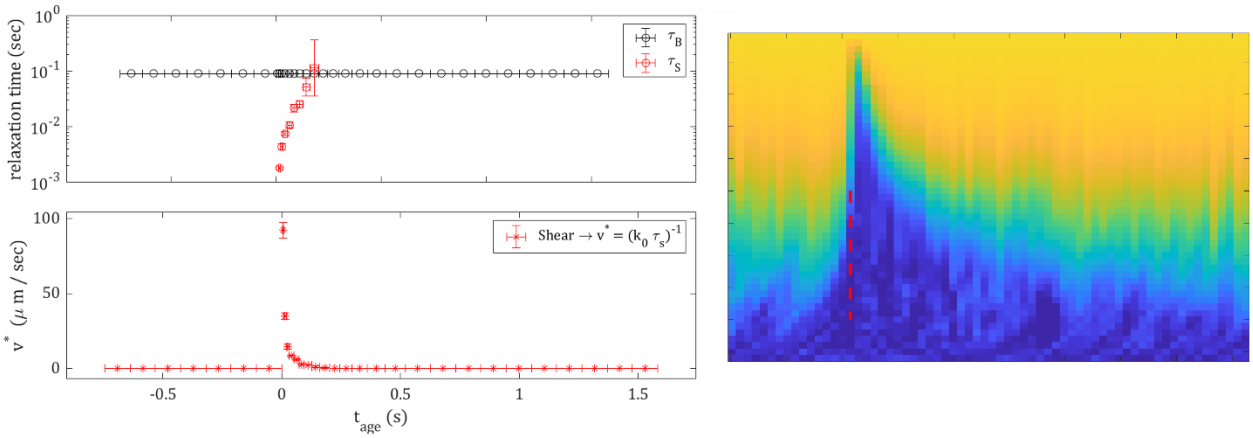

Figure 7.18 Trend of relaxation time, both Brownian time τ_B and shear time τ_s, is at the top of the figure. Ballistic velocity on the bottom of the figure for sample 10-1 (30:70 o/w, 10^{-5} M). On the right is a time-resolved $g_2(t_{age})$ where the intermittent events is depicted as dark spikes in the g_2 plot as a function of aging time. The event takes place about 90 minutes after emulsification, and it ends in a tenth of seconds.

Finally, it is possible to compare the extents of ballistic motions derived from the DWS analysis (chapter 7.1) with the resolved velocities obtained through multi-speckle analysis. The key distinction between these analyses lies in the temporal resolution used for calculating the correlation function. Consequently, the most logical approach is to integrate the ballistic velocities over the corresponding time intervals for each analysis. This integration yields a quantity known as “ballistic displacement”, which is inherently independent of the temporal resolution used in the analysis.

Table 7 below depict the ballistic displacement obtained from both the DWS analysis and the multi-speckle analysis (LC) at the initial stage of aging. Notably, it becomes evident that in the LC analysis, the displacement is consistently an order of magnitude lower than that observed in the DWS analysis. The observed difference arises due to the utilization of the DWS technique, which enables the concurrent examination of correlation functions in both backscattering and transmission, thereby allowing for a comprehensive assessment of the entire emulsion volume. In contrast, when employing the LC method, the investigation is limited to the scattering centres encountered by the light along its trajectory. While transmission DWS always probes the total volume of the cell, our Monte Carlo simulations show that, for l^* values around 4 mm typical of our samples, 63% of the scattering events occur in a volume approximately one third of the total cell volume. The total amount of ballistic displacement detected is given by the product of volumetric density of events, times the probed volume. This justifies qualitatively the different values found in transmission and backscattering, as reported in the following table.

Sample	Ballistic displacement from DWS (μm)	Ballistic displacement from LC (μm)
S091	89 ± 34	5 ± 2
S092	105 ± 23	12 ± 5
S101	37 ± 18	6 ± 11
S102	215 ± 30	11 ± 7
S111	25 ± 25	20 ± 17
S112	115 ± 15	50 ± 5

Table 7. Initial value of ballistic displacement for samples SXX-1 and SXX-2. On the right is the ballistic displacement obtained from multi-speckle analysis, while on the left is the same quantity obtained from DWS analysis.

7.3 Velocity distribution as a function of oil and surfactant content

The observation of transient events and their frequency, coupled with the subsequent analysis utilizing correlation functions from both DWS and line camera techniques through our approach, enables us to extract the ballistic velocities associated with these intermittent events. Given the large number of events observed in the multi-speckle analysis, velocity distributions can be derived for them. The analysis focuses on transient events of large intensity (defined as ballistic velocity larger than 5 μm/s and wide in time) observed in the initial two hours after emulsification.

The samples considered in the analysis below comprise those that exhibit a substantial number of events, allowing for the construction of a probability distribution function of velocity. These samples align with those previously examined in chapter 7.1, except for samples characterized by higher surfactant concentrations (SXX-3 and SXX-4). In most cases, these high-surfactant samples display minimal events, negligible velocities, and a high degree of stability. However, there are exceptions, notably samples S113 and S114, which contain a higher amount of oil (50% o/w) and a surfactant concentration of $10^{-4}M$. For these, important crowding effects complicate the dynamics, and the Mean Squared Displacement (MSD), fitted with an anomalous diffusion law (eq. 7.8), assumes a power coefficient $\alpha < 1$, indicative of a sub-diffusive behaviour.

The presence of confined motions within these samples, and their effect on emulsion stability will be the subject of future analysis.

Figure 7.19 represents the number of events as a function of the corresponding peak velocity (blue histograms). Overplotted, a phenomenological fit to a lognormal distribution with a mean velocity $\mu = \exp\left(m + \frac{\sigma^2}{2}\right)$ in a range of 17 to 180 $\mu m/s$; with m and σ respectively the mean and the standard deviation of the logarithmic values. This value of the mean velocity is dependent upon the quantity of oil or surfactant present in the sample. Samples with lower surfactant content display higher mean velocities compared to those with a higher concentration of surfactant. The same effect happens with increasing oil content. What is the source of this effect? Once more, a decrease in surfactant content and/or an increase in oil concentration leads to an increased probability of coalescence events and, subsequently, major rearrangement, resulting in higher peak velocities.

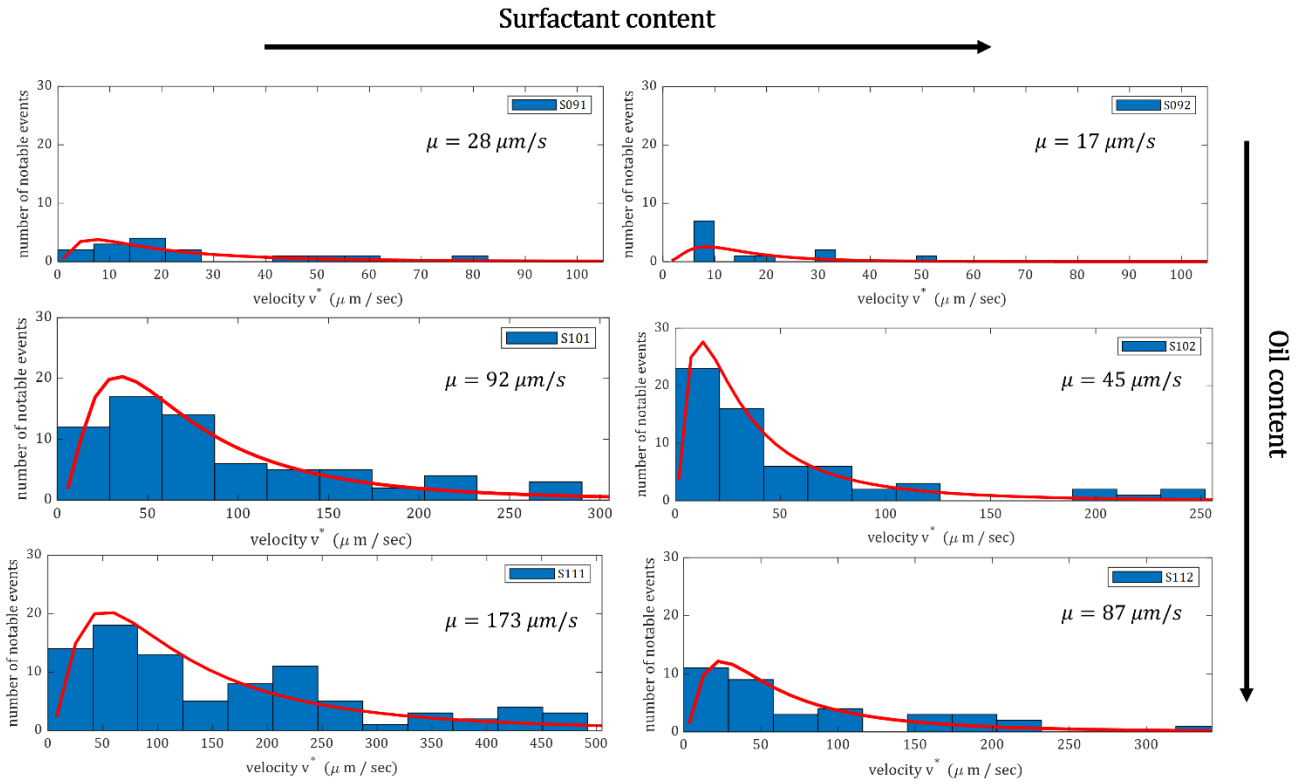

Figure 7.19 Velocity distribution in relation to the number of transient events observed in samples S091, S092, S101, S102, S111, S112. In the panel the amount of surfactant in the samples grows from $10^{-5}M$ to $4 \cdot 10^{-5}M$ going from left to right. Reading the data from top to bottom instead increases the amount of oil from 20 %, to 30% up to 50% or/w. Velocity histograms are obtained by collecting data for two hours of sample aging, after emulsification.

7.4 Comparison of droplet dynamics on ground and on board

The analysis presented in the preceding chapters can also be applied to the common scenarios on ground. The primary objective is to detect transient events, even in the presence of gravity, and to extract ballistic velocities over time while considering creaming effects. Furthermore, conducting this analysis on the ground enables to distinguish between creaming velocity and velocities associated with other destabilization phenomena. Another significant objective in conducting a ground analysis is to explore how the detection of these transient events is affected by the presence or absence of air, which, it is important to recall, was intentionally introduced in small quantities into the sample cell during the emulsion experiments to compensate overpressure limits

(chapter 5.1). This analysis aims to shed light on the potential variations in the velocities associated to transient events under different environmental conditions.

The sample investigated on the ground corresponds to the sample S11-4 on board (50:50 o/w, $2 \cdot 10^{-4}\ M$). This sample is particularly suitable for on-ground study due to its inherent stability, slower aging, and the greater volume available for examination, even after creaming-induced crowding effects.

The sample is prepared with nominally 0% air and 1% air inside. The figure 7.20 below, shows resolved ballistic velocities obtained through multi-speckle analysis for two notable transient events in sample with 0% air. Even after 4 minutes since the emulsification process, creaming remains evident in the emulsion, and the ballistic velocities never reach zero value during the transient event. Nevertheless, the presence of ballistic velocity attributed to the transient event is discernible. Upon the end of the creaming phase at the 7-minute mark of the aging process, the trend in ballistic velocity during the transient event closely mirrors the patterns observed in microgravity experiments. It exhibits a zero value before and after the event, with a peak velocity of 60 $\mu m/s$ coinciding with the event's onset.

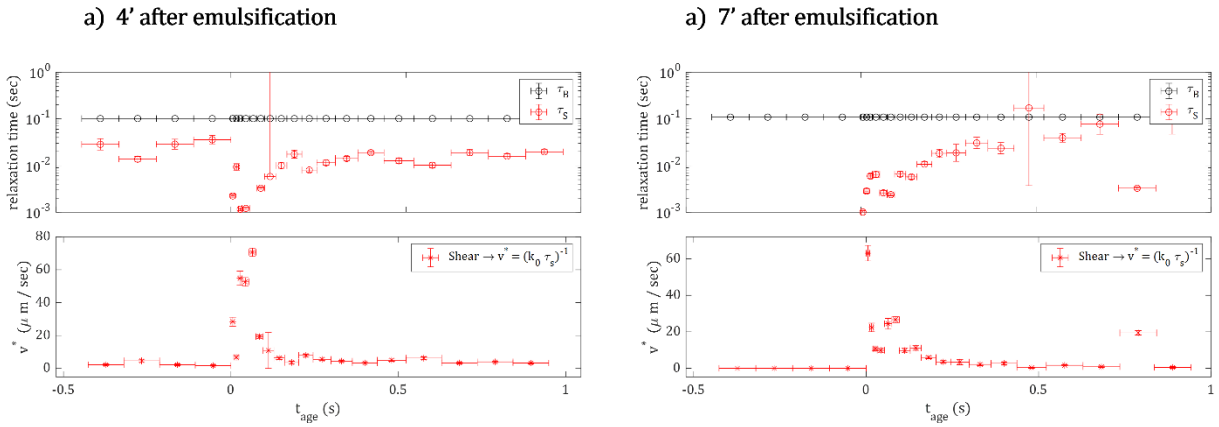

Figure 7.20 Trend of relaxation time, both Brownian time τ_B and shear time τ_s, on the top of a) and b) panels. Ballistic velocity on the bottom of a) and b) panels during a transient event observed from line camera. The sample, investigated on the ground, corresponds to sample S11-4 (50:50 o/w, $2 \cdot 10^{-4}$ M) on board. In this case, the sample nominally includes 0% air content. The sample is shown shortly after emulsification (a) panel) and at aging time about 7 minutes from emulsification (b) panel).

Sample	Number of events in 18 minutes
S114 gravity	13
S114 microgravity	29

Table 8 Number of events collected in 18 minutes of emulsion's aging for sample S114 (50:50 o/w $2 \cdot 10^{-4}M$) in gravity and microgravity environments.

Table 8 shows the number of transient events observed by LC and acquired during the first 18 minutes of emulsion aging, in microgravity and gravity environments for sample S114. It seems that in gravity more such events are visible, probably due to the presence of creaming related to motion of drops and bubbles, which is coupled in a dense system.

7.5 Towards the interpretation of DWS results: surfactant depletion and coverage

The reduction in surfactant concentration in the aqueous phase after emulsification is substantial, typically two orders of magnitude lower than the nominal concentration. The extent of depletion, represented by the matrix molar concentration after emulsification, depends on the initial concentration of surfactant in the matrix. As a result, the properties of the emulsions undergo significant changes, particularly in the initial portion of the isotherm that relates interfacial tension to surfactant concentration. A fascinating question that arises from this phenomenon is: What is the extent of surface coverage achieved by the surfactant molecules at the droplet interface?

To facilitate a meaningful comparison of the temporal evolution of the emulsions under study, it is important to consider the actual surfactant concentration within the emulsion matrix phase. This concentration can vary considerably from the nominal concentration of the solutions prior to dispersion/emulsification, primarily due to the extensive surface area available for surfactant adsorption within the emulsion's droplets. By adopting this approach to establish correlations between the observed behaviour of the emulsion and the real surfactant coverage at the droplet interface, a more accurate assessment of our guess can be achieved.

Due to surfactant adsorption, emulsification produces a large liquid-liquid area that can significantly reduce the surfactant concentration in the bulk solution. The fact that at equilibrium (for soluble surfactant such as C12EO21), adsorption isotherm $c(\Gamma)$, is proportional to the bulk concentration must be taken into consideration in order to explain this depletion.

In accordance with the creation of an interface with area A in a surfactant solution with an initial concentration of c_0, an adsorption process starts, leading the system to achieve a new equilibrium state. This state is characterized by the presence of an adsorption value Γ and a bulk concentration denoted as c, that satisfy both the mass balance and the adsorption isotherm.

$$\begin{cases} A\Gamma + cV = c_0 V & mass\ balance \\ c = c(\Gamma) & adsorption\ isotherm \end{cases} \tag{7.14}$$

Where V is the volume of the surfactant solution.

Prior research [81] has established a well-known fact: the adsorption equilibrium behaviour of surfactants like C12EO21, which belong to the class of poly-oxyethylenated alcohols, can be effectively described using a 2-state isotherm model. This model suggests that surfactant molecules have the ability to adsorb in two distinct states, denoted as Γ_1 and Γ_2. These states are characterized by specific occupation areas, ω_1 and ω_2, and surface activities, represented by b_1 and b_2. These parameters are interconnected through the relation: $b_1 = b_2 \left(\frac{\omega_1}{\omega_2}\right)^{\alpha}$.

Solving the set of equations (7.14) for the 2-state isotherm requires a numerical approach, as the isotherm cannot be explicitly resolved. However, based on the optimal fit parameters derived from equilibrium interfacial tension measurements, obtained through pendant drop experiments at the water-MCT interface for C12E21 (ICMATE), it can be deduced that, in the PASTA experiments, operations consistently occur within a range of low concentrations. In this regime, the quantity of molecules adsorbed in the state with the smaller occupation area, ω_2, becomes negligible. Under these circumstances, the 2-state isotherm simplifies to a more manageable form.

$$c = \frac{\omega_1 \Gamma}{b_1(1 - \omega_1 \Gamma)} \tag{7.15}$$

This corresponds to the Langmuir isotherm, where the occupation area and surface activity are associated with the state possessing the larger occupation, expressed as $b_1 = b_2 \left(\frac{\omega_1}{\omega_2}\right)^{\alpha}$.

Assuming the **Langmuir** model, the corresponding adsorption isotherm is explicit.

$$\begin{cases} A\Gamma + cV = c_0 V \\ c = \dfrac{\omega\Gamma}{b(1-\omega\Gamma)} \end{cases} \tag{7.16}$$

Advancing the system further and incorporating the volume ratio ϕ, defined as the ratio of the volume of oil to the total volume of the aqueous surfactant solution $\phi = V_{oil}/V$, allows for the calculation of Γ through a second-order equation.

$$\omega\phi qb\Gamma^2 - (\phi qb + \omega + \omega b c_0)\Gamma + bc_0 = 0 \tag{7.17}$$

taking the solution with the minus sign before the square root, which in fact satisfies the inequality $\omega\Gamma < 1$, the latter represents the coverage, that is, the fraction of interface occupied by the surfactant molecules. Furthermore, the parameter q in the equation (7.17), which depends on the droplet size distribution, indicates the ratio between the total number of droplets are and volume in the emulsion $q = \phi A/V$. For monodisperse emulsion, this quantity takes the value of $q = \frac{3\phi}{R}$, where R is the mean drop radius. In the scenario of emulsions featuring a bimodal distribution characterized by radii R_1 and R_2, q takes on the following expression:

$$q = \phi\left[f\frac{3}{R_1} + (1-f)\frac{3}{R_2}\right] \tag{7.18}$$

With f, the volume fraction of droplets with radius R_1.

This bimodal model is more accurate in describing the emulsion conditions during the PASTA experiment, according to the results of the microscopy investigations. It is also feasible to obtain information on the temporal evolution of R (small droplets) and of the associated volume fraction f from the DWS analysis.

To calculate the depletion of surfactant concentration due to adsorption on emulsion drops, one can assume of a constant $R_2 = 60\ \mu m$. Currently, by considering the bimodal distribution and applying the above calculation, coverages $\omega\Gamma$ (representing the fraction of droplet area occupied by the adsorbed surfactant molecules) are derived and depicted in figure 7.21. In this analysis, Langmuir isotherm parameters $b = 52.3\ m^3/mol$ and $\omega = 1.4 \cdot 10^6 mol/m^2$ are employed. These values have been calculated based on measurements conducted in ICMATE (Genova, Italy), where interfacial tension was examined in relation to the concentration.

Apparently, at the lower ϕ, the coverage does not reach an equilibrium value, while the mean free path of transport is slowly increasing. This is incoherent with the bimodal distribution with R_2 constant. The coverage $\omega\Gamma$ is overall decreasing with the increasing of ϕ. This aligns with the fact that the amount of available surfactant molecules decreases with high oil volume, while the radii of small droplets show a weak dependence on volume ratio.

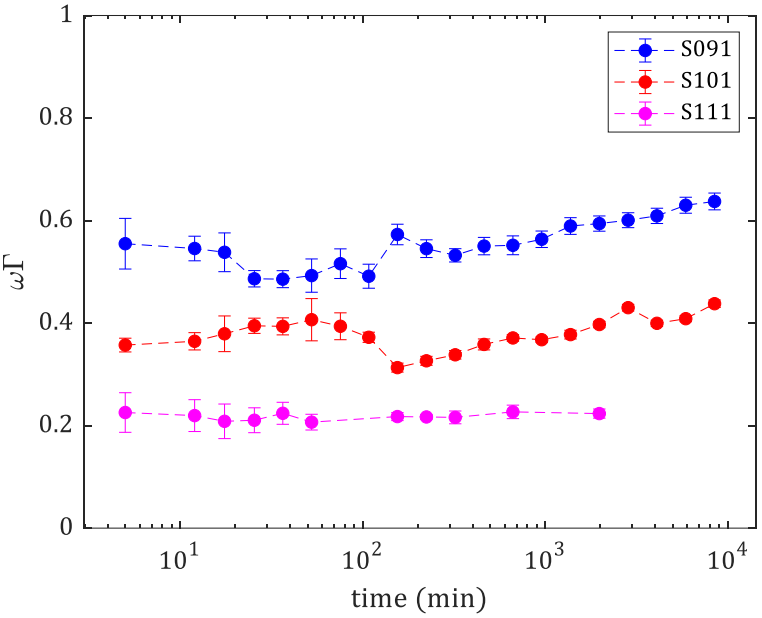

Figure 7.21 Coverage ωΓ as function of aging time for emulsions S091, S101, S111, respectively with 10^{-5} *M surfactant content and 20%, 30% and 50% oil content. The coverage is lower with higher amounts of oil in water.*

Overall, coverage seems constant over time as an equilibrium system, then the adsorption dynamics should not really play a role. The results on coverage reached at the time of concluding this thesis is subject to ongoing analysis, with some open problems yet to be addressed.

8. Solid foams for photocatalytic purification of air and water

Our research team has dedicated significant efforts to studying emulsion technology and solid foams, both in gravity and microgravity environments. These areas of research hold great promise as enabling technologies for future space exploration activities. Moreover, our projects prioritize a green technology approach, aligning with sustainable practices and minimizing environmental impact. By focusing on green technology, we aim to achieve more efficient utilization of materials, which in turn reduces the costs associated with development and production. Additionally, adopting environmentally friendly methods and products carries significant benefits for both the environment and human health. As previously discussed in earlier sections, the SPUMA (PRIN 2022AFXC29 , P.I. Luigi Cristofolini, "Solid Foam Photocatalytic Multiscale Filters - SPUMA ") project stands as another significant attempts undertaken by our research group.

The SPUMA project has a comprehensive objective of developing hierarchical porous objects that encompass multiple length scales, ranging from the meso- to the macro-scale. These objects will serve as highly efficient PCO (photocatalytic oxidation) filters, specifically activated by visible light emitted from LED sources. The project aims to achieve this by utilizing multiscale structures based on solid foams, characterized by open pores ranging from sub-micron to fractions of millimeters. These solid foams exploit photocatalytic titania nanoparticles as building blocks. Additionally, the project intends to incorporate larger open pores, typically in the millimeter range, into the structures through additive manufacturing using hybrid polymer-based formulations. To optimize the design and performance of the filters, optical Monte Carlo and ray tracing simulations will be employed. These simulations will guide the design process, ensuring a reasonably homogeneous distribution of light throughout the filter volume. The overall goal is to achieve homogeneous photo activation, with porosity adjusted to strike a balance between efficient air flow, facilitated by large pores, and effective PCO purification, which benefits from a larger surface area provided by smaller pores. To evaluate the performance of the developed filters, a laboratory-scale plant will be designed, constructed, and utilized for testing. The PCO activity will be assessed against various substances of industrial relevance, including volatile organic compounds (VOCs) and microorganisms. Additionally, the filters will be tested against air-borne pathogens relevant to nosocomial environments.

The project involves the characterization of stimuli-responsive and photoactive nanoparticles and hybrid nanostructures. These materials, undergo SEM (Scanning Electron Microscopy) analysis with EDS (Energy-dispersive X-ray Spectroscopy) microanalysis. Other characterization techniques include Raman and UV-Vis spectroscopy, DLS (Dynamic Light Scattering) with Z potential measurements and AFM (Atomic Force Microscopy). Correlation Spectroscopies are regularly employed to characterize foams. Furthermore, Monte Carlo simulations are utilized for interpreting experimental results.

In traditional PCO (photocatalytic oxidation) devices, anatase titania (TiO2) is commonly used as nanocrystals or films, which are activated by UV-C light. UV-C radiation itself has some antimicrobial activity but can also produce ozone, a harmful gas that requires an additional filtration. More recently, PCO activated by visible light has been proposed, employing more efficient LED sources and with longer operational life than the Hg lamps employed in classical PCO filters [82]. Titania exists in four natural polymorphs, with rutile and anatase being the most common ones. Rutile is the stable form, and the other polymorphs tend to convert into rutile through thermal treatment [83]. Since anatase has the highest photocatalytic efficiency, it is crucial to ensure that the titania used in PCO applications is in the desired crystalline form, moderate metal doping makes the anatase phase more resistant to temperature. To produce Titania NPs Zn-doped, a sol-gel synthesis process is exploited in isopropanol in the presence of Ti and Zn precursors, followed by calcination to 500 °C. This pathway is attractive as it produces anatase, both as a pure phase and as a majority phase (photocatalytic anatase phase is predominant, accounting for more than 85% in weight) [84]. Research has shown that moderate doping of zinc (Zn), with a ratio of about 0,5 % mol of Zn/Ti [85,86], slightly reduces the energy of the band gap while

maintaining the high photocatalytic activity of pure Titania. It also stabilizes the anatase phase, preventing the thermally induced phase transition from anatase to rutile. The photocatalytic capability of these NPs is tested by degrading Rhodamine B in a water suspension. The first step for the realization of a solid foam is the creation of a liquid foam stabilized by the nanoparticle-surfactant complexes. Those complexes are formed through self-assembly, gradually adding a water solution of CTAB (Hexadecyltrimethylammonium bromide) to a water suspension of NPs and its interfacial activity is maximized by tuning the NP/surfactant ratio. These complexes were used to stabilize both liquid and solid foams, whose morphology and pore size distribution was characterized by SEM and optical microscopy. Subsequently, foams are solidified by gel casting procedure using solution of PVA (poly-vinyl-alcohol) crosslinked with DHF (2,5-Dimethoxy-2,5-dihydrofuran) as a cross-linker agent. The jellification time can be controlled by the concentration of the crosslinker, pH, or temperature, minimizing aging effects. After foaming, the polymeric matrix is hardened through a mild thermal treatment. The photocatalytic activity of the solid foam was evaluated following a similar procedure as the one used for testing the NPs. The results demonstrate the decrease in RhB concentration over time and the UV-visible absorption spectra, exhibit the characteristic features of photoinduced de-ethylation of RhB. Remarkably, in these first results, the rate of photocatalytic degradation achieved by the foam slightly surpasses that achieved by the NPs alone [84].

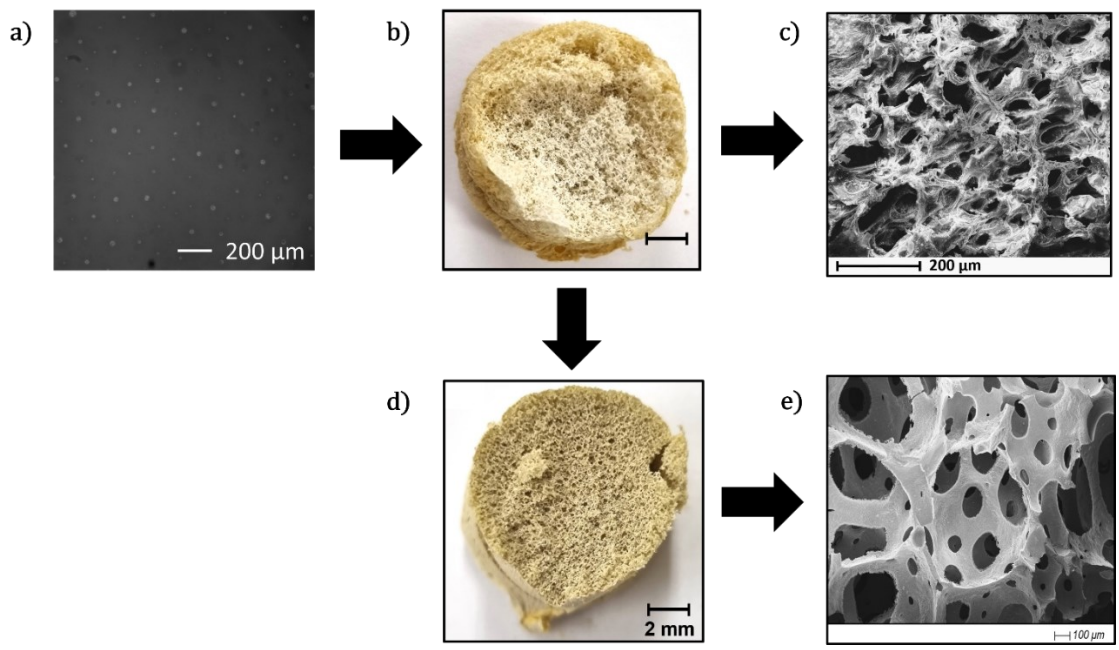

Figure 8.1 a) Liquid foam precursor: micrometric bubbles disperse in liquid matrix b) TiO2 NPs – PVA stabilized solid foam. c) SEM acquisition of a solid foam portion d) Sintered TiO2 NPS solid foam e) SEM acquisition of a sintered solid foam portion. The procedure for transforming the liquid precursor into a solid foam involves several steps. Firstly, the crosslinker, DHF, is added to the precursor. Then, foaming occurs, followed by a heating process at approximately 80 °C. This process results in the formation of a solid hybrid material composed of TiO2 NPs and PVA. The foam possesses compact open cells, with an average pore size of approximately 9.3 µm *and a variance of* 283 μm^2. *To convert the "hybrid" foam into a fully solid foam, a debinding treatment is conducted at 300°C, followed by a sintering treatment at 700°C. During the sintering process, an issue arises concerning the transformation from anatase to rutile, which is mitigated by introducing metal doping.*

These results mark a significant step forward in the development of compact and energy efficient PCO filters that utilize objects with hierarchical porosity, derived from foams stabilized by photocatalytic NPs. The enhanced efficiency of these filters makes them particularly valuable for air purification in various settings, including industrial and nosocomial environments, as well as in demanding sectors such as aerospace. These advanced filters hold promise for human space exploration, a strategic sector recognized as a priority by NASA and ESA agencies. Indeed, one crucial challenge in space exploration is the prevention and control of airborne and waterborne pathogens and photocatalytic solid foams present a promising solution.

Through our research, we seek to combine economic savings with positive impacts on the environment and health. This approach allows us to optimize resource utilization, minimize waste generation, and develop sustainable solutions for space exploration and beyond. By exploring emulsion technology and solid foams through the lens of green technology, our research team contributes to the advancement of space exploration while ensuring a responsible and sustainable approach to our work.

9. Conclusions and Perspectives

From an application and perspective standpoint, emulsions play a fundamental role in various industries. The stability and breakdown of emulsions are critical factors in these applications. Key parameters for product performance are droplet size and volume density, which must remain stable under challenging environmental conditions. A comprehensive understanding of the role of surface-active species in emulsion stabilization is essential, as it has wide-reaching implications.

While significant progress has been made in understanding emulsions, many details remain unclear. The development of emulsifiers and de-emulsifiers still relies heavily on empirical knowledge. A more systematic approach to the design of these additives will contribute to the green economy by promoting efficient resource and energy use while minimizing negative impacts on the environment and health. The results of this study have the potential to pave the way for such advancements by providing data that can be used to create models for predicting emulsion behaviour based on the chemical and physical properties of the liquids and interfaces involved.

The successful execution of the first set of microgravity experiments using the ESA Soft Matter Dynamics facility as part of the MAP project Emulsion Dynamics and Droplet Interfaces (EDDI) has yielded promising insights into the behaviour of emulsions under unique conditions. By employing Diffusing Wave Spectroscopy (DWS) and related techniques, the ageing of emulsions has been effectively examined, spanning from semi-dilute to concentrated. In this experiment we developed and validated a tools capable of real-time monitoring the dynamic evolution of vital parameters in microgravity-emulsions. These parameters include the mean drop size, the number density of drops, and the ability to detect any sudden changes in droplet dynamics such as avalanche type phenomena. This particular investigation is innovative, as previous research has primarily focused on observing transients in arrested systems like granular materials and foams. In such systems, sporadic sequences of dynamic events occur within inherently stationary conditions.

In stark contrast, our research reveals a novel phenomenon characterized by stationary diffusive dynamics, occasionally punctuated by ballistic transients. These transients are tentatively attributed to the coalescence events of droplets.

Moreover, by specialized DWS modeling, we have gained access to both qualitative and quantitative characteristics of the processes involved in emulsion evolution, including coalescence, aggregation, and Ostwald ripening.

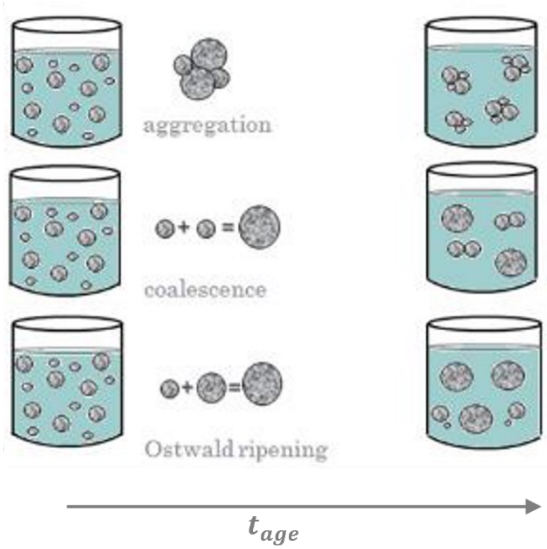

Figure 9 Sketch of the processes governing emulsion evolution in microgravity, including coalescence, aggregation, and Ostwald ripening.

Through a comprehensive analysis involving hydrodynamic drop radius, ballistic velocity, and mean free path on transport, distinct de-emulsification mechanisms have been identified. These mechanisms primarily involve interactions between small droplets, with additional interactions between small and large droplets becoming prominent during the later stages of de-emulsification.

The wealth of data and insights obtained from these experiments has paved the way for future investigations, with plans for new experiment campaigns set to take place between 2023 and 2025 on board the ISS, building by the presented results.

Nonetheless, our progress in these microgravity experiments also highlights the presence of certain unresolved issues and technical challenges that require careful attention and further exploration. For instance, the mechanical properties of the fluid phases are known to impact on the emulsion production and its evolution, and as such it would be very important to address this aspect e. g. by introducing viscosity modifiers and/or inducing non-Newtonian character in the fluid phases.

In all the investigations reported so far, a small amount of air (order of 5% in volume) is necessarily introduced for reasons related to thermal expansion differences. This results in a certain population of air bubbles, which contribute to the DWS signal itself, besides possibly affecting drop dynamics via drop-bubble coupling. The subject of drop-bubble coupling is interesting *per se*, as many real-life systems contain both gaseous and oil dispersed phases. However, a simpler system would be desirable from some points of view.

In the investigations reported so far, only marginal use was made of direct space imaging. This is justified by the fact that the existing observation chain (OVC) is not optimized for emulsions. Nevertheless, with appropriate adjustments, direct observation could provide valuable information complementing DWS, posing bases for reliable implementations of ray tracing algorithms and allowing, to precisely identify critical features that trigger de-emulsification. This would be made possible at first by improvements to the already existing camera. In perspective, confocal microscopy, like that implemented in the FLUMIAS facility, would provide high-precision information on emulsion structure and its dynamics.

Lastly, incorporating tensiometry experiments to analyse surface tension and distinguish contributions from drops and bubbles will be a pivotal step in addressing these technical challenges. These experiments could provide valuable insights into the interfacial properties of emulsions.

It is easy to foresee a major role for Artificial Intelligence in managing all this wealth of information. AI could contribute important insight, e.g. correlating direct space imaging, and patterns of speckle evolution to the different phenomena driving emulsion ageing, like drop population dynamics, drop-drop interactions, to establish simple and reliable criteria for early predictors of emulsions' fate.

It is clear that these findings hold great potential for the advancement of emulsion-related technologies and products. The knowledge generated through this research will significantly contribute to addressing applicative needs in various industries, ultimately facilitating the development of innovative solutions and products that rely on a deep understanding of emulsion dynamics. Moreover, our results might lead to enrich an emulsion database, which could serve as a valuable resource for crucial parameters, such as those required for hydrodynamic correlation modelling.

In conclusion, the prospects for technologies involving emulsions and colloids are very promising, both in the context of space exploration and the broader sphere of sustainable industrial practices on Earth. These innovative approaches not only hold the key to enhancing space missions by improving air purification and heat transfer technologies, thus making interplanetary travel more feasible and efficient, but they also offer a profound opportunity to revolutionize our approach to industry. By transcending the current empirical methodologies, these advancements open the door to a more sustainable and environmentally friendly future, ensuring that our quest for exploration and our commitment to ecological responsibility go hand in hand. As we navigate the challenges of both space and our home planet, it is evident that these pioneering approaches offer a brighter and more sustainable future for us all.

List of Figure

3.1 *A schematic representation of light scattering experiment in Homodyne configuration, where xy indicates the scattering plane.*

3.2 *Setup for heterodyne configuration: laser radiation hits the beam splitter, thus generating a "second beam" that will be used as a second input (local oscillator). The initial beam continues along the optical path to the sample, passes through the sample and produces diffuse radiation that will be used as the first input (scattered light). The two outputs are collected in fiber. The correlator finally generates the autocorrelation functions of the mixed intensity.*

3.3 *The first panel on left, show DLS correlation function in homodyne (unmixed), heterodyne (mixed) and heterodyne configuration with translating sample (mixed translate) overlap with their simulated curves. On second panel the heterodyne configuration with translation is tested for three different translation speed at* $300\ \mu m/s, 166\ \mu m/s$ *and* $83\ \mu m/s$.

3.4 *Example of distributions of path length s,* $P(s, l^*)$, *generated. Top panel: Backscattering detector; Bottom panel: Transmission detector. The colour indicates the value of* l^* *(from 100 micron up to 3mm) corresponding to each curve (from blue to yellow)*

3.5 *Left panel: reduced* χ^2 *of the fits for each value of* l^*, *the red point indicates the minimum value* χ^2. *Right panel: red lines are the best fits to the measured correlation functions, in green and blue are "wrong" fits: the model curves for BS and FW are either too far apart (*l^* *too short) or too close to each other (*l^* *too large).*

4.1 *Interior of the SMD container. The main components are the experiment container controller unit (ECCU), the sample cells (SC) in the sample cell units (SCU) and the stepper motor to drive the carousel with the sample cell units. The diagnostics consist of a laser, overview camera, line camera and avalanche photodiodes with a hardware-implemented intensity correlator.*

4.2 *On the left calibration images from the OVC. On right examples images of an emulsion acquired with OVC.*

4.3 *On the left: time resolved intensity autocorrelation: each line corresponds to a specific delay time (ms). On right: raw spatio-temporal speckles images*

4.4 *On left APD layout. An APD consists of 4 sub-APDs, resulting in four photon count channels. On right the correlation curves in Transmission and Backscattering acquisition*

4.5 *Examples of photon count traces for both Transmission and Backscattering geometry*

4.6 *The optical diagnostics of the soft matter dynamics experiment container are presented in a schematic representation. At the centre of the setup is a sample cell, and multiple sample cells (up to four) are arranged as a unit on a carousel, as shown in Figure 3.12. By rotating the carousel, one sample cell at a time can be brought into the measurement position, enabling access for diagnostics. The sample cell unit consists of a body made of cyclic olefin copolymer (COC) and features a three-faceted prismatic interface for both the illuminating light and the light backscattered from the sample. Two collimators, positioned perpendicular to their respective facets, collect the backscattered light for the line camera (LC) and the avalanche photodiodes (BS). In the transmission direction, the collimator collects the light transmitted (FW) through the flat cell wall and directs it towards the photodiodes (APDs). The overview camera*

(OVC), equipped with a microscope objective, captures images of the sample from the top surface of the sample cell. To illuminate the sample, three light emitting diodes (LEDs) are employed. Additionally, a piston mechanism can be utilized for emulsifying the samples.

4.7 The sample container with four sample cells, each of which houses at the bottom the piston shaft, which ensures the emulsification process. At the top two optical interfaces (one on front and one on back) for laser diagnostics, while on the cell lid, a window, allows microscopy and imaging measurements.

4.8 Here is a picture of the sample cell (SC). The upper part of the cell is used as a microscope window. The central part contains the sampled emulsion volume with the prism used to accommodate simultaneous lighting and light collection with APD and linecamera. The Gaussian beam impinges one side of the pyramidal prism (spot-in lighting, orange point); the backscattered light is collected by several detectors from two different points, (spot-out collection, green and blue point) placed at a distance d_(in-out) from the lighting point.

5.1 Beam profile along x-axis (panel a)) and y-axis (panel b)). The mean normalized linecamera intensity is here shown as a function of the LC pixel and lines.

5.2 Diagram of a cell in which the fraction of oil, water and air is displayed. It is necessary to insert a percentage of air inside the water/oil sample to bypass the effect of overpressure in the SMD cell, due to the thermal expansion of liquids.

5.3 Transport mean free path of oil in water (50-50) bubbly emulsion with 4% of air content. In panel a) air bubbles and oil drops have the same size, while in panel b) air bubbles are 4 times larger than oil drops because of the different surface tension of MCT/water and air/water at the given surfactant concentration.

5.4 a) Mie simulation of the mean free path of transport l^* due to air bubbles, polystyrene nanoparticles (PS 900 nm) and ${l^*_{eff}}^{-1} = (l^*_{PS} + l^*_{air})^{-1}$. Up to 100 microns size of air bubbles both l^* values become comparable. This could result in an effective Diffusion coefficient (panel b)) which has a lower value than expected for the suspension of nanoparticles.

5.5 Schematic of the EBB, as a prototype of the equipment on board. The laser light is collided and engraves on the prism and then passes through the sample. The detection takes place in both geometries (BS and FW) thanks to photomultipliers that are connected to the correlator and then to the software. Complete the optical analysis OVC and LC.

5.6 a) Brownian and Shear time as function of aging time and varying air concentration from 0 to 1%, for freshly emulsion with 50:50 MCT oil/water and stabilized by C12EO21 10^{-4} M. b) Trend of Peclet number $Pe = \tau_B/\tau_S$

5.7 a) Brownian and Shear time as function of aging time and varying air concentration from 0 to 1%, for freshly emulsion with 50:50 MCT oil/water and stabilized by C12EO21 $2 \cdot 10^{-4}$ M. b) Trend of the rays obtained from Brownian diffusion coefficient (linked to τ_B). After about 5 minutes from emulsification procedure, the creaming take place.

5.8 a) Drop radius as function of aging time and varying air concentration from 0 to 4 %, for freshly emulsion with 50:50 MCT oil/water and stabilized by C12EO21 $2 \cdot 10^{-4}$ M. b) Standard deviation of velocities σ_v

as function of aging time and varying air concentration from 0 to 4 %, for freshly emulsion with 50:50 MCT oil: water and stabilized by C12EO21 $2 \cdot 10^{-4}$ *M*

5.9 *The proposed procedure: from left to right, by DWS experiments and a set of Optical Monte Carlo (OMC) simulations, a calibration sample is fully characterized with respect to its internal dynamics and the photon transport mean free path* l^**. Then, this same sample is measured by the specialized DWS to be calibrated; by analysing the results in the light of MC simulations, the optical parameters of this setup are determined. Finally, this is used (right panel) to investigate the emulsions of interest.*

5.10 *DWS transmission (FW, black dot) and backscattering (BS, red dot) correlations function, simultaneously measured on a polystyrene suspension and in laboratory set up. The best fit (black and red lines) results in a determination of* l^* *and of the diffusion coefficient of the nanoparticles*

5.11 *a) Reduced* χ^2 *of the fit for each value of optical distance between spot in and spot out* d_{in-out}*. The minimum value of* χ^2 *corresponds to an optical distance* $= 2.175 \pm 0.005$ *mm for this specific setup geometry. b) DWS transmission (FW APD, black dots) and backscattering (BS APD, red dots) correlations function, simultaneously measured on a polystyrene suspension in Engineering Model set up. The best fit (black and red lines) results in the determination of optical distance* d_{in-out} *and Brownian time* τ_B*.*

5.12 *a) Reduced* χ^2 *of the fit for each value of mean free path of transport* l^**, without optical distance* d_{in-out}*. The minimum value of* χ^2 *corresponds to an* $l^* = 0.99 \pm 0.1$ *mm b) DWS transmission (FW APD, black dots) and backscattering (BS LC, red dots) correlations function, simultaneously measured on a polystyrene suspension in Engineering Model set up. The best fit (black and red lines) results in the determination of mean free path of transport* l^* *and Brownian time* τ_B*.*

5.13 *Diagram illustrating the initialization and acquisition protocols of the PASTA experiment conducted aboard the International Space Station (ISS). The sequence progresses from left to right outlines the sequential execution of the various protocol: starting with optimization and progressing through shorter investigation times, a 2-hour Protocol A, and concluding with the extended 120-hour Protocol B, which focuses on studying sample aging.*

5.14 *Figure show 5 repetitions of polarizer optimization loop. Then polarizers identified intensity minima is at about 60 degrees while the intensity maxima is at 150 degrees.*

5.15 *a) Reduced* χ^2 *of the fit for each value of* l^* *for freshly prepared emulsion with 50:50 MCT oil: water and stabilized by C12EO21,* $c = 10^{-4} M$*. The minimum value of* χ^2 *corresponds to a* $l^* = 0.95 \pm 0.1$ *mm. b) DWS transmission (FW, black dot) and backscattering (BS, red dot) correlations function, simultaneously measured on a polystyrene suspension and in Engineering Model set up. The best fit (black and red lines) results in a determination of* l^*, τ_B, τ_S*.*

6.1 *Gray value for runs flat field (polystyrene nanoparticles standard sample). The average intensity as a function of pixels is homogeneous in the central 500 pixels ROI (red square).*

6.2 *overview camera images acquired for 16-bit depth with FoV of 2448 x 2048 (left), 1600 x 1200 (right)*

6.3 *OVC Images of processed SC's before / after A0 protocol (initial emulsification of samples): in panel a) is shown sample SC 09-1 (20:80 o/w* 10^{-5} *M), in panel b) is shown sample SC 10-1 (30:70 o/w* 10^{-5} *M) and finally in panel c) is shown sample SC 11-1 (50:50 o/w* 10^{-5} *M).*

6.4 *Sample SC 09-1 (20:80, $10^{-5}M$) images from OVC data. The a) panel show the sample in A1 protocol recording, while the b) panel show the sample in A2 protocol recording.*

6.5 *Sample SC 09-1 (20:80, $10^{-5}M$) average intensity as function of pixel from LC data. The top panel show the sample in A1 protocol recording, while the bottom panel show the sample in A2 protocol recording.*

6.6 *Polystyrene Correlation function in Backscattering from APD (line), Backscattering from LC (dashed line) and Transmission (dot) acquired on board the ISS before (black) and after (red) the full shaking procedure.*

6.7 *In this figure the relaxation time of Backscattering Correlation function from APD for each measurement of polystyrene sample (5 measure of 120 second) before and after the "emulsification" procedure (i.e., shaking of sample at 18 Hz, 2 minutes, 4 cycles).*

6.8 *In this figure the relaxation time of Transmission Correlation function from APD for each measurement of polystyrene sample (5 measure of 120 second) before and after the "emulsification" procedure (i.e., shaking of sample at 18 Hz, 2 minutes, 4 cycles).*

6.9 *Emulsions 11-3 ($2 \cdot 10^{-4}M$ 50:50 o/w) Correlation function in Backscattering (panel a)) and Transmission (panel b)) acquired on ground (red dot) and on board the ISS (blue dot from APD and blue circle from LC). The difference in the decay of the correlation function acquired using DWS or LC can be attributed to the variation in the optical distance between the input and output lighting spots for the two different detectors.*

6.10 *1/e relaxation time of the backscattering (filled squares) and transmission (empty diamonds) correlation functions, as a function of the time from emulsification for the PASTA samples: from left to right increase of oil fraction (20:80, 30:70, 50:50 oil/water ratio) and surfactant (C12EO21) concentration $2 \cdot 10^{-4}M$ in water*

6.11 *1/e relaxation time of the backscattering (filled squares) and transmission (empty diamonds) correlation functions, as a function of the time from emulsification for the PASTA samples: from left to right increase of oil fraction (20:80, 30:70, 50:50 oil/water ratio) and surfactant (C12EO21) concentration 10^{-5} M in water.*

7.1 *The Marangoni effect arises when there is a gradient in surface tension on the liquid's surface, caused by differences in temperature, concentration, or composition. Regions with lower surface tension tend to experience a net inward flow, pulling liquid from regions with higher surface tension. As a result, the liquid moves and generates flow patterns that can lead to a range of interesting effects, such as the spreading of liquid droplets. The figure demonstrates an event where the merging of two drops results in a reduction of the interfacial area. This reduction triggers the desorption and release of surfactant in solution. Consequently, a gradient of surfactant concentration forms in the continuous phase, giving rise to a Marangoni effect.*

7.2 *Representative microscopy images of droplet population in emulsion S092. Images provided by AUTH, Thessaloniki, Greece*

7.3 *Droplet Size Distribution for S092. Respectively droplet number density function (left) and droplet volume probability density function (right). Distribution provided by AUTH, Thessaloniki, Greece.*

7.4 *Hydrodynamic droplet radius as function of emulsions aging, for the small droplets. In left panel is shown the samples SXX-1, with surfactant concentration* $c = 10^{-5}M$ *and in the right panel the samples SXX-2, with surfactant concentration* $c = 4 \cdot 10^{-5}M$

7.5 *Mean photon transport length* l^**, as function of emulsion aging, for SXX-1 (left, surfactant concentration* $10^{-5}M$ *) and SXX-2 (right, surfactant concentration* $4 \cdot 10^{-5}M$)

7.6 *Ballistic velocities, as function of emulsion aging, for SXX-1 (left, surfactant concentration* $10^{-5}M$*) and SXX-2 (right, surfactant concentration* $4 \cdot 10^{-5}M$)

7.7 *Fraction of oil in small droplets as a function of emulsions aging. On the left the surfactant concentration in solution is* $10^{-5}M$*, while on the right* $4 \cdot 10^{-5}M$*. Roughly 10% of the oil volume in all emulsions is found within the small droplets, with the majority being clearly associated with the formation of larger droplets.*

7.8 *A speckle pattern is generated on the camera optical plain, and a single line is acquired from line Camera detector. Single lines are collected into 2D images incrementally and set of data is processed with a fixed lag time* τ*. Several* τ *are used to produce the autocorrelation function at each lag times as a function of time.*

.

7.9 *Time resolved* $g_2(t_{age})$ *for freshly emulsion prepared with 50:50 oil/water ratio and* 10^{-5} *M surfactant (sample S 11-1) content at different lag time* τ (ms).

7.10 *Examples of Time resolved* $g_2(t_{age})$ *at different lag time* τ (ms) *from the elaboration of the SMD line camera data, at the early stage of the aging sample 11-1: oil/water ratio 50:50; surfactant (C12EO21) concentration* $10^{-5}M$ *in water. Transient events, depicted as dark spikes in the* g_2 *plot as a function of aging time, can be observed. These events indicate rapid accelerations in the decay of the correlation function.*

7.11 *The figure presents the frequency of transients as a function of surfactant concentration and ageing time. Starting from the top left panel, emulsions contain C12EO21 in quantities of* $1 \cdot 10^{-5}$ *M. Immediately to the right are emulsions with a surfactant content of* $4 \cdot 10^{-5}M$*. Moving to the lower left panel, the surfactant content increases to* $1 \cdot 10^{-4}M$*, and finally, the bottom right panel shows emulsions formed with* $2 \cdot 10^{-4}M$ *of C12EO21 in aqueous solution.*

7.12 *Transient frequency as a function of ageing time. From red to black increases the concentration of surfactant, while the dots represent the fraction of oil in water lower (20%), which increases with squares (30%) up to asterisks (50%)*

7.13 *Image from elaborated Line Camera data of time against pixel. Series of normalized correlation function $g_2(\tau)$ during the temporal evolution of transient event. The time resolved correlation function in blue are computed at beginning of the event τ_{start}, then in light blue the correlation function computed during the event at τ_{event}. The colours scale of the correlation functions continues with green, yellow, orange to finish with red when the event is ended at τ_{end}.*

7.14 ***a)*** *α and D trend for the sample 09-1 (20:80 o/w, $10^{-5}M$) immediately after emulsification at about 4 minutes aging time. The residues of the emulsification process are observable both in the coefficient of anomalous diffusion D and in the fitting parameter α, circled in red.* ***b)*** *α and D trend during the transient event for the sample 09-1 (20:80 o/w, $10^{-5}M$) at about 20 minutes from emulsification. The transient event is circled in red and can be identified by a peak and a subsequent relaxation of the anomalous diffusion parameters D and α.*

7.15 *Trend of relaxation time, both Brownian time τ_B and shear time τ_s, on the top of a) and b) panels. Ballistic velocity on the bottom of a) and b) panels, during the transient event for sample 09-1 (20:80 o/w, $10^{-5}M$) shortly after emulsification (a) panel) and at aging time about 30 minutes from emulsification (b) panel)*

7.16 *Trend of relaxation time, both Brownian time τ_B and shear time τ_s, on the top of the figure. Ballistic velocity on the bottom of the figure for sample 11-4 (50:50 o/w, $2 \cdot 10^{-4}M$). Example of double event.*

7.17 *Trend of relaxation time, both Brownian time τ_B and shear time τ_s, on the top of figure. Ballistic velocity on the bottom of the figure for sample 10-1 (30:70 o/w, 10^{-5} M). On the right a time-resolved $g_2(t_{age})$ where the intermittent events is depicted as dark spikes in the g_2 plot as a function of aging time. The event takes place about 70 minutes from emulsification, and it ends in 1.5 seconds.*

7.18 *Trend of relaxation time, both Brownian time τ_B and shear time τ_s, on the top of figure. Ballistic velocity on the bottom of the figure for sample 10-1 (30:70 o/w, 10^{-5} M). On the right a time-resolved $g_2(t_{age})$ where the intermittent events is depicted as dark spikes in the g_2 plot as a function of aging time. The event takes place about 90 minutes from emulsification, and it ends in a tenth of second.*

7.19 *Velocity distribution in relation to the number of transient events observed in samples S091, S092, S101, S102, S111, S112. In the panel the amount of surfactant in the samples grows from $10^{-5}M$ to $4 \cdot 10^{-5}M$ going from left to right. Reading the data from top to bottom instead increases the amount of oil from 20 %, to 30% up to 50% or/w. Velocity histograms are obtained by collecting data for two hours of sample aging, after emulsification.*

7.20 *Trend of relaxation time, both Brownian time τ_B and shear time τ_s, on the top of a) and b) panels. Ballistic velocity on the bottom of a) and b) panels during a transient event observed from line camera. The sample, investigated on the ground, corresponds to sample S11-4 (50:50 o/w, $2 \cdot 10^{-4}$ M) on board. In this case, the sample nominally includes 0% air content. The sample is shown shortly after emulsification (a) panel) and at aging time about 7 minutes from emulsification (b) panel).*

7.21 *Coverage ωΓ as function of aging time for emulsions S091, S101, S111, respectively with* 10^{-5} *M surfactant content and 20%, 30% and 50% oil content. The coverage is lower with higher amounts of oil in water.*

8.1 *a) Liquid foam precursor: micrometric bubbles disperse in liquid matrix b) TiO2 NPs – PVA stabilized solid foam. c) SEM acquisition of a solid foam portion d) Sintered TiO2 NPS solid foam e) SEM acquisition of a sintered solid foam portion. The procedure for transforming the liquid precursor into a solid foam involves several steps. Firstly, the crosslinker, DHF, is added to the precursor. Then, foaming occurs, followed by a heating process at approximately 80°C. This process results in the formation of a solid hybrid material composed of TiO2 NPs and PVA. The foam possesses compact open cells, with an average pore size of approximately 9.3 micrometers and a variance of 283 square micrometers. To convert the "hybrid" foam into a fully solid foam, a debinding treatment is conducted at 300°C, followed by a sintering treatment at 700°C. During the sintering process, an issue arises concerning the transformation from anatase to rutile, which is mitigated by introducing metal doping.*

List of Acronyms

AFM	Atomic Force Microscopy
APD	Avalanche Photodiode
BS	Backscattering
BUSOC	Belgian User Support and Operations Centre
CCD	Charge-Coupled Device
CMC	Critical Micellar Concentrations
CMOS	Complementary metal-oxide semiconductor
COC	Cyclic olefin copolymer
CTAB	Cetyltrimethylammonium bromide
DHF	2,5-Dimethoxy-2,5-dihydrofuran
DLS	Dynamic Light Scattering
DSD	Drop Size Distribution
DWS	Diffusing Wave Spectroscopy
EBB	Elegant Bread Board
EC	Experimental Container
EDDI	Emulsions Dynamics and Droplet Interfaces
EDS	Energy-dispersive X-ray spectroscopy
EM	Engineering Model
ESA	European Space Agency
FOV	Full field of view
FSL	Fluid Science Laboratory
FW	Forward
ISRU	In Situ Resource Utilization
ISS	International Space Station
LC	Line Camera
LED	Light Emitting Diodes
MC	Monte Carlo
MCFA	Medium Chain Fatty Acids
MCT	Medium Chain Triglycerides
MM	Multi-Mode
MMA	Microgravity Measurement Assembly

MT Moving Tray

MSD Mean Square Displacement

NASA National Aeronautics and Space Administration

NR Neutron Reflectometry

NP Nanoparticles

OR Ostwald ripening

OVC Overview Camera

PCO Photocatalytic oxidation

PVA Poly-vinyl-alcohol

RhB Rhodamine B

ROI Region of Interest

SANS Small Angle Neutron Scattering

SAS Small-angle scattering

SC Sample Cell

SCU Sample Cell Unit

SEM Scanning Electron Microscope

SLD Scattering length density

SM Single-Mode

SMD Soft Matter Dynamics

SPUMA Solid Foam Photocatalytic Multiscale Filters

VOC Volatile organic compounds

List of Collaborations

CNR Inst. for Condensed Matter Chemistry and Energy Technologies - ICMATE (Italy)

- Co-Supervisor: Libero Liggieri

Aristotle University Thessaloniki - AUTH (Greece)

- Thodoris Karapantsios

Tokio University of Science & Chiba Institute of Science - TUS&CIS (Japan)

- Kazutami Sakamoto
- Yuji Yamashita

Virginia Commonwealth University -VCU (USA)

- James K. Ferri

Aix-Marseille Université -AMU (France)

- Mickael Antoni

COSMOS-Nikkol Group (Japan)

Darmstadt Technical University (Germany)

Acknowledgment

I would like to thank University of Parma, particularly my thesis supervisor, Prof. Luigi Cristofolini, and my co-supervisor, Prof. Libero Liggieri. I am also appreciative of my colleagues from the research group, Dr. Davide Orsi and Dr. Marco Vaccari, for their collaboration.
I would like to thank the European Space Agency for allowing us to conduct our experiment aboard the International Space Station within the MAP project "Emulsion Dynamics and Droplet Interfaces - EDDI," (ESA Contract n. 4000128643/19/NL/PG).
The Belgian User Support and Operations Centre for skilfully accompanied us throughout the experiment. The staff of Airbus, Defence and Space for the access to the "Elegant Breadboard" is gratefully acknowledged. I also wish to extend my acknowledgement to our esteemed industrial and academic partners, whose invaluable contributions have played an important role in the successful execution of this project.

Bibliography

[1] Miller R, Liggieri L. Interfacial Rheology. Leiden: Brill Academic Pub.; 2009.

[2] Hu X, Miller R, Guo L. Experimental study on interfacial characteristics during bubble dissolution. Colloids Surf A Physicochem Eng Asp 2016;505:179–85. https://doi.org/10.1016/j.colsurfa.2016.03.076.

[3] Yarranton HW, Sztukowski DM, Urrutia P. Effect of interfacial rheology on model emulsion coalescence. J Colloid Interface Sci 2007;310:246–52. https://doi.org/10.1016/j.jcis.2007.01.071.

[4] Langevin D. Influence of interfacial rheology on foam and emulsion properties. Adv Colloid Interface Sci 2000;88:209–22. https://doi.org/10.1016/S0001-8686(00)00045-2.

[5] De Aguiar HB, De Beer AGF, Strader ML, Roke S. The interfacial tension of nanoscopic oil droplets in water is hardly affected by SDS surfactant. J Am Chem Soc 2010;132:2122–3. https://doi.org/10.1021/ja9095158.

[6] Berg JC. An introduction to interfaces and colloids: The bridge to nanoscience. 2009. https://doi.org/10.1142/7579.

[7] Liggieri L, Miller R. Relaxation of surfactants adsorption layers at liquid interfaces. Curr Opin Colloid Interface Sci 2010;15:256–63. https://doi.org/10.1016/j.cocis.2010.02.003.

[8] Danov KD. Effect of Surfactants on Drop Stability and Thin Film Drainage. In: Starov VM, Ivanov IB, editors. Fluid Mechanics of Surfactant and Polymer Solutions, Springer US; 2004, p. 1–38. https://doi.org/10.1006/jcis.1998.5973.

[9] Aronson MP, Princen HM. Contact angles in oil-in-water emulsions stabilized by ionic surfactants. Colloids and Surfaces 1982;4:173–84.

[10] Teppner R, Haage K, Wantke D, Motschmann H. On the Internal Structure of an Adsorption Layer of an Ionic Soluble Surfactant. The Buildup of a Stern Layer Monitored by Optical Means. J Phys Chem B 2002;104:11489–96. https://doi.org/10.1021/jp002192q.

[11] Aveyard R, Binks BP, Esquena J, Fletcher PDI, Bault P, Villa P. Flocculation transitions of weakly charged oil-in-water emulsions stabilized by different surfactants. Langmuir 2002;18:3487–94. https://doi.org/10.1021/la011723e.

[12] Mowald H. Surfactant Layers at Water Surfaces. Reports on Progress in Physics 1993;56:653–85.

[13] Goloub T, Pugh RJ. The role of the surfactant head group in the emulsification process: Single surfactant systems. J Colloid Interface Sci 2003;257:337–43. https://doi.org/10.1016/S0021-9797(02)00047-4.

[14] Defay 1887-1988 (viaf)17297469 R, Prigožin 1917-2003 (viaf)99876969 IR, Bellemans A. Surface tension and adsorption. London : Longmans; 1966.

[15] Leermakers F, Eriksson JC, Lyklema H. Chapter 4 - Association Colloids and their Equilibrium Modelling. In: Lyklema J, editor. Soft Colloids, vol. 5, Academic Press; 2005, p. 4.1-4.123. https://doi.org/https://doi.org/10.1016/S1874-5679(05)80008-X.

[16] Langevin D. On the rupture of thin films made from aqueous surfactant solutions. Adv Colloid Interface Sci 2020;275:102075. https://doi.org/10.1016/J.CIS.2019.102075.

[17] Zeichner GR, Schowalter WR. Effects of hydrodynamic and colloidal forces on the coagulation of dispersions. J Colloid Interface Sci 1979;71:237–53. https://doi.org/10.1016/0021-9797(79)90235-2.

[18] Binks BP, Lumsdon SO. Stability of oil-in-water emulsions stabilised by silica particles. Physical Chemistry Chemical Physics 1999;1:3007–16. https://doi.org/10.1039/a902209k.

[19] Binks BP, Horozov TS. Aqueous foams stabilized solely by silica nanoparticles. Angewandte Chemie - International Edition 2005;44:3722–5. https://doi.org/10.1002/anie.200462470.

[20] Santini E, Guzmán E, Ferrari M, Liggieri L. Emulsions stabilized by the interaction of silica nanoparticles and palmitic acid at the water-hexane interface. Colloids Surf A Physicochem Eng Asp 2014;460:333–41. https://doi.org/10.1016/j.colsurfa.2014.02.054.

[21] Campbell RA, Wacklin HP, Sutton I, Cubitt R, Fragneto G. FIGARO: The new horizontal neutron reflectometer at the ILL. Eur Phys J Plus 2011;126:1–22. https://doi.org/10.1140/epjp/i2011-11107-8.

[22] Fayer MJ, Gee GW. Neutron Scattering. vol. 4. 2004. https://doi.org/10.1016/B0-12-348530-4/00505-1.

[23] L.G.Parrat. Surface Studies of Solids By Total Reflection of Xrays. Physical Review 1954;95:359–69.

[24] Skinner BJ, Appleman DE. Melanophlogite, a cubic polymorph of silica. Am Mineral 1963;48:854–67.

[25] Salager J-L. Basic theory, measurement, applications. Encyclopedia of Emulsion Technology 1988;3:79–134.

[26] Silva B, Rodríguez-Abreu C, Vilanova N. Recent advances in multiple emulsions and their application as templates. Curr Opin Colloid Interface Sci 2016;25:98–108. https://doi.org/10.1016/j.cocis.2016.07.006.

[27] Vladisavljević G. Recent advances in the production of controllable multiple emulsions using microfabricated devices. Particuology 2015;24. https://doi.org/10.1016/j.partic.2015.10.001.

[28] Dickinson E. Double Emulsions Stabilized by Food Biopolymers. Food Biophys 2011;6:1–11. https://doi.org/10.1007/s11483-010-9188-6.

[29] Verbich S V, Dukhin SS, Tarovski A, Holt Ø, Saether Ø, Sjo¨blom J. Evaluation of stability ratio in oil-in-water emulsions. Colloids Surf A Physicochem Eng Asp 1997;123–124:209–23. https://doi.org/https://doi.org/10.1016/S0927-7757(96)03939-8.

[30] Aveyard R, Binks BP, Clint JH. Emulsions stabilised solely by colloidal particles. Adv Colloid Interface Sci 2003;100–102:503–46. https://doi.org/10.1016/S0001-8686(02)00069-6.

[31] Jiang J, Zhu Y, Cui Z, Binks BP. Switchable pickering emulsions stabilized by silica nanoparticles hydrophobized in situ with a switchable surfactant. Angewandte Chemie - International Edition 2013;52:12373–6. https://doi.org/10.1002/anie.201305947.

[32] Yang H, Zhang H, Peng J, Zhang Y, Du G, Fang Y. Smart magnetic ionic liquid-based Pickering emulsions stabilized by amphiphilic Fe3O4 nanoparticles: Highly efficient extraction systems for water purification. J Colloid Interface Sci 2017;485:213–22. https://doi.org/10.1016/j.jcis.2016.09.023.

[33] Dutta A, Chengara A, Nikolov AD, Wasan DT, Chen K, Campbell B. Texture and stability of aerated food emulsions—effects of buoyancy and Ostwald ripening. J Food Eng 2004;62:169–75. https://doi.org/10.1016/S0260-8774(03)00229-2.

[34] Salonen A, Lhermerout R, Rio E, Langevin D, Saint-Jalmes A. Dual gas and oil dispersions in water: Production and stability of foamulsion. Soft Matter 2012;8:699–706. https://doi.org/10.1039/c1sm06537h.

[35] Lekhlifi A, Ouazzani J, Antoni M. Drainage of water droplets in a bounded paraffin oil continuous phase: Role of temperature, size and boundary walls. Colloids Surf A Physicochem Eng Asp 2014;460:342–50. https://doi.org/10.1016/j.colsurfa.2014.05.078.

[36] Lekhlifi A, Fanzar A, Antoni M. A numerical investigation on the drainage of a surfactant-modified water droplet in paraffin oil. Adv Colloid Interface Sci 2015;222:446–60. https://doi.org/10.1016/j.cis.2015.02.005.

[37] Leal-Calderon F, Gerhardi B, Espert A, Brossard F, Alard V, Tranchant JF, et al. Aggregation phenomena in water-in-oil emulsions. Langmuir 1996;12:872–4. https://doi.org/10.1021/la950615n.

[38] Dukhin SS, Mishchuk NA, Loglio G, Liggieri L, Miller R. Coalescence coupling with flocculation in dilute emulsions within the primary and/or secondary minimum. Adv Colloid Interface Sci 2003;100–102:47–81. https://doi.org/10.1016/S0001-8686(02)00073-8.

[39] Llamas S, Santini E, Liggieri L, Salerni F, Orsi D, Cristofolini L, et al. Adsorption of Sodium Dodecyl Sulfate at Water–Dodecane Interface in Relation to the Oil in Water Emulsion Properties. Langmuir 2018;34:5978–89. https://doi.org/10.1021/acs.langmuir.8b00358.

[40] Tchoukov P, Czarnecki J, Dabros T. Study of water-in-oil thin liquid films: Implications for the stability of petroleum emulsions. Colloids Surf A Physicochem Eng Asp 2010;372:15–21. https://doi.org/10.1016/j.colsurfa.2010.09.007.

[41] Kovalchuk VI, Makievski AV, Krägel J, Pandolfini P, Loglio G, Liggieri L, et al. Film tension and dilational film rheology of a single foam bubble. Colloids Surf A Physicochem Eng Asp 2005;261:115–21. https://doi.org/10.1016/j.colsurfa.2004.12.051.

[42] Deminière B, Colin A, Calderon FL, Bibette J. Vieillissement par coalescence et durée de vie d'une emulsion concentrée. Comptes Rendus de l'Académie Des Sciences - Series IIC - Chemistry 1998;1:163–5. https://doi.org/10.1016/S1387-1609(99)80075-9.

[43] Georgieva D, Schmitt V, Leal-Calderon F, Langevin D. On the Possible Role of Surface Elasticity in Emulsion Stability. Langmuir 2009;25:5565–73. https://doi.org/10.1021/la804240e.

[44] Kalogianni EP, Varka E-M, Karapantsios TD, Kostoglou M, Santini E, Liggieri L, et al. A multi-probe non-intrusive electrical technique for monitoring emulsification of hexane-in-water with the emulsifier C10E5 soluble in both phases. Colloids Surf A Physicochem Eng Asp 2010;354:353–63. https://doi.org/10.1016/j.colsurfa.2009.09.004.

[45] Taylor P. Ostwald ripening in emulsions. Adv Colloid Interface Sci 1998;75:107–63. https://doi.org/10.1016/S0001-8686(98)00035-9.

[46] Voorhees PW. The theory of Ostwald ripening. J Stat Phys 1985;38:231–52. https://doi.org/10.1007/BF01017860.

[47] Cantat I, Höhler R. Foams : structure and dynamics. Oxford University Press; 2013.

[48] Meinders MBJ, van Vliet T. The role of interfacial rheological properties on Ostwald ripening in emulsions. Adv Colloid Interface Sci 2004;108–109:119–26. https://doi.org/10.1016/j.cis.2003.10.005.

[49] Ariyaprakai S, Dungan SR. Influence of surfactant structure on the contribution of micelles to Ostwald ripening in oil-in-water emulsions. J Colloid Interface Sci 2010;343:102–8. https://doi.org/10.1016/j.jcis.2009.11.034.

[50] Ravera F, Dziza K, Santini E, Cristofolini L, Liggieri L. Emulsification and emulsion stability: The role of the interfacial properties. Adv Colloid Interface Sci 2021;288:102344. https://doi.org/10.1016/J.CIS.2020.102344.

[51] Weitz DA, Pine DJ. Diffusing-wave spectroscopy. In: Brown W, editor. Dynamic Light Scattering: The Method and Some Applications, Clarendon Press; 1993.

[52] Pine DJ, Weitz DA, Chaikin PM, Herbolzheimer E. Diffusing wave spectroscopy. Phys Rev Lett 1988;60:1134–7. https://doi.org/10.1103/PhysRevLett.60.1134.

[53] Badruddoza AZM, MacWilliams S V., Sebben DA, Krasowska M, Beattie D, Durian DJ, et al. Diffusing wave spectroscopy (DWS) methods applied to double emulsions. Curr Opin Colloid Interface Sci 2018;37:74–87. https://doi.org/10.1016/j.cocis.2018.06.006.

[54] Born P, Braibanti M, Cristofolini L, Cohen-Addad S, Durian DJ, Egelhaaf SU, et al. Soft matter dynamics: A versatile microgravity platform to study dynamics in soft matter. Review of Scientific Instruments 2021;92. https://doi.org/10.1063/5.0062946.

[55] Berne BJ, Pecora R. Dynamic Light Scattering. New York: Dover; 1976.

[56] Mason TG, Weitz DA. Optical Measurements of Frequency-Dependent Linear Viscoelastic Moduli of Complex Fluids. Phys Rev Lett 1995;74:1250–3. https://doi.org/10.1103/PhysRevLett.74.1250.

[57] Mason TG. Estimating the viscoelastic moduli of complex fluids using the generalized Stokes-Einstein equation. Rheol Acta 2000;39:371–8. https://doi.org/10.1007/s003970000094.

[58] Kim HS, Şenbil N, Zhang C, Scheffold F, Mason TG. Diffusing wave microrheology of highly scattering concentrated monodisperse emulsions. Proc Natl Acad Sci U S A 2019;116:7766–71. https://doi.org/10.1073/pnas.1817029116.

[59] Wu X-L, Pine DJ, Chaikin PM, Huang JS, Weitz DA. Diffusing-wave spectroscopy in a shear flow. Journal of the Optical Society of America B 1990;7:15. https://doi.org/10.1364/josab.7.000015.

[60] Lorusso V, Orsi D, Salerni F, Liggieri L, Ravera F, McMillin R, et al. Recent developments in emulsion characterization: Diffusing Wave Spectroscopy beyond average values. Adv Colloid Interface Sci 2021;288:102341. https://doi.org/10.1016/j.cis.2020.102341.

[61] Kim HS, Senbil N, Zhang C, Scheffold F, Mason TG, Şenbil N, et al. Diffusing wave microrheology of highly scattering concentrated monodisperse emulsions. Proc Natl Acad Sci U S A 2019;116:7766–71. https://doi.org/10.1073/pnas.1817029116.

[62] Dukhin SS, Kovalchuk VI, Gochev GG, Lotfi M, Krzan M, Malysa K, et al. Dynamics of Rear Stagnant Cap formation at the surface of spherical bubbles rising in surfactant solutions at large Reynolds numbers under conditions of small Marangoni number and slow sorption kinetics. Adv Colloid Interface Sci 2015;222:260–74. https://doi.org/10.1016/j.cis.2014.10.002.

[63] Pawliszak P, Ulaganathan V, Bradshaw-Hajek BH, Manica R, Beattie DA, Krasowska M. Mobile or Immobile? Rise Velocity of Air Bubbles in High-Purity Water. Journal of Physical Chemistry C 2019. https://doi.org/10.1021/acs.jpcc.9b03526.

[64] Chan DYC, Klaseboer E, Manica R. Film drainage and coalescence between deformable drops and bubbles. Soft Matter 2011;7:2235–64. https://doi.org/10.1039/c0sm00812e.

[65] Crassous J. Diffusive wave spectroscopy of a random close packing of spheres. European Physical Journal E 2007;23:145–52. https://doi.org/10.1140/epje/i2006-10079-y.

[66] Salerni F, Orsi D, Santini E, Liggieri L, Ravera F, Cristofolini L. Diffusing wave spectroscopy for investigating emulsions: II. Characterization of a paradigmatic oil-in-water emulsion. Colloids Surf A Physicochem Eng Asp 2019;580:123724. https://doi.org/10.1016/j.colsurfa.2019.123724.

[67] Orsi D, Salerni F, Macaluso E, Santini E, Ravera F, Liggieri L, et al. Diffusing wave spectroscopy for investigating emulsions: I. Instrumental aspects. Colloids Surf A Physicochem Eng Asp 2019;580:123574. https://doi.org/10.1016/j.colsurfa.2019.123574.

[68] Cristofolini L. Simulate_path_length_distributions Matlab code (https://github.com/LuigiCristofolini/MonteCarlo_for_DWS/releases/tag/1.1) 2020.

[69] Durian DJ. Accuracy of diffusing-wave spectroscopy theories. Phys Rev E 1995;51:3350–8. https://doi.org/10.1103/PhysRevE.51.3350.

[70] Carpy R, Picker G, Amann B, Ranebo H, Vincent-Bonnieu S, Minster O, et al. Foam generation and sample composition optimization for the FOAM-C experiment of the ISS. J Phys Conf Ser 2011;327:012025. https://doi.org/10.1088/1742-6596/327/1/012025.

[71] Weitz DA, Pine DJ. Diffusing-wave spectroscopy 1870.

[72] Mätzler C. MATLAB Functions for Mie Scattering and Absorption. IAP Res Rep 2002;2002–08:1139–51.

[73] Daimon M, Masumura A. Measurement of the refractive index of distilled water from the near-infrared region to the ultraviolet region. Appl Opt 2007;46:3811–20. https://doi.org/10.1364/AO.46.003811.

[74] Kasarova SN, Sultanova NG, Ivanov CD, Nikolov ID. Analysis of the dispersion of optical plastic materials. Opt Mater (Amst) 2007;29:1481–90. https://doi.org/10.1016/j.optmat.2006.07.010.

[75] Höhler R, Cohen-Addad S, Durian DJ. Multiple light scattering as a probe of foams and emulsions. Curr Opin Colloid Interface Sci 2014;19:242–52. https://doi.org/10.1016/j.cocis.2014.04.005.

[76] Mason TG, Gang H, Weitz D a. Diffusing-wave-spectroscopy measurements of viscoelasticity of complex fluids. Journal of the Optical Society of America A 1997;14:139. https://doi.org/10.1364/JOSAA.14.000139.

[77] Crassous J, Saint-Jalmes A. Probing the dynamics of particles in an aging dispersion using diffusing wave spectroscopy. Soft Matter 2012;8:7683. https://doi.org/10.1039/c2sm25526j.

[78] Alexander M, Corredig M, Dalgleish DG. Diffusing wave spectroscopy of gelling food systems: The importance of the photon transport mean free path (l*) parameter. Food Hydrocoll 2006;20:325–31. https://doi.org/10.1016/j.foodhyd.2005.02.021.

[79] Cristofolini L, Orsi D, Isa L. Characterization of the dynamics of interfaces and of interface-dominated systems via spectroscopy and microscopy techniques. Curr Opin Colloid Interface Sci 2018;37:13–32. https://doi.org/10.1016/j.cocis.2018.06.001.

[80] Kostoglou M, Karapantsios TD. Approximation of Any Particle Size Distribution Employing a Bidisperse One Based on Moment Matching 2024;i.

[81] Dziza K, Santini E, Liggieri L, Jarek E, Krzan M, Fischer T, et al. Interfacial Properties and Emulsification of Biocompatible Liquid-Liquid Systems. Coatings 2020;10:397. https://doi.org/10.3390/coatings10040397.

[82] Muramoto Y, Kimura M, Nouda S. Development and future of ultraviolet light-emitting diodes: UV-LED will replace the UV lamp. Semicond Sci Technol 2014;29:84004. https://doi.org/10.1088/0268-1242/29/8/084004.

[83] Luttrell T, Halpegamage S, Tao J, Kramer A, Sutter E, Batzill M. Why is anatase a better photocatalyst than rutile? - Model studies on epitaxial TiO2 films. Sci Rep 2014;4:4043. https://doi.org/10.1038/srep04043.

[84] Vaccari M, Cremona M, Orsi D, Lorusso V, Baraldi A, Bosio A, et al. Zn-doped titania nanoparticles as building blocks for solid foam filters of water and air via photocatalytic oxidation. Catal Commun 2022;171:106527. https://doi.org/https://doi.org/10.1016/j.catcom.2022.106527.

[85] Liao DL, Badour CA, Liao BQ. Preparation of nanosized TiO2/ZnO composite catalyst and its photocatalytic activity for degradation of methyl orange. J Photochem Photobiol A Chem 2008;194:11–9. https://doi.org/https://doi.org/10.1016/j.jphotochem.2007.07.008.

[86] Liu G, Zhang X, Xu Y, Niu X, Zheng L, Ding X. The preparation of Zn2+-doped TiO2 nanoparticles by sol–gel and solid phase reaction methods respectively and their photocatalytic activities. Chemosphere 2005;59:1367–71. https://doi.org/https://doi.org/10.1016/j.chemosphere.2004.11.072.